

**Modified Semiconductor
Photoelectrodes for Water
Oxidation**

Ruifei Xuan

Doctor of Philosophy

University of York

Chemistry

September 2018

Abstract

Several methods for improving the properties of photoelectrodes are described. A) Amorphous materials were prepared and modified for better photo properties. Pb-Bi-Sn oxide system was prepared on FTO glass and characterized. By modification, the amorphous photoelectrode could perform as well as crystalline materials with regards to photo properties. B) Surface modification was investigated and successfully improved the photocurrent of a hematite nanotube film photoelectrode. The modification is unlike most methods used in previous reports, as only trace amounts of metal ions remain on the surface of the hematite. The surface defects were filled and this improved the charge transport. The Zn doped sample showed most enhancement; the photo current at 1.23 V vs RHE under 1 sun light reached 1.03 mA/cm² which is 77.6 % higher than the unmodified pure Fe₂O₃ electrode. C) Unique surfaces were prepared for better photo performance. Electrospinning was applied to prepare nanofibers on the surface of FTO glass. This 3D framework structure has a high surface area and acted as support for semiconductor loading. The characterization and PEC experiments show that the photocurrent was directly related to the load of the semiconductor, and the fibers sample afforded more loading. The limit of this method is the heating temperature which should be kept under a threshold value to keep the stability and tenacity of nanofibers. Characterization methods were used to get details of the samples' structure, morphology, composition, light absorbance and dopant distribution. Different PEC experiments, such as LSV, CPE, IPCE, Mott-Schottky measurement, EIS, *et al.*, were applied to study the photo properties and mechanism of enhancement. New methods have been developed to improve photoelectrodes and there is potential for other materials and applications.

Table of Contents

Abstract	2
Table of Contents	3
Table of Figures.....	7
Table of Tables.....	15
List of Accompanying Material.....	16
Acknowledgements	17
Declaration	19
1 Introduction.....	21
1.1 Overview	21
1.2 Solar energy	21
1.3 Semiconductor photocatalyst.....	23
1.4 Water splitting reaction.....	24
1.5 Energy band and water splitting	26
1.6 Photocatalysts.....	28
1.6.1 Powder catalyst	28
1.6.2 Electrode catalyst	28
1.6.3 Photoelectrochemistry	29
1.7 Visible light active photoanode material	29
1.8 Enhancement of photocatalysts	33
1.8.1 Surface area.....	33
1.8.2 Morphology	33
1.8.3 Defects	34
1.8.4 Co-catalysts	35
1.9 Amorphous photocatalysts.....	35
1.9.1 Amorphous materials	36
1.9.2 Amorphous photoelectrodes	38
1.10 Fe ₂ O ₃ based photocatalyst	40

1.10.1 Fe ₂ O ₃ catalyst.....	40
1.10.2 Enhancement.....	41
1.11 Electrospinning method	46
1.12 Project aims	48
2 The preparation and characterization of amorphous metal oxide photoelectrodes.....	52
2.1 Introduction	52
2.2 Chapter aim.....	53
2.3 Results and discussion	55
2.3.1 Synthesis of the films	55
2.3.2 Morphology and composition	57
2.3.2.1 Scanning Electron Microscopy (SEM) and Energy Dispersive Analysis of X-rays (EDX)	57
2.3.2.2 X-ray fluorescence (XRF).....	60
2.3.2.3 X-ray photoelectron spectroscopy (XPS)	61
2.3.3 Structure.....	64
2.3.3.1 X-ray diffraction (XRD).....	64
2.3.3.2 Light absorption (UV-vis absorption and visible appearance).....	66
2.3.4 Photoelectrochemistry	69
2.3.4.1 PbBiSn samples	69
2.3.4.2 Effect of calcination temperature.....	69
2.3.4.3 Volume of precursor.....	71
2.3.4.4 Concentration of precursor	73
2.3.4.5 Stability.....	76
2.3.4.6 Study of ratio of Pb-Bi-Sn in PbBiSnOx system.....	77
2.3.4.7 Incident photon-to-current efficiency (IPCE) study.....	79
2.3.5 Modification of amorphous oxide films.....	80
2.3.6 Layer by layer structures	83
2.4 Conclusion.....	85
3 Surface Modification of Fe ₂ O ₃ Anode for Photoelectrochemical Water Oxidation	89
3.1 Introduction	89
3.2 Chapter aim.....	90
3.3 Results and discussion	91
3.3.1 Synthesis of Fe ₂ O ₃ film electrode	92

3.3.2 Surface-modified iron oxide electrode with metal ions	93
3.3.3 Characterization	94
3.3.3.1 X-ray diffraction (XRD).....	94
3.3.3.2 Scanning electron microscopy (SEM) and Energy-dispersive X-ray spectroscopy (EDX).....	95
3.3.3.3 UV-visible light absorption	99
3.3.3.4 X-ray photoelectron spectroscopy (XPS)	102
3.3.3.5 Transmission Electron Microscopy (TEM)	109
3.3.4 Photoelectrochemistry	114
3.3.4.1 Photocurrent and stability test.....	114
3.3.4.2 Mott-Schottky plots.....	118
3.3.4.3 Impedance Spectroscopy (EIS) experiments.....	119
3.4 Conclusion.....	123
4 Semiconductor coated F-SnO ₂ nanofiber surface electrode.....	126
4.1 Introduction	126
4.1.1 Electrospinning	126
4.1.2 CdS photocatalyst	129
4.2 Chapter aim.....	131
4.3 Characterization	133
4.3.1 Synthesis of F-SnO ₂ nanofiber film on FTO glass.....	133
4.3.2 Decorating CdS on F-SnO ₂ nanofiber photoelectrode and pure FTO glass	134
4.3.3 Characterization	135
4.3.3.1 Scanning electron microscopy (SEM) and Energy-dispersive X-ray spectroscopy (EDS).....	135
4.3.3.2 X-ray diffraction (XRD).....	138
4.3.3.3 UV-visible spectroscopy and photography	139
4.3.4 Photoelectrochemistry	142
4.3.5 Fe ₂ O ₃ decorated F-SnO ₂ nanofiber photoelectrode.....	145
4.4 Conclusion.....	149
5 Conclusions.....	153
5.1 Concluding Remarks	153
5.2 Future Direction	155
6 Experimental.....	158
6.1 Chemicals used.....	158

6.2 Techniques.....	159
6.2.1 Powder X-ray Diffraction (PXRD)	159
6.2.2 Scanning electron microscopy (SEM)	160
6.2.3 Transmission Electron Microscopy (TEM).....	161
6.2.4 UV-vis absorption, reflection and transmission spectroscopy	161
6.2.5 Fourier-transform infrared spectroscopy (FTIR)	162
6.2.6 X-ray fluorescence (XRF) measurement	162
6.2.7 Photoelectrochemical measurement	163
6.2.7.1 Photoelectrochemistry experiments.....	163
6.2.7.2 Incident photon-to-current efficiency (IPCE) measurements	164
6.2.7.3 Mott-Schottky measurement.....	164
6.2.7.4 Electrochemical Impedance Spectroscopy (EIS).....	165
6.3 Synthetic methods	166
6.3.1 Synthesis of Pb-Bi-Sn oxides amorphous films on FTO glass	167
6.3.2 Synthesis of Pb-Bi-Sn oxide on KBr disc for FTIR	169
6.3.3 Doping the amorphous electrode with Fe, Co and Cu dopant	169
6.3.4 Doping the amorphous electrode with WO ₃ nanoparticles	170
6.3.5 Electrodeposition of Co-Pi on amorphous electrode	170
6.3.6 Preparing layer-by-layer amorphous films on FTO glass	171
6.3.7 Synthesis of iron oxide slide	171
6.3.8 Synthesis of metal-modified iron oxide electrode	172
6.3.9 Synthesis of F-SnO ₂ nanofiber film on FTO glass.....	173
6.3.10 Decorating CdS on F-SnO ₂ nanofiber photoelectrode and pure FTO glass	175
6.3.11 Growing Fe ₂ O ₃ nanotubes on F-SnO ₂ nanofiber photoelectrode and pure FTO glass	176
Abbreviations.....	177
List of references	180

Table of Figures

- Figure 1 The energy band structure of (c) semiconductor, which is different from (a) metal (conductor) and (b) insulator (nonconductor). (a) There is no band gap in a conductor and the valence band (VB) and conduction bands (CB) overlap. (b) The band gap of an insulator is too large for electrons to overcome at room temperature. (c) The band gap of a semiconductor is smaller than that of an insulator, thus the electrons can be excited to the CB, and improve the conductivity. 23
- Figure 2 The scheme of photocatalytic activity of TiO_2 . The light-excited electrons from the top of valence band (VB) to the bottom of conduction band (CB) and the redox reactions for water splitting. .. 24
- Figure 3 The potential barrier of water decomposition reaction. The reaction with catalyst has a lower potential barrier. 25
- Figure 4 Band edge positions with respect to the vacuum level and NHE for selected semiconductors at pH=0 (a) oxides, phosphates and carbides; (b) chalcogenides and silicon. The top squares represent the conduction band edges; the bottom squares represent the valence band edges. The top numbers show the exact conduction band level and the number between the squares is the band gap. The two dashed lines indicate the water redox reaction potentials. ²¹ 27
- Figure 5 Spectrum of sunlight above atmospheric and at surface. 31
- Figure 6 The difference between crystalline and amorphous materials is whether they exhibit long-range order or short-range. 36
- Figure 7 Overpotentials of amorphous metal oxide materials. ⁷¹ 37
- Figure 8 Representative current–potential curves in the dark (dotted line) and under simulated illumination (solid curves) recorded for (1) pristine

hematite, (2) 10.71% Zn, (3) 1.96% Ti, and (4) 1.40% Ti + 5.58% Zn-modified hematite electrodes. Inset: the photocurrent onset potential (dashed line) and current density (solid line) at 1.23 V vs RHE for the hematite and modified-hematite electrodes ¹⁰⁶	43
Figure 9 SEM of Co–Pi/ α - Fe ₂ O ₃ composite photoanodes showing (a) ring-like deposition of Co–Pi in selective areas of the α - Fe ₂ O ₃ surface and (b–d) magnified views of Co–Pi patches within this ring. (d) Co–Pi conforming to the topology of the underlying α - Fe ₂ O ₃ mesostructure. The cracks in the Co–Pi result from drying ¹⁰⁷	44
Figure 10 SEM image of needle-like Fe ₂ O ₃ thin film, composed of small individual nanoparticles ¹⁰⁸	45
Figure 11 The schematic diagram of the energy band structure of the SrTiO ₃ / α - Fe ₂ O ₃ heterojunction ¹⁰⁹	46
Figure 12 Schematic diagram of electrospinning.....	47
Figure 13 The molecular formula ethylhexanoate (EH) salt which is used in this chapter. M is the metal element.	53
Figure 14 FTIR spectrum of sample using Fe ₈₀ *7.5 after different time periods of UV irradiation.....	57
Figure 15 Surface SEM images of (a) FTO glass, (b) PbBiSn _{7.5} *10 and (c) PbBiSn _{52.5} *40.	58
Figure 16 SEM/EDX images of PbBiSn _{7.5} *10 heated at 100°C. (a)SEM image and linear sweep EDX of cross section, where red line is for Si, green line for Sn, blue line for Pb and yellow line for Bi. (b)Elements mapping of cross section.....	59
Figure 17 XRF mapping of Pb, Bi and Sn and XRF spectrum of central area of a PbBiSn _{7.5} *10 film.....	60

- Figure 18 Etching depth profiling quantification of (a) all elements, (b) Pb, (c) Bi and (d) Sn in $\text{PbBiSn}_{7.5*10}$ film before PEC (fresh $\text{PbBiSn}_{7.5*10}$).
..... 63
- Figure 19 XRD pattern of (a) $\text{PbBiSn}_{7.5*10}$ samples heated at different temperatures for 1 hour and (b) $\text{PbBiSn}_{7.5*10}$ samples prepared with different volumes of precursor. The red vertical bars are the standard spectrum of FTO glass. 65
- Figure 20 UV-vis absorption spectrum of a series of samples. (a) samples of different concentrations of precursor (b) samples with different volumes of precursor (c) samples doped with different amounts of amorphous iron oxide (d) samples doped with different amounts of amorphous cobalt oxide (e) samples doped with different amounts of amorphous copper oxide..... 67
- Figure 21 Photographs of samples with change of colour. (a) $\text{PbBiSn}_{7.5*10}$, (b) PbBiSn_{15*10} , (c) $\text{PbBiSn}_{22.5*10}$, (d) PbBiSn_{30*10} , (e) $\text{PbBiSn}_{37.5*10}$, (f) PbBiSn_{45*10} , (g) $\text{PbBiSn}_{52.5*10}$, (h) $\text{PbBiSn}_{52.5*20}$, (i) $\text{PbBiSn}_{52.5*40}$ and (j) $\text{PbBiSn}_{52.5*40}$ heated at 500°C 68
- Figure 22 Photo electrochemistry on samples calcined under different temperatures ((a) LSV in the dark, where the large current after 1.6 V is due to water oxidation. (b) LSV-illuminated (on)-dark(off) and (c) CPE-photoresponse under bias of 1.78 V versus RHE). Samples were all prepared using $20\mu\text{L}$ 7.5% w/w PbBiSn precursor and heated at 100°C 70
- Figure 23 Photoelectrochemistry on samples prepared with different volumes of precursor ((a) LSV, (b) LSV-photo-dark and (c) CPE-photo-dark). Samples were all prepared using 7.5% w/w PbBiSn precursor and heated at 100°C 72
- Figure 24 Photoelectrochemistry on samples prepared with different concentrations of precursor ((a) LSV-photo-dark and (b) CPE-photo-

dark under bias of 1.78 V versus RHE)). Samples were all prepared by 20 μ L PbBiSn precursor and heated at 100°C.	73
Figure 25 The relationship between (a) absorbance and photocurrent and (b) between concentration of precursor and absorbance or photocurrent. The data was collected from samples of 10 μ L of different concentrations of PbBiSn precursor heated at 100°C. The photocurrent was collected at bias of 1.3 eV versus RHE. The absorbance data was collected at wavelength of 500 nm.	75
Figure 26 Stability test of samples with 52.5% w/w PbBiSn precursor. ..	76
Figure 27 (a) Photo current (=(current under visible light – current in dark) and (b) dark current of Pb-Bi-Sn oxide samples with different ratios.	78
Figure 28 Incident photon-to-current efficiency (IPCE) measured at 1.23V versus RHE. The test sample is PbBiSn _{52.5*10}	79
Figure 29 Adding different metals into Pb-Bi-Sn system. CPE of (a) PbBiSn _{7.5*10} with Fe ₂ O ₃ , (b) PbSn _{7.5*10} with Fe ₂ O ₃ , (c) PbBi _{7.5*10} with Fe ₂ O ₃ , (d) PbBi _{7.5*10} with CuO, (e) PbBi _{7.5*10} with Co ₂ O ₃ and (f) PbBiSn _{7.5*10} with WO ₃ . The bias is 1.78 V versus RHE. The percentages are mass fractions (w/w).	82
Figure 30 (a) LSV and (b) CPE test of PbBiSn _{7.5*40} . The CPE test was run under a bias potential of 800mV.	83
Figure 31 Comparison of mixed metal oxide film (black line) and layer-by-layer film (red line). (a) LSV and (b)CPE test of Pb/Fe sample and (c) LSV and (d)CPE test of Bi/Pb/Fe sample. The CPE tests were all running with a bias of 1.78 V versus RHE.	84
Figure 32 Energy band structure of Pb-Fe-Bi layer-by-layer film.	85
Figure 33 (a) Top view and (b) back view of FTO slide before hydrothermal experiment. Final sample (c) with Teflon tape (for PEC/EIS experiments) and (d) without Teflon tape.	93

Figure 34	XRD figure of unmodified Fe and Li, Na, K, Mg and Zn modified samples. The peaks of FTO (PDF 46-1088) and Fe ₂ O ₃ (PDF 33-0664) are marked using asterisk (*) and plus (+) respectively.....	95
Figure 35	SEM image of FTO surface and Fe ₂ O ₃ layer surface. The image was captured at the boundary of the Fe ₂ O ₃ covered area. The left part in the image is lower level FTO particles and the right part is higher level Fe ₂ O ₃ nanorods.	96
Figure 36	Low magnification SEM images of the surface of pure Fe and Li, Na, K, Mg and Zn modified samples. All the images are obtained at the same magnification.	97
Figure 37	The SEM images of cracked surface area of unmodified and modified samples. The thicknesses are marked in every image.	98
Figure 38	UV-visible absorption spectrum of unmodified and modified samples. The data was collected before dip-coating (black), after dip-coating (red) and after PEC/EIS experiments (green), respectively.	100
Figure 39	(a) Original and (b) normalized UV-visible absorption spectrum of unmodified Fe and Li, Na, K, Mg and Zn modified electrode samples.	101
Figure 40	(a) XPS spectrum for Fe 2p. (fresh unmodified and Li, Na, K, Mg, Zn modified samples and used Zn modified sample) (b) Splitted XPS spectrum of fresh unmodified sample.	103
Figure 41	Relatively higher intensity Na peaks of used Zn modified sample.....	104
Figure 42	Etching XPS measurement of used Zn modified sample for (a) Fe 2p, (b) O 1s and (c) Zn 2p peak.	106
Figure 43	XPS spectra for (a) survey (b) Na 1s peak of fresh Na modified sample, (c) K 2s peak of K modified sample, (d) Mg 1s peak of fresh Mg modified sample, (e) Zn 2p peak of fresh Zn modified sample, (f) Zn 2p peak of used Zn modified sample.	107

Figure 44 (a) TEM image of Zn doped Fe ₂ O ₃ . (b) High resolution image magnified the area in red box.....	110
Figure 45 (a) TEM and (b) electron diffraction pattern of nanotubes samples.....	111
Figure 46 (a) STEM of Zn-doped Fe ₂ O ₃ (b) EDX of red circled area showing Fe and Cu (from grid) but no Zn.....	112
Figure 47 (a) STEM of Zn-doped Fe ₂ O ₃ . EDX of (b) regions 1 (c) regions 2.....	113
Figure 48 (a) Original and (b) normalized Linear sweep voltammetry results of unmodified and Li, Na, K, Mg and Zn modified samples. The normalizing method is the same as that which was used for UV-vis spectrum.	115
Figure 49 Two different stability experiments of unmodified Fe ₂ O ₃ electrode. (a) Comparison of LSV results collected before and after EIS experiments. (b) Long time (24 hours) Chronoamperometry experiments.....	117
Figure 50 The Mott-Schottky plots of unmodified and Li, Na, K, Mg and Zn modified Fe ₂ O ₃ electrodes.	118
Figure 51 Analyzed (a) R1, (b) Q1, (c) R2, (d) Q3, and (e) R3 value change against the potential. (f) LSV figure for comparison.	120
Figure 52 Total resistance calculated from LSV (black line) and sum of R1+R2+R3 (red square point).....	122
Figure 53 “Firecracker-shaped” ZnO/polyimide hybrid nanofiber (the upper diagram is the process of fabrication and the lower section is the (a) SEM image and (b) HR-SEM image of the sample’s fibres). ¹²⁷	127
Figure 54 Core-shell metal oxide/polymer fibres. ¹⁶⁵	128
Figure 55 Photocurrent measurements performed at a light intensity of 1.5AM in 1M KOH, SG (sol-gel) and SG-fibers, as well as SG-P25 composite photoelectrodes. ¹⁶⁶	129

Figure 56 SEM and HRSEM image of fibre covered FTO glass (a)(c) before and (b)(d) after CdS coating.....	136
Figure 57 EDX mapping of C, S, Cd, Sn and O elements corresponding to SEM images.....	137
Figure 58 XRD pattern of samples with and without CdS coating. The peaks of FTO (PDF 46-1088) are shown using vertical red lines. The peaks of CdS (PDF 43-0985) are marked using asterisks (*). Two unknown peaks are marked using plus (+).....	139
Figure 59 UV-visible measurement of (a) transmission and (b) reflection.	141
Figure 60 Calculated UV-visible absorption spectrum.....	142
Figure 61 Test results of pure FTO, fibered FTO and CdS-coated fibered FTO. (a) Linear sweep voltammetry results in dark. (b) light/dark current switch test with 1 sun of Xe lamp through 420 nm band pass filter, 0 V vs Ag/AgCl (0.8 V vs RHE), Na ₂ S (0.25 M)/Na ₂ SO ₃ (0.35 M) at pH 11.....	143
Figure 62 Linear sweep voltammetry results with light switch that shows light response of CdS coated samples on substrate of FTO, 3.5 minutes electrospun (ES) FTO and 7 minutes electrospun FTO glass.	145
Figure 63 SEM and HRSEM images of Fe ₂ O ₃ coated fibered FTO electrode.	146
Figure 64 Photographs of Fe ₂ O ₃ coated on pure FTO, 1.5 minute electrospun FTO and 7 minute electrospun FTO glass substrate.	147
Figure 65 Linear sweep voltammetry results of Fe ₂ O ₃ coated samples on different substrates. Solid lines are for results obtained under 1 sun light irradiation and the dash lines are for results got in the dark. .	148
Figure 66 Proposed structure of a working electrode.....	166
Figure 67 Scheme of module used to analyze the EIS data.....	166

- Figure 68 Reaction of decomposing ethylhexanoate (EH) metal salt to amorphous metal oxide..... 167
- Figure 69 The schematic drawing that illustrates the experiment processing steps. The precursor was spin coated onto FTO glass to form a film sample as a working electrode (WE). The electrochemical experiment was performed in a three-electrode cell using 0.1 M NaOH (aq) as the electrolyte solution. A platinum wire was used as the counter electrode (CE). An Ag/AgCl (sat. NaCl) reference electrode (RE) was separated from electrolyte solution with a glass protector..... 168
- Figure 70 Scheme of electrospinning experiments. (a) peristaltic pump, (b) temperature controller for collector heating, (c) DC power supply, (d) electrospinning box with an observation window, (e) digital camera, (f) metal collector and (g) needle of syringe. 174

Table of Tables

Table 1 Photoresponses of doped hematite photoelectrodes ⁸⁷	41
Table 2 The samples used to collect the data for the photocurrent phase diagrams. The ratio of Pb Bi and Sn is the relative atomic ratio.	56
Table 3 The proportion of different valence states of Pb, Bi and Sn in PbBiSn _{7.5*10} films following changes during the PEC experiment. (Proportion of PbO was calculated from Pb ₃ O ₄ .).....	61
Table 4 Deconvolution parameters of the Fe 2p peaks measured for the fresh unmodified Fe ₂ O ₃ sample. (oct, octahedral; tet, tetrahedral; sat, satellite).....	105
Table 5 Surface relative sensitivity factors ^{141, 142} and peak area. Ratio to Fe was calculated though equation 8.	109
Table 6 The Donor density and Flatband potential calculated from the Mott-Schottky plots of unmodified and Li, Na, K, Mg and Zn modified Fe ₂ O ₃ electrodes.	119

List of Accompanying Material

A digital copy of this thesis is included on a CD in the back of this volume.

Acknowledgements

There are many people that I wish to thank for their support and help.

Firstly, I would like to thank my supervisor, Richard Douthwaite, for his academic support and guidance. He taught me a lot about how to be a researcher and has always been approachable for any problems whether to do with my studies or my life in the UK, no matter how busy he was. I thank him for his help and all his suggestions. I am grateful to my IPM Victor Checkik, for the useful discussions and advice in TAP meetings. I am also grateful to the Wild Funding and Dr Anthony Wild for Funding my research.

I would like to thank Ian Wright, Adrian Whitwood, Leonardo Lari and other staff in the department and nanocentre for their assistance and support in using the instruments, including XRD, SEM and TEM. They gave me lots of help and were always happy to answer my questions about the instruments. I would like to thank all the admin and technical staff in the department.

Around the lab and the office, I would like to thank Dr Menglong Zhang who gave me lots of assistance. Especially during my first days in the UK, he helped me to fit into an unfamiliar environment and explained lots of things both in the lab and in life. I would also like to thank Dr Natalie Pridmore and Dr Danielle Jowett. They are always nice and friendly and help me feel included in the lab. I would also like to thank Dr Robert Mitchell, who is friendly and has helped a lot in TEM experiments. Thanks go to Ben who is always kind to me, and Dr Christopher Unsworth who helps a lot with experiments. Thank you to Mina, you are always very humorous and funny. My thanks to Katy, a friendly and

interesting girl, and to Will and Dr Wi Nawawi, it is a pleasure to study with you. Joy, thanks for much help and discussion about the experiments and measurement. Thanks to Emma: whatever problems I have had, you always helped me to solve them. I would like to especially thank Haowei Huang who provided many useful discussions. I always had a good time making dinner and chatting with you. Outside of the RED group, I am also grateful to other people in E014: Dr Luisa Ciano, Dr Sindhu Krishna and Dr Lu Zhou. They also helped me a lot.

Lastly, I would like to thank my family. I am extremely grateful for everything my parents have done for me. I love you.

Sep 2018

Declaration

The work presented in this thesis is to the best of my knowledge original. This work has not previously been presented for an award at this, or any other, University. All sources are acknowledged as References. The work contained within is entirely my own, with the following exception:

- TEM of Zn doped Fe_2O_3 were performed by Leonardo Lari from *The York JEOL Nanocentre*.

Chapter 1

Introduction

1 Introduction

1.1 Overview

Semiconductor materials have been widely applied to photoelectrochemical (PEC) water splitting. Specifically metal oxides such as Fe_2O_3 , ZnO and TiO_2 , have been used to make photoanodes for the oxygen evolution reaction from water oxidation. In this thesis, FTO glass was used as the substrate for OER experiments. Amorphous metal oxides, surface-doped Fe_2O_3 , and fluorine-doped tin dioxide nanofibers were prepared on FTO glass and tested for better photoelectrochemistry performance. The aim of this work is to investigate the synthesis and properties of new photoelectrochemical semiconductor electrodes with enhanced PEC properties. This chapter will present a brief review of results in the area of PEC semiconductors related to this thesis.

1.2 Solar energy

Energy, as the base of modern society, has always been a hot topic from the moment that people started to use machines. Traditional fossil fuels including coal and petroleum, have two crucial problems. Firstly, fossil fuels generate heavy pollution and CO_2 , a greenhouse gas responsible for climate change. Secondly, they are not renewable and will be exhausted in a few hundred years. People have tried to develop sources of green energy to solve these problems, like wind, hydro, tidal, geothermal, *etc.* However, there are limitations of usage

which make these energies difficult to develop, such as intermittency, geographical limitations, and storage.

Solar energy is also a strong candidate for renewable energy, and could potentially make a significant contribution to the world's needs. In 2016, the total energy consumption of the world was about 5.712×10^{20} J. This equals an average energy consumption rate of 18.2 terawatt (TW), of which 81.4 % is from coal, natural gas and oil.¹ By comparison, over 120,000 TW of energy is received from the sun, yet only 1.4 % of energy consumption came from solar power - less than 0.27 TW.¹

Although humans have used solar energy for thousands of years, there has been much research on the core problem, which is how to efficiently convert and store solar energy. In nature, sunlight is transformed into other types of energy and stored everywhere, from water and wind through to the chlorophyll in plants to give carbohydrates. In each case a lot of time can pass before the energy can be utilized. People are working to directly use solar energy, and one solution is water splitting where solar energy is stored in chemical bonds by driving an endergonic reaction.

Since 1972, when Fujishima and Honda reported that water could be split into hydrogen and oxygen with a UV illuminated TiO_2 electrode², using solar energy to split water became an attractive prospect and was widely researched. By splitting water, solar energy could be stored in terms of chemical energy in hydrogen and oxygen. Hydrogen could generate electricity in a fuel cell or be burned to power a turbine. Moreover, the overall process is environmentally friendly since the product of hydrogen combustion is water.

1.3 Semiconductor photocatalyst

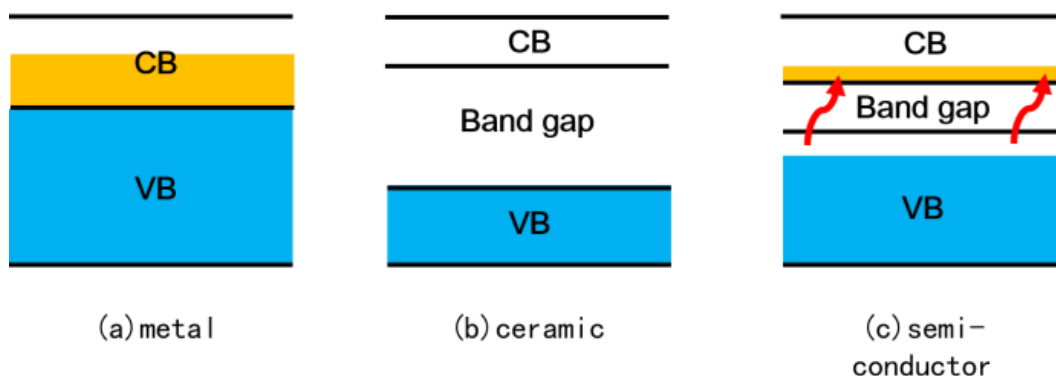
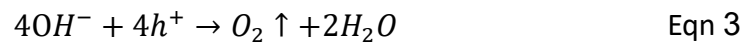


Figure 1 The energy band structure of (c) semiconductor, which is different from (a) metal (conductor) and (b) insulator (nonconductor). (a) There is no band gap in a conductor and the valence band (VB) and conduction bands (CB) overlap. (b) The band gap of an insulator is too large for electrons to overcome at room temperature. (c) The band gap of a semiconductor is smaller than that of an insulator, thus the electrons can be excited to the CB, and improve the conductivity.

Semiconductors are a naturally good material for photoelectrochemistry and related photocatalysis. Unlike metals and insulators, semiconductors have narrow bandgaps (Figure 1). As a result, the electrons are easily excited by photons and transfer from the valence band to conduction band leaving holes in the valence band. Partially filled energy bands make semiconductors conductive. The excited electrons, or holes, are unstable and highly energetic and their potential is sufficient to be able to split water. The full reaction of water splitting is shown below:



The half reactions describe the redox reactions:



Taking TiO_2 as an example (Figure 2), the electrons at the top of the valence band receive energy from light and are transferred to the conduction band. These higher-energy electrons are active and reduce H^+ in water. At the valence band oxidation reaction occurs and returns the electrons to TiO_2 .

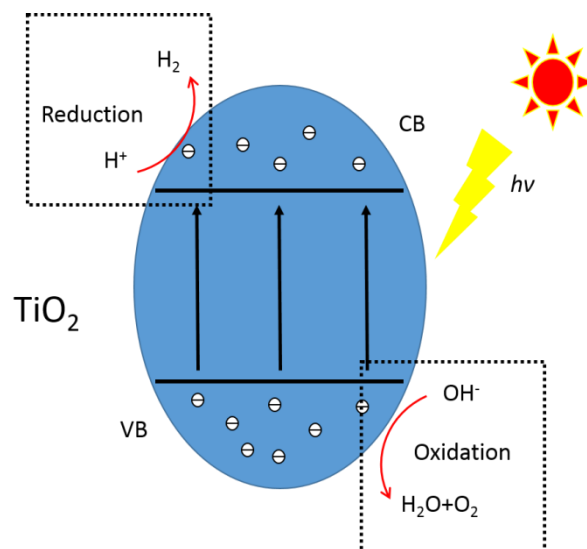


Figure 2 The scheme of photocatalytic activity of TiO_2 . The light-excited electrons from the top of valence band (VB) to the bottom of conduction band (CB) and the redox reactions for water splitting.

1.4 Water splitting reaction

Using a semiconductor for water splitting comprises three processes: light absorption; charge separation; and redox reactions with species in water. The photon energy is stored in excited carriers and transferred to water. Thus, the light energy needs to be higher than the energy needed for the water splitting reaction. Figure 3 shows the energy change in the reaction of water splitting, which is an endergonic reaction. The Gibbs free energy of the reaction is 237 kJ/mol, which equals 1.23 eV. The water molecule acquires energy, and as a result the excited H-O bond breaks and forms new H-H and O-O bonds. In fact, the required potential is higher because of extra overpotentials and slow reaction kinetics. In the electrolysis experiment, a potential of about 1.8 eV is necessary to overcome the potential barrier. A photoactive semiconductor catalyst could lower this barrier to use less energy (Figure 3).

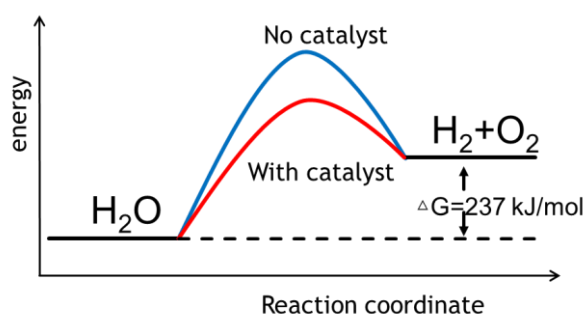


Figure 3 The potential barrier of water decomposition reaction. The reaction with catalyst has a lower potential barrier.

When it comes to the half reactions, the excited electrons, or holes, should have higher energy than the minimum energy of the hydrogen evolution reaction (HER) and oxygen evolution reaction (OER). Figure 4 shows the band levels of semiconductor and redox potentials for water splitting. Semiconductors that have a higher conduction band edge than the potential of $\text{H}_2\text{O}/\text{H}_2$ (0 eV versus

NHE), can reduce water and generate hydrogen. Materials for OER need a lower valence band edge than the potential of O₂/H₂O (1.23 eV versus NHE).

1.5 Energy band and water splitting

The energy band gap and the position of CB and VB determine the performance of a semiconductor in a water splitting experiment. For the semiconductors shown in Figure 4, if the VB edge is lower than the potential of O₂/H₂O (1.23 eV versus NHE), the semiconductor could be used for OER. In the same way, the HER experiment requires a semiconductor with its CB edge higher than the potential of H₂O/H₂ (0 eV versus NHE). Semiconductors that meet both requirements could be prepared for whole water splitting. For instance, wide band gap semiconductors like TiO₂³⁻⁸, In₂O₃⁹⁻¹¹, SrTiO₃¹², ZrO₂^{13, 14} and ZnO¹⁵⁻²⁰ have been used to generate hydrogen and oxygen. However, the wide band gap means that most of these semiconductors are only UV light active.

The energy of the photon is related to the wavelength of light, as shown in the following equation:

$$E = hv = \frac{hc}{\lambda} \quad \text{Eqn 4}$$

Where h is Plank's constant, c is the velocity of light and λ is the wavelength of light.

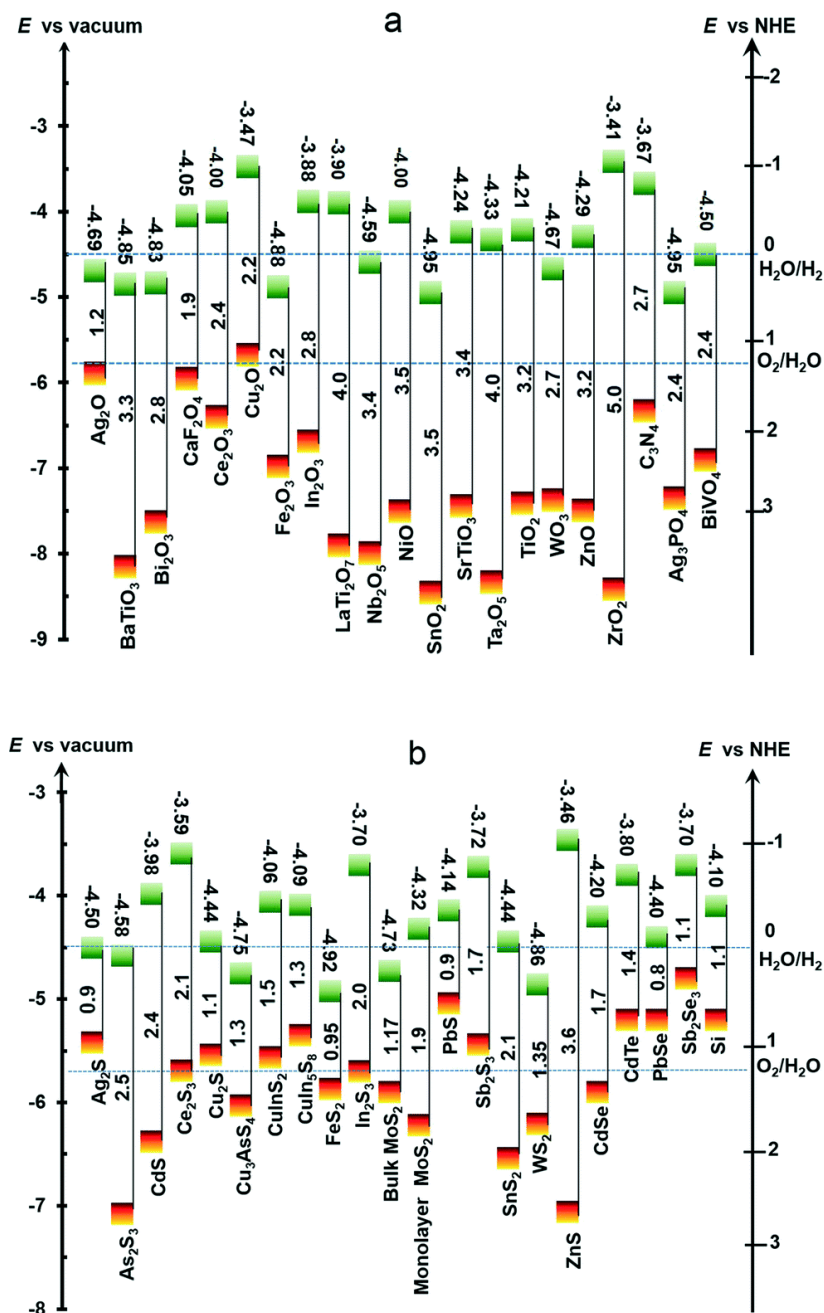


Figure 4 Band edge positions with respect to the vacuum level and NHE for selected semiconductors at $\text{pH}=0$ (a) oxides, phosphates and carbides; (b) chalcogenides and silicon. The top squares represent the conduction band edges; the bottom squares represent the valence band edges. The top numbers show the exact conduction band level and the number between the squares is the band gap. The two dashed lines indicate the water redox reaction potentials. ²¹

1.6 Photocatalysts

Certain kind of semiconductors are photocatalysts, which absorb light and utilize solar energy to catalyze reactions. There are two general methods to use a photocatalyst to split water.

1.6.1 Powder catalyst

A powder catalyst is mixed in aqueous solution with stirring and irradiated under light. It is easy to prepare and dispersed easily in the solution. However, a powder catalyst has two main disadvantages. First, it is hard to collect after the experiment, and needs many steps to collect and clean it. Second, it is dangerous and difficult to separate hydrogen and oxygen when mixed together.

1.6.2 Electrode catalyst

Supporting a photocatalyst on an electrode for splitting water solves the problems of powder catalysts. It is easy to collect, and hydrogen and oxygen are generated on the surfaces of different separated electrodes. Moreover, the electrodes can be biased to improve the splitting. Bias potential forms an electric field in which the electrons and holes will be separated and

recombination losses will be reduced. The electrons will move to the cathode, and holes to the surface of the anode. Depending on the system either cathode or anode can be photoactive or both electrodes can be photoactive.

1.6.3 Photoelectrochemistry

Photoelectrochemistry is based on electrochemistry, which is a reliable method for evaluating potential semiconductor materials. Electrode catalysts are supported on a conductive substrate (for example FTO or ITO glass) and connected to a potentiostat. A controlled voltage is applied and it is irradiated under a controlled light, at which point the current through the electrode will be recorded and calculated. In a different mode, the photoelectrochemical experiment could show the details of the electrical properties. The comparison of the same experiment running in the dark or under irradiation allows for investigation of the photochemical processes.

A typical three-electrode photoelectrochemical cell (PEC) includes a counter electrode (such as Pt wire or mesh), a reference electrode and a working electrode for the photoactive semiconductor. All the electrodes are put in a three-neck round bottom flask adapted with a quartz window designed for illumination. The flask is filled with appropriate electrolyte for different conditions.

1.7 Visible light active photoanode material

Since Fujishima and Honda first reported in 1972², TiO₂ is the most popular material for photocatalysis material owing to its nontoxicity, stability and low cost. However, anatase TiO₂ has a band gap of 3.2 eV²², resulting in an absorption edge at 386 nm. Therefore, this popular photocatalyst can only absorb ultraviolet light, which is only a small part of sunlight.

Sunlight comprises a wide range of different light. Visible light is the strongest output range of the sunlight spectrum (Figure 5). Of the radiant energy emitted from the Sun, about 10% lies in the UV and about 40% in the visible region²³. After atmospheric absorption, the sunlight received at the Earth's surface consists of about 44% visible light and 3% UV light.

To better utilize solar energy, the semiconductor should have a proper bandgap to absorb these low energy visible light photons. According to equation 4, the band gap maximum is 2.95 eV for visible light absorption.

Spectrum of Solar Radiation (Earth)

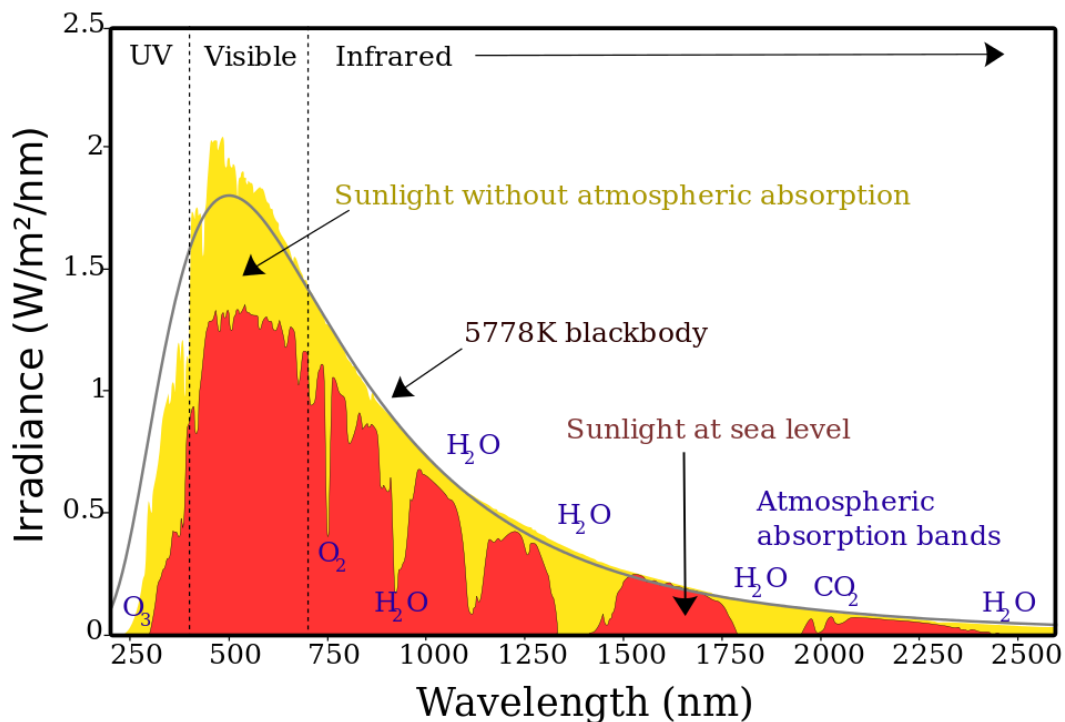


Figure 5 Spectrum of sunlight above atmospheric and at surface.

As mentioned before, a visible light active photoanode material for OER should have a proper band gap (< 2.95 eV) and lower VB edge (< 1.23 eV versus NHE). The material should be physically and chemically stable during the PEC experiment; and it is important that it should be nontoxic and cost-effective.

BiVO_4 is a well-known visible-light active material for water oxidation, and absorbs visible light owing to its suitable band gap (2.4 eV)²⁴. It is nontoxic and chemically stable in aqueous solution under irradiation. However, due to the poor charge transport²⁵ BiVO_4 usually shows low photocatalytic activity. Doping²⁶⁻²⁸, heterojunction structure²⁹⁻³³ and co-catalyst^{34, 35} are effective methods to improve the charge transport and the performance.

WO_3 is also widely known as a stable and nontoxic catalyst material. It has a band gap of 2.8 eV and shows an activity for oxygen evolution from aqueous solutions when including a sacrificial reagent.^{36, 37} Considering the band position, WO_3 could be produced for both hydrogen evolution reaction (HER)³⁸ and OER³⁹. However, photogenerated holes accumulate on the surface of the WO_3 photoanode owing to the slow kinetic nature of OER⁴⁰. Thus the WO_3 would suffer from a gradual loss of photoactivity due to the formation and accumulation of peroxo species⁴¹⁻⁴³, anion oxidation⁴⁴ and photocorrosion⁴⁰. Jason A. Seabold and his co-workers investigated the effect of Co-Pi co-catalyst and found that the Co-Pi coupled WO_3 electrode achieved a more efficient and sustainable solar-to- O_2 conversion, and prevented the photocurrent decay of WO_3 electrode⁴⁰.

CdS, an n-type semiconductor which possesses a 2.4 eV⁴⁵ band gap, has a good visible light absorption edge. It has a long diffusion length for photogenerated carriers⁴⁶ which is important for carriers transport. Corresponds to the energy band, CdS has been widely used as photoanode. Alka Pareek and his co-workers⁴⁷ prepared nanorod-like structured CdS photoanodes for hydrogen generation using a spray pyrolysis method. The nanostructured morphology enhanced the performance of the photoanode and the technique allows a large area fabrication.

Fe_2O_3 was first used as a photocatalyst for water splitting in 1978. $\alpha\text{-Fe}_2\text{O}_3$ (hematite) is an n-type semiconductor with a band gap of about 2.0 eV to 2.2 eV^{48, 49}. Fe is the most abundant metallic element in the Earth's crust. Fe_2O_3 is also stable, nontoxic and has a good absorbance for visible light. It has been widely used for water splitting⁵⁰⁻⁵⁴. However, it has poor carrier dynamics and very high recombination rates.

1.8 Enhancement of photocatalysts

Not every semiconductor material can be a photocatalyst due to the limit of the energy band gap and band position. To make more semiconductor materials photoactive and to improve the performance of photocatalysts, several methods can be applied.

1.8.1 Surface area

The surface of the photocatalyst is the place where the reactions occur. Generally, electrodes with higher surface areas provide more active sites per gram to which reaction species can be attached. For instance, Wei-Guang Yang and his co-workers⁵⁵ prepared highly-crystallized mesoporous titania microspheres with surface areas up to $193 \text{ m}^2\text{g}^{-1}$. The ultrahigh surface areas enhanced the light harvesting within the photoanodes of dye-sensitized solar cells. However, a higher surface area may also bring a higher recombination of electrons and holes, which needs to be considered.

1.8.2 Morphology

Different morphology could affect the diffusion length of photogenerated carriers which is important for carrier transfer and electron/hole recombination. H. J. Lewerenz *et al.*⁵⁶ investigated the performance of a series of n-WSe₂ photoanodes with different surface morphologies. They found that the decrease in photocurrent and photovoltage could be explained by the drift of minority carriers near faults on the surface due to the large amount of surface states.

1.8.3 Defects

In semiconductor materials, defects on the surface can be recombination centres for electrons and holes, thus decreasing the photo properties. Preparing nano-size materials could increase the carriers transfer due to the shorter distance from the photogenerated carriers to the surface. Guoshuai Wang *et al.*⁵⁷ prepared high quality CuInS₂ quantum dots and controlled Cu/In non-stoichiometric ratios to reduce the surface defects. When decreasing the defect states, better cell performance was observed.

On the other hand, defects are not always a problem in photocatalysis. BoTang and his co-workers⁵⁸ prepared three-dimensional graphene networks with various defect densities to modify TiO₂ for better photocatalytic performances. They compared samples with different defect densities and found that the photocatalytic activities were closely related to the defect density. The surface defects could act as active sites to adsorb pollutants for better following decomposition process. The defects also enhanced the electron-transport ability by improving the contact between the 3D graphene networks and the TiO₂.

1.8.4 Co-catalysts

Co-catalysts, such as Pt, Au metals or other semiconductors, have been widely used to improve the photo properties. Generally, the co-catalysts enhanced the photogenerated electrons and holes separation before they recombined. Amorphous NiO co-catalyst could provide more active sites and allow effective light harvesting, thus improving the visible-light-driving hydrogen generation of g-C₃N₄.⁵⁹

Noble metals were also used in previous works. Weiyi Ouyang *et al.*⁶⁰ deposited Ru co-catalyst to prepare RuO₂-TiO₂ for hydrogen evolution. The improvement was better than Pt and Pd containing catalysts. Au co-catalyst was also deposited with La₂Sn₂O₇ to enhance the photocatalytic CO₂ reduction with water.⁶¹

Co-Pi is also a good co-catalyst and could be deposited photoelectrochemically. Co-Pi/ α -Fe₂O₃ prepared under microwave irradiation could significantly enhance the photocurrent related to photocatalytic water oxidation.⁶²

1.9 Amorphous photocatalysts

1.9.1 Amorphous materials

Most photocatalysts are crystalline materials due to their lower defect density, by contrast, amorphous materials have short range order and no fixed melting point (Figure 6). Amorphous materials only have short range ordered crystal structure so that no peaks are observed in XRD. Amorphous film materials have been used as recording ^{63, 64}, solar cell⁶⁵, electrode⁶⁶, gas sensor⁶⁷⁻⁷⁰ and catalyst materials.

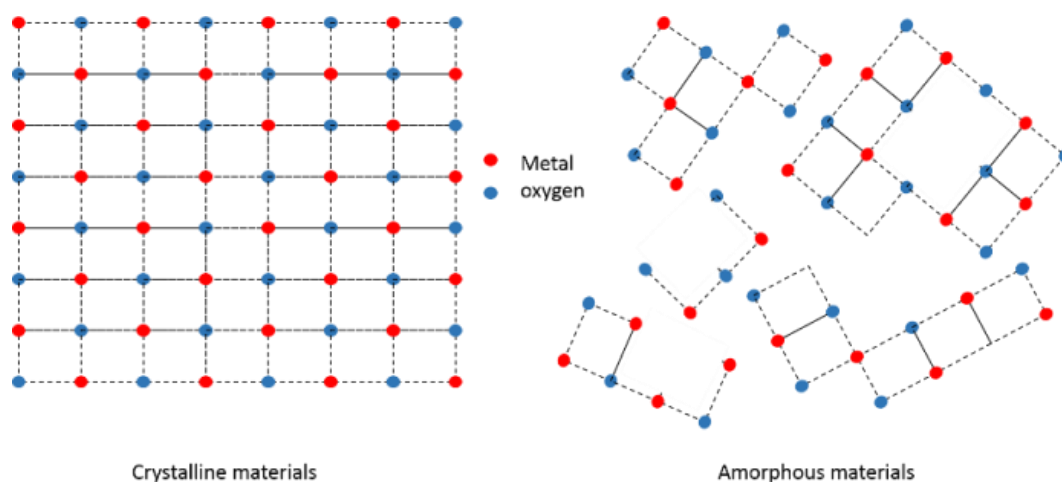


Figure 6 The difference between crystalline and amorphous materials is whether they exhibit long-range order or short-range.

Amorphous oxides have been used for electrolytic oxidation of water (not photoactivated). In 2013, Rodney D. L. Smith *et al.*⁷¹ reported several ratios of amorphous Fe, Co and Ni oxides that show better electrochemistry properties than crystalline iron oxide. The best of these, the amorphous $\text{Fe}_{50}\text{Co}_{50}\text{O}_x$ electrode, could decrease the onset potential to 1.4 eV (Figure 7).

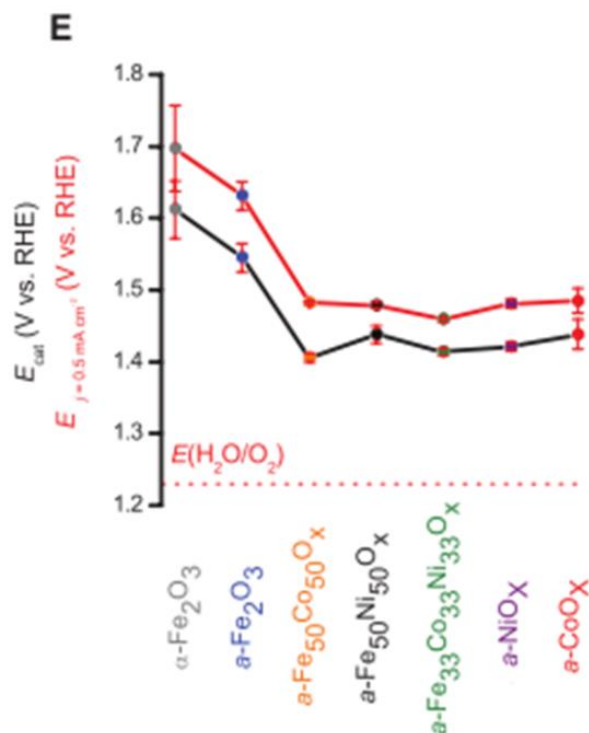


Figure 7 Overpotentials of amorphous metal oxide materials. ⁷¹

The Fe, Co, Ni three-phase diagram was studied and gave the result that the best catalytic parameters of the series were obtained from the film composed of $\text{Fe}_{20}\text{Ni}_{80}\text{O}_x$ ⁷². Two years later, further work was reported by Cuijuan Zhang and his co-workers⁷³. They prepared different ratios of amorphous ternary metal oxide and got ternary mapping of performance of Al/Fe/Ni, Al/Co/Ni and Al/Co/Fe water oxidation catalysts.

However, only a few studies about amorphous metal oxide material photo electrolysis⁷⁴ and photolysis⁷⁵ have been published. Horst Kisch *et al.*⁷⁴ reported that an amorphous microporous titania modified with transition metal salts showed a photoactivity and could be used to degrade 4-chlorophenol with visible light. Hui Cao and Steven L. Suib⁷⁵ reported that they prepared amorphous manganese oxide to be used as a photocatalyst for the oxidation of

2-propanol to acetone and it showed high activity under visible light at room temperature.

The most published research on amorphous metal oxide is when it is applied as thin-film transistors (TFT). With the development of smartphone and similar appliances, TFT materials became a hot topic as they are the core technique of touch screens. The amorphous metal oxide semiconductor is flexible, transparent and conductive which are natural properties of TFT. Indium oxide⁷⁶,⁷⁷ or the more complex indium gallium zinc oxide⁷⁸, are used to produce TFT materials.

1.9.2 Amorphous photoelectrodes

The main feature of amorphous oxides is the natural abundance of interfaces and defects. This might be the reason why there is little research about amorphous metal oxide materials being used as photoelectrochemical electrodes. Defects are a key factor in semiconductors since they can increase the carrier density but decrease carrier mobility.

The following formula is the relationship between electrical conductivity (σ), carrier density (n) and carrier mobility (μ). Here e is electron charge.

$$\sigma = ne\mu \quad \text{Eqn 5}$$

Amorphous oxides naturally have many carriers, but there is no obvious improvement to electrical conductivity due to low mobility. For electrocatalysis,

conductivity is dominated by carriers in either the conduction or valence band whereas for photoelectrolysis the photogenerated charges in both valence and conduction band move slowly and there is not enough time for them to react with water before recombination occurs.

There are only a few studies in the literature on amorphous oxide photocatalysts. However, these amorphous materials could not function without metal or other crystallized materials, unlike our samples prepared in this thesis.

Xinwei Li and his co-workers⁷⁹ prepared amorphous bismuth oxide/metal Bi photocatalyst. The decorated Bi metal activated amorphous bismuth oxide and improved the bulk defect recombination. However, the TEM images showed that the bismuth oxide only formed a very thin layer on the surface of the metallic Bi particles.

William D. Chemelewski and his co-workers⁸⁰ reported an amorphous FeOOH photoelectrode which showed enhanced performance in oxygen evolution reaction. However, the amorphous FeOOH absorbed less than 3% of solar photons. They therefore combined another light absorber layer to the amorphous catalyst to improve the photocurrent. The amorphous FeOOH film acted as a high activity electrocatalyst in this photoelectrode.

Amorphous oxides show good electric properties, however they perform poorly in the matters of carrier recombination and light absorption. However, there are some potential methods to improve the photo properties of amorphous oxide. Heavy post-transition-metal cations are reported to improve the carrier mobility in amorphous materials⁸¹. They form covalent bonding with the oxide which has a large covalent radius and spatially connect with other metal cations. This

makes a short path for carriers via the metal orbitals, unaffected by distorted metal-oxygen-metal chemical bonds in the amorphous metal oxide materials.

A large surface area can provide more active sites for reaction, and thin films are often used for decreasing the rate of recombination of photogenerated charges. Heterostructures may also provide an energy band structure to separate the electrons and holes at the interface.

1.10 Fe₂O₃ based photocatalyst

1.10.1 Fe₂O₃ catalyst

Fe₂O₃ is a good material that satisfies the requirements for photocatalysis. It is abundant on earth, non-toxic, low-cost and has a high stability. With a band gap of about 2.0 eV to 2.2 eV, it can absorb almost all UV light and most visible light comprising over 38% of the photons of sunlight (AM)⁸²⁻⁸⁵. However, despite its promising nature, Fe₂O₃ still has some drawbacks. Its poor oxygen generation rate, high electron-hole pairs recombination rate, short hole-diffusion length (~2–4 nm) and low carrier mobility (~10⁻¹ cm² V⁻¹ s⁻¹)⁸⁶ all lead to a low conversion efficiency. Also, due to the band positions, without bias, Fe₂O₃ could only generate oxygen, not hydrogen, due to its conduction band position.

1.10.2 Enhancement

Table 1 Photoresponses of doped hematite photoelectrodes⁸⁷

Dopant	Concentration	Technique	Photoresponses
W	0.0025%	Synthesized ceramics	IPCE 29% at 400 nm and 1.23 V_{RHE}
Mo	15%	Electrodeposition	IPCE 12% at 400 nm and 1.4 V_{RHE}
V	0.05%	Synthesized ceramics	IPCE 28% at 400 nm and 1.23 V_{RHE}
Nb	0.5%	Synthesized ceramics	IPCE 27% at 400 nm and 1.23 V_{RHE}
Nb	0.1%	Synthesized ceramics	135 cm^{-2} at 0.2 V_{SCE} (100 W Hg arc lamp, 20 $mW cm^{-2}$)
Nb	1.5%	Single crystal	IPCE 37% at 370 nm and 1.23 V_{RHE}
Nb	10%	Synthesized ceramics	IPCE 26.7% at 450 nm and 1.5 V_{RHE}
Ta	0.5%	Synthesized ceramics	IPCE 32% at 400 nm and 1.23 V_{RHE}
Ta	0.5%	Synthesized ceramics	640 $\mu A cm^{-2}$ at 0.7 V (a high-pressure lamp of 1 KW) (two-electrode setup)
Si	2%	Synthesized ceramics	IPCE 34% at 400 nm and 1.23 V_{RHE}
Si	2%	Synthesized ceramics	IPCE 9.3% at 340 nm and 1.49 V_{RHE}
Si	~1.5%	APCVD	IPCE 42% at 370 nm and 1.23 V_{RHE}
Si	5.3%	RMS	IPCE 2.5% at 375 nm and 1.54 V_{RHE}
Si	0.1%	SP	IPCE 23% at 360 nm and 1.4 V_{RHE}
Si	0.2%	SP	0.37 $mA cm^{-2}$ at 1.23 V_{RHE} (0.8 sun, AM 1.5)
Ti	5%	RMS	IPCE 14% at 375 nm and 1.54 V_{RHE}
Ti	4%	RBD	IPCE 31% at 360 nm and 1.4 V_{RHE}
Ti	2.5%	PVD	IPCE 15% at 360 nm and 1.6 V_{RHE}
Ti	1%	Synthesized ceramics	IPCE 1.2% at 340 nm and 1.49 V_{RHE}
Ge	0.05%	Synthesized ceramics	IPCE 5.5% at 340 nm and 1.44 V_{RHE}
Zr	0.5%	Synthesized ceramics	IPCE 23% at 400 nm and 1.23 V_{RHE}
Zr	2.0%	Electrodeposition	2.1 $mA cm^{-2}$ at 1.64 V_{RHE} (Xe lamp, 150 $mW cm^{-2}$)
Ru	5%	Synthesized ceramics	108 $\mu A cm^{-2}$ at 0.2 V_{SCE} (100 W Hg arc, 20 $mW cm^{-2}$)
Sn	4%	RBD	IPCE 21% at 360 nm and 1.4 V_{RHE}
Sn	0.05%	Synthesized ceramics	IPCE 4.0% at 340 nm and 1.04 V_{RHE}
Sn	4%	Deposition annealing	IPCE 0.7% at 420 nm and 0.3 V vs. Ag/AgCl (0.2 M NaOH)
Sn	9.4%	Hydrothermal method	IPCE 19.2% at 400 nm and 1.23 V_{RHE} 1.86 $mA cm^{-2}$ at 1.23 V_{RHE} (AM 1.5 G)
Ce	0.05%	Synthesized ceramics	IPCE 30% at 400 nm and 1.23 V_{RHE}
Hf	0.002%	Synthesized ceramics	IPCE 26% at 400 nm and 1.23 V_{RHE}
Pt	5%	Electrodeposition	IPCE ~12% at 400 nm and 1.4 V_{RHE}
Pt	5%	Hydrothermal	1.38 $mA cm^{-2}$ at 1.25 V_{RHE} under 1 sun illumination
Al	0.46%	Electrodeposition	IPCE 8% at 400 nm and 1.4 V_{RHE}
Cr	5%	Electrodeposition	IPCE 6% at 400 nm and 1.4 V_{RHE}
In	8–20%	Sputtering	21% at 400 nm and 1.5 V_{RHE} (effective quantum efficiency)
Mg	1%	Plasma sprayed	2.1% at 400 nm and -0.4 V (cathodic) vs. V_{SCE} (pH 13) 0.84% at 400 nm and +0.5 V (anodic) vs. V_{SCE} (pH 13)
Ca	1%	Synthesized ceramics	—
Ni	5%	Spray pyrolysis	0.26 $mA cm^{-2}$ at 0.59 V_{NHE} (500 W Xe)
Cu	5%	Spray pyrolysis	66.8 $\mu A cm^{-2}$ at 1.61 V_{RHE} (150 W Xe lamp)
Zn	5%	Spray pyrolysis	422.6 $\mu A cm^{-2}$ at 1.61 V_{RHE} (150 W Xe lamp)
Zn	5%	Spray pyrolysis	0.64 $mA cm^{-2}$ at 1.71 V_{RHE} (150 W Xe lamp)
Cd ^b	~1%	Electrodeposition	1.25 $mA cm^{-2}$ at 1.23 V_{RHE} (AM 1.5)
Si + Ti	4%Si + 2%Ti	USP	IPCE 37% at 370 nm and 1.23 V_{RHE}
Be + Sn	6%Be + 4%Sn	Deposition annealing	IPCE 1.2% at 420 nm and 0.3 V vs. Ag/AgCl (0.2 M NaOH)
Ti + Al	5%Ti + 1%Al	Spray pyrolysis	IPCE 25% at 400 nm and 0.7 V_{NHE}
Ti + Li	5%Ti + 1%Li	Spray pyrolysis	0.9 $mA cm^{-2}$ at 0.5 V_{NHE} (500 W Xe)

To improve the efficiency of Fe_2O_3 , many methods have been developed, such as doping, surface modification, unique nanostructure, homo/heterojunction *etc.* Pure α - Fe_2O_3 shows low conversion efficiency due to the high carrier recombination rate, low carrier mobility and short hole-diffusion length. Doping has been widely used to improve the carrier concentration and the conductivity

of hematite. Table 1 lists the research results for doped hematite photoelectrodes created from a variety of elements.

Generally, if a dopant element has a valence state larger than +3, such as Sn⁸⁸⁻⁹¹, Ti^{90, 92-94}, Zr^{95, 96} and Si^{92, 96-98}, these +4 dopants act as electron donors when replacing Fe in hematite. Thus, the doped hematite improves the donor density and probably improves the electrical properties. On the other hand, if the dopant element has a valence state smaller than +3, for example Zn^{99, 100}, Mg^{101, 102}, Cu^{99, 103}, Li¹⁰⁴, and Ni^{104, 105}, the dopants would act as electron acceptor.

Naghmehalsadat Mirbagheri *et al*¹⁰⁶ electrodeposited Zn and Ti doped Fe₂O₃ on FTO glass in a mixed solution containing 5 mM FeCl₃, 5 mM KF, 0.1 M KCl, and 1 M H₂O₂, following annealing at 800°C. The obtained modified samples showed improved photo current than the pristine Fe₂O₃ sample. The samples prepared from 1.40% Ti + 5.58% Zn-containing solutions demonstrated a photocurrent density 2.5 times higher than that of the pristine hematite electrode at 1.23 V vs RHE (1.5 mA cm⁻²). The Ti dopant induced high donor density (5 times higher than pristine) and Zn dopant increased the width of the space-charge region and improve the charge separation. As a result, the photo current was improved compared to pristine hematite.

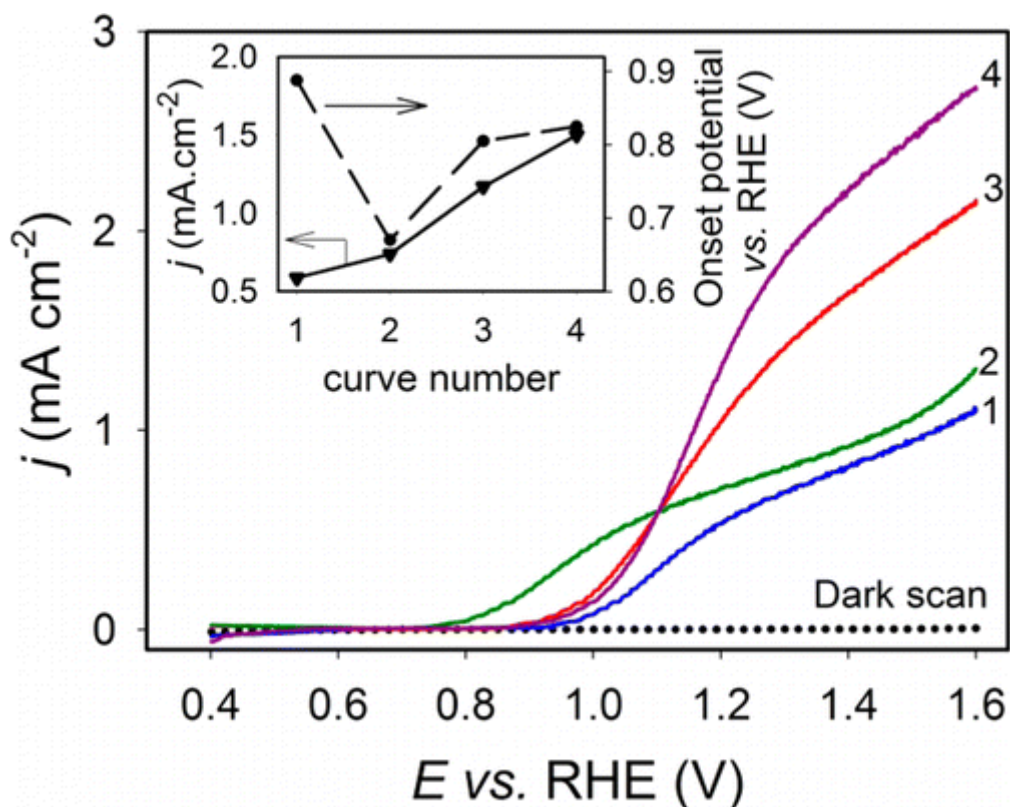


Figure 8 Representative current–potential curves in the dark (dotted line) and under simulated illumination (solid curves) recorded for (1) pristine hematite, (2) 10.71% Zn, (3) 1.96% Ti, and (4) 1.40% Ti + 5.58% Zn-modified hematite electrodes. Inset: the photocurrent onset potential (dashed line) and current density (solid line) at 1.23 V vs RHE for the hematite and modified-hematite electrodes¹⁰⁶.

Diane K. Zhong and her co-worker¹⁰⁷ has reported a surface electrodeposited Co-Pi doped hematite photoanode with a sustained 5-fold enhancement in the photocurrent density. The O₂ evolution rate was observed at +1.0 V vs RHE. They decreased the deposition time to form a more sparse deposition of Co-Pi onto hematite. The hematite therefore absorbs light and the Co-Pi acts as an oxidization centre.

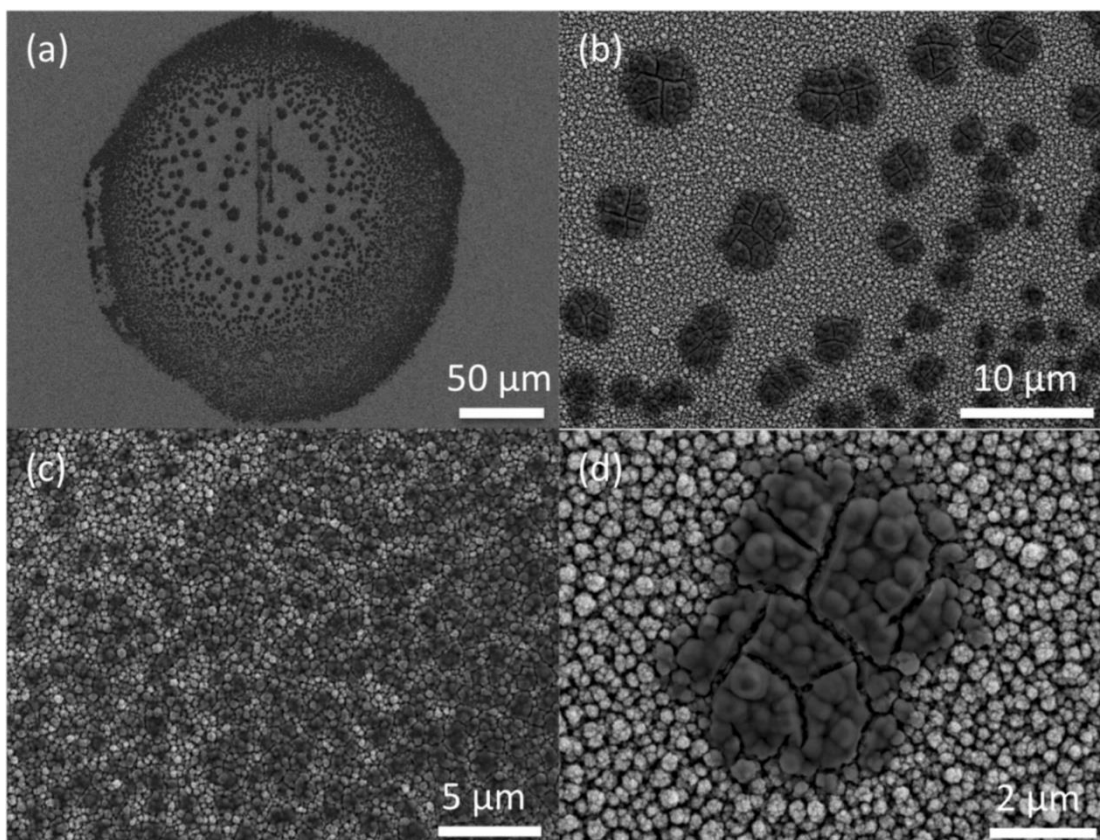


Figure 9 SEM of Co–Pi/ α -Fe₂O₃ composite photoanodes showing (a) ring-like deposition of Co–Pi in selective areas of the α -Fe₂O₃ surface and (b–d) magnified views of Co–Pi patches within this ring. (d) Co–Pi conforming to the topology of the underlying α -Fe₂O₃ mesostructure. The cracks in the Co–Pi result from drying¹⁰⁷.

Asif Ali Tahir *et al*¹⁰⁸ prepared nanostructured thin film hematite for water splitting. They synthesized $[\text{Fe}_6(\text{PhCOO})_{10}(\text{acac})_2(\text{O})_2(\text{OH})_2]_3\text{C}_7\text{H}_8$ as precursor and used Aerosol-assisted chemical vapor deposition (AACVD) to prepare hematite thin film on FTO glass. The crystalline nanostructured hematite films, comprising needle-like features 100–160 nm long with a diameter of 30–50 nm, resulted in improved photocurrent density of 600 $\mu\text{A cm}^{-2}$ at 1.23 V vs RHE. XPS confirmed that Fe is present only in the Fe³⁺

oxidation state. Mott-Schottky plots showed that the donor density of the α - Fe_2O_3 was $2.914 \times 10^{23} \text{ m}^{-3}$.

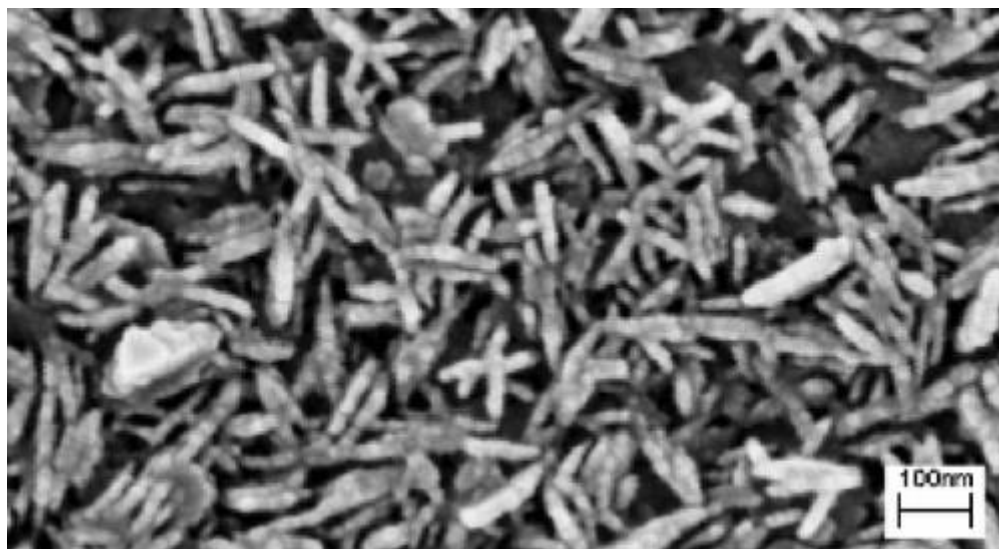


Figure 10 SEM image of needle-like Fe_2O_3 thin film, composed of small individual nanoparticles¹⁰⁸.

Yaoming Wang *et al*¹⁰⁹ reported a $\text{SrTiO}_3/\alpha\text{-Fe}_2\text{O}_3$ heterojunction photoanode which, in comparison to single SrTiO_3 or $\alpha\text{-Fe}_2\text{O}_3$ films, performs higher photocurrent and the incident photon to current conversion efficiencies. The research results indicated weak mobility of holes photo-generated in $\alpha\text{-Fe}_2\text{O}_3$ and strong mobility of holes excited in SrTiO_3 . Due to the special band structure, SrTiO_3 improved the separation efficiency of charge carriers which had been photo-generated in $\alpha\text{-Fe}_2\text{O}_3$. Thus, the heterojunction enhanced the photo current density and conversion efficiency.

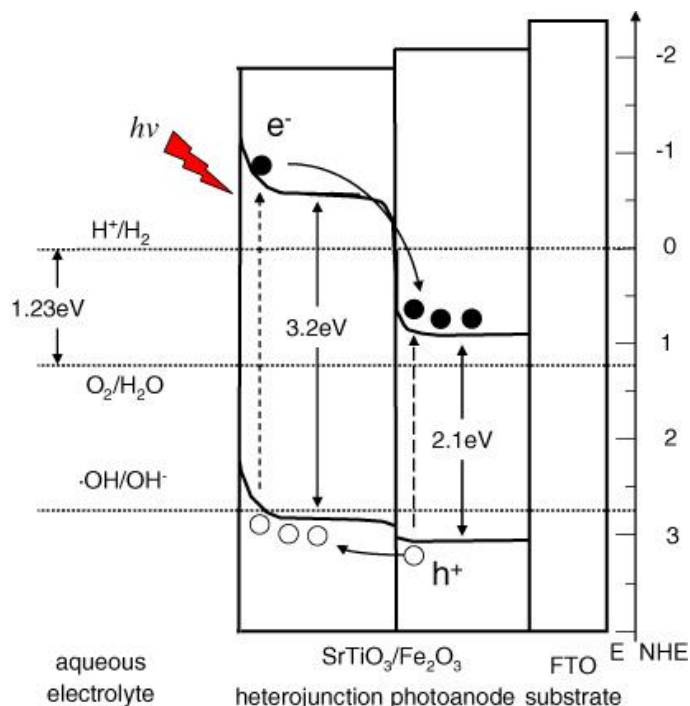


Figure 11 The schematic diagram of the energy band structure of the $\text{SrTiO}_3/\alpha\text{-Fe}_2\text{O}_3$ heterojunction¹⁰⁹.

The low mobility and high recombination rate of Fe_2O_3 are assumed to be owing to the defect (surface state) which acted as a recombination centre^{110, 111}. Wenjun Luo *et al*¹¹² found that the surface state could be changed irreversibly by pretreatment, increasing photocurrent by a factor of three. Nathan T. Hahn *et al*¹¹³ also reported that thin film (18–70 nm) and higher temperature (500–550°C) could improve the crystalline order and decrease the surface defects. In this project, we tried surface modification by the dip-coating method to improve the mobility and lower the recombination rate. All the modified samples have shown improved photo current compared to unmodified pure Fe_2O_3 electrodes.

1.11 Electrospinning method

Electrospinning is a promising method by which to prepare materials with high surface areas. It has been used to synthesize polymer nanofibers¹¹⁴, carbon nanofibers^{115, 116}, semiconductor nanomaterials¹¹⁷⁻¹²⁰, organic-inorganic hybrid nanofibers^{121, 122} and functional nonwoven mats^{123, 124}. Electrospinning is a very simple and versatile method, and the equipment could be set up easily using common materials in the lab.

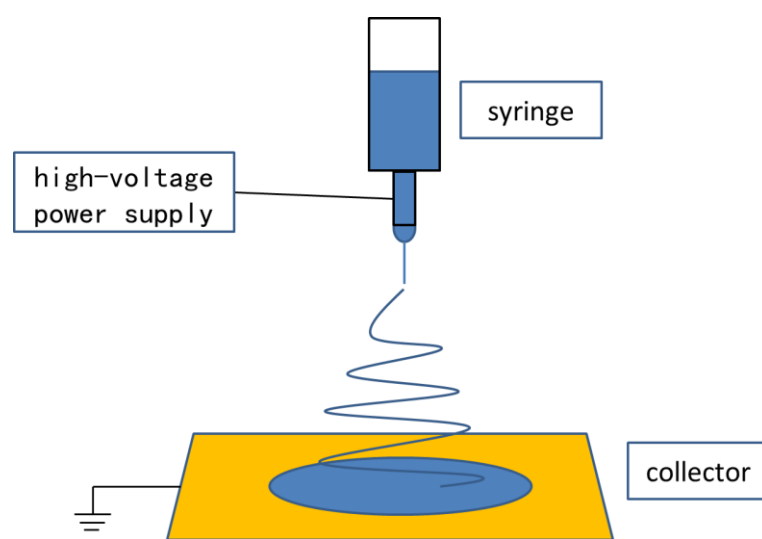


Figure 12 Schematic diagram of electrospinning.

Figure 12 represents a scheme of typical electrospinning equipment. The precursor, normally a conductive solution with proper viscosity (commonly affected by polymer additions), is placed in a syringe with a metal needle. The collector is also conductive, such as tinfoil, or an aluminium plate *etc.* The needle is connected to a high-voltage power supply and the collector is ground connected. As a result, the conductive precursor solution will fly to the collector under the very high electrostatic force. The solution is extracted to form very fine fibres which result in solid nanofibers due to the solvent evaporation.

The final sample of electrospinning could be affected by various parameters:

- a) System parameters: such as the relative molecular mass of the precursor solution polymer and properties of the solvent. These parameters could affect the viscosity of the precursor which will determine the thickness of the nanofibers. If the viscosity is too low, the solution will be hard to keep in a continuous flow and will become separate droplets (which is another synthetic technology called electrospray). In addition, the conductivity, surface tension and dielectric constant of the solvent could affect the final sample as well.
- b) Process parameters: including concentration, applied potential, distance between needle and collector, *etc.* Generally, lower concentration and higher applied potential will create thinner fibres. The spin distance is more complex, as it affects both the electric-field intensity and spinning time.
- c) Environmental parameters: for instance, the temperature, humidity and air velocity. These parameters influence the evaporation of the solvent and the stability of the spinning process.

By controlling the aforesaid parameters, the nanofibers could have different morphologies, such as “necklace”¹²⁵, hollow nanotube¹²⁶, rice-grain shape, unique pattern¹²⁴, “firecracker” shape¹²⁷, *etc.*

1.12 Project aims

As discussed in this chapter, there are many different factors in the research into photoelectrodes. To improve the efficiency of semiconductor photoelectrodes, many methods have been used in previous works, such as doping, co-catalysts, specific structure and morphology.

A photoelectrode based on amorphous metal oxide materials will be prepared and discussed in chapter 2. Due to the long-range disorder, amorphous materials have abundant defects which play an important role in semiconductor conductivity. However, the disadvantage is the low carrier mobility meaning the photo-induced electron-hole pairs do not have adequate time to move to the interface for the reactions. To prepare an amorphous metal oxide photoelectrode with enhanced photo properties, Pb, Bi and Sn oxides will be used to prepare amorphous transparent film on FTO glass. Doping with amorphous Fe, Co and Cu oxide and WO_3 nanoparticles will be applied and discussed.

Synthesis and characterization of an Fe_2O_3 film electrode by surface modification will be presented in chapter 3. The surface state could act as recombination centre and trap holes generated in the valence band, and electrons generated in the conduction band. By decreasing the surface state, the carrier mobility could be improved, the recombination rate could be lower, and the photo current would be enhanced. To achieve the project aim, gentle methods which are easily repeated will be applied.

The preparation and characterization of a CdS/F- SnO_2 fiber photoelectrode will be described in chapter 4. Electrospinning will be applied to prepare the unique nonwoven mat structure precursor.

All photoelectrodes will be tested using photoelectrochemistry system. An Xe lamp through a 420 nm band pass filter with an irradiance of 1 sun will be used as the light source.

The main aims of this project are as following:

1 Prepare amorphous oxide photoelectrodes. Improve their photo properties by doping and co-catalysts. Characterize and improve modification methods for these photoelectrodes.

2 Develop surface modification methods to improve the photo response of hematite photoelectrodes. Prepare and compare the effect of different metal ions. Control the parameters and optimize the experiment conditions.

3 Use electrospinning to prepare a conductive substrate with 3D structured surface. Load photocatalysts on this substrate for better photo properties.

Chapter 2

The preparation and
characterization of amorphous
metal oxide photoelectrodes

2 The preparation and characterization of amorphous metal oxide photoelectrodes

2.1 Introduction

Amorphous materials, due to their specific structure (unlike crystalline materials), have been used as recording ^{63, 64}, solar cell⁶⁵, electrode⁶⁶, gas sensor⁶⁷⁻⁷⁰ and catalyst materials. Amorphous materials have higher defect density, which is a key factor for semiconductors as regards to electron/hole generation and recombination. To synthesize and enhance the amorphous photoelectrode, gentle preparing method was applied.

The method used in this chapter is photochemical metal-organic deposition (PMOD)^{68, 70, 72, 128} which has, of recent years, been commonly used to prepare transition metal oxides. The organic metal salts are prepared as a precursor, after which the organic groups are degraded by irradiation under UV light. In this way the amorphous metal oxide sample is obtained. In this method, the sample is unheated to avoid the crystallizing. Also, as the precursor is liquid it can be prepared on different substrates without any limitation (such as large area or curved substrates). The PMOD method can be used to prepare a very thin film of metallic materials or metallic oxides, and can control the thickness of the film and number of layers. In this chapter, the organic metal film precursors are prepared on FTO glass by spin coating the precursor solution, in this case Ethylhexanoate (EH) salts. The molecular formula is shown below:

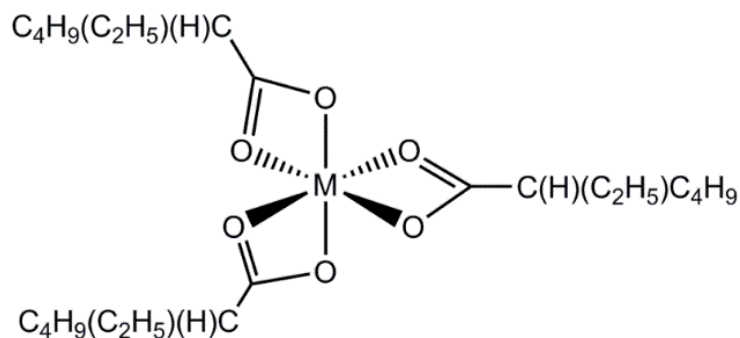


Figure 13 The molecular formula ethylhexanoate (EH) salt which is used in this chapter. M is the metal element.

As a three-elements metal oxide material, the effect of different ratios was studied. Also, different methods were tried such as doping and co-catalysts, in order to enhance the photo properties.

2.2 Chapter aim

The aim of this chapter is to investigate if amorphous metal oxide materials could be used for photoelectrode catalysts, and, if so, how then to enhance them.

Due to the long-range disorder, amorphous materials have abundant defects which play an important role in semiconductor conductivity. However, the disadvantage is their low carrier mobility which is of great importance for photoelectrochemistry materials, and which means the photo-induced electron-hole pairs do not have adequate time to move to the interface for the reactions.

To achieve the aim, several areas were studied:

- The use of Pb, Bi and Sn oxides, which contain large spherical valence orbitals, to obtain s-based bands that are insensitive to directional chemical bonding.
- Experimenting with different factors during the preparation, included calcining temperature, the volume and the concentration of the precursor, in order to control film thickness and the ratio of Pb-Bi-Sn.
- Doping with amorphous Fe, Co, Cu oxide, and WO_3 nanoparticles to improve the light absorption properties.
- Layer-by-layer structures of different metal oxides to improve hole-electron pair separation.

A repeatable experiment process was followed to meet the requirements below:

- Easily adjustable synthetic parameters, which include the quantity of metal oxides, the thickness of the films and the order of deposition of different metal oxide layers.
- Ensuring the experimental conditions of the characterisation are the same to compare the photoelectrochemistry results of different electrode materials.

The following methods were used:

- Convincing characterization to show the composition, microstructure and morphology (SEM, TEM, EDX, XPS, XRF and XRD);
- To study light absorption (UV-vis absorption);

- Photoelectrochemical properties using Linear sweep voltammetry (LSV) method to show the samples' electrochemical properties and photoelectrochemical properties under visible light, controlled potential electrolysis (CPE) to show the samples' photo electrochemical properties under visible light and stability, incident photon-to-current efficiency (IPCE) experiment to show the samples' quantum efficiency.

2.3 Results and discussion

2.3.1 Synthesis of the films

The experiment focussed on amorphous films on the transparent conducting substrate FTO glass to work as a photoanode. The Pb-Bi-Sn oxide amorphous film on FTO glass was made in three steps based on previous work used to prepare amorphous films from Fe, Ni and Co oxides⁷¹. The mixed metal complex precursor was dropped on the FTO glass substrate and then spin-coated at 3000 rpm for 1 minute. Then the substrate was irradiated under UV light until the organic acid ligand degraded completely, which was judged by FTIR. Lastly, the substrate was heated at 100°C to obtain the final sample.

Samples are named as for the following form.



“PbBiSn” means that this sample is mixed PbBiSn oxide with the ratio of Pb, Bi and Sn being 1:1:1. “c” is the concentration of the precursor and “v” is the

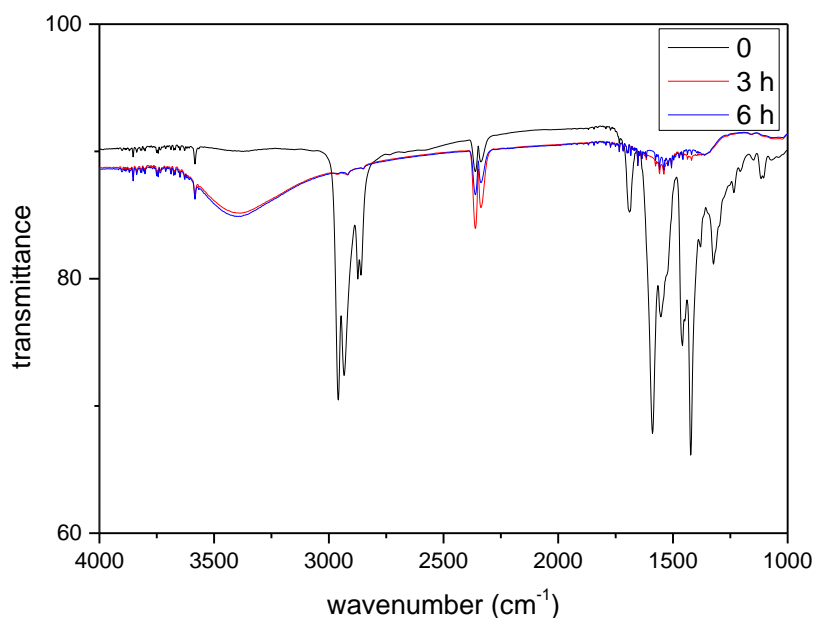
volume used in the spin-coating process. The detailed parameters of samples tested in this chapter are listed in Table 2.

Table 2 The samples used to collect the data for the photocurrent phase diagrams. The ratio of Pb Bi and Sn is the relative atomic ratio.

volume (μL)	Concentration (%, w/w)	Pb	Bi	Sn	volume (μL)	Concentration (%, w/w)	Pb	Bi	Sn
10	7.5	1	0	0	20	7.5	1/3	1/3	1/3
10	7.5	0	1	0	40	7.5	1/3	1/3	1/3
10	7.5	0	0	1	80	7.5	1/3	1/3	1/3
10	7.5	0.75	0.25	0	10	15	1/3	1/3	1/3
10	7.5	0.75	0	0.25	20	15	1/3	1/3	1/3
10	7.5	0.5	0.5	0	40	15	1/3	1/3	1/3
10	7.5	0.5	0	0.5	10	22.5	1/3	1/3	1/3
10	7.5	0.25	0.75	0	20	22.5	1/3	1/3	1/3
10	7.5	0.25	0	0.75	40	22.5	1/3	1/3	1/3
10	7.5	0	0.25	0.75	10	30	1/3	1/3	1/3
10	7.5	0	0.5	0.5	20	30	1/3	1/3	1/3
10	7.5	0	0.75	0.25	40	30	1/3	1/3	1/3
10	7.5	1/3	1/3	1/3	10	37.5	1/3	1/3	1/3
10	7.5	1/6	2/6	3/6	20	37.5	1/3	1/3	1/3
10	7.5	1/6	3/6	2/6	40	37.5	1/3	1/3	1/3
10	7.5	2/6	1/6	3/6	10	45	1/3	1/3	1/3
10	7.5	2/6	3/6	1/6	20	45	1/3	1/3	1/3
10	7.5	3/6	1/6	2/6	40	45	1/3	1/3	1/3
10	7.5	3/6	2/6	1/6	10	52.5	1/3	1/3	1/3
					20	52.5	1/3	1/3	1/3
					40	52.5	1/3	1/3	1/3

A sample was prepared on a KBr disc substrate (radius of 1cm) for an FTIR experiment to confirm the decomposition of organic groups. Precursor solution was dropped on the disc for spin-coating and then irradiated under UV light. During the irradiation, the KBr disc sample was measured by FTIR every 3 hours until the vibration peaks of 2-ethylhexanoate ligand had disappeared. Figure 14 shows example FTIR spectra. The 2-ethylhexanoate shows a strong

absorption peak (1421 cm^{-1} and 1587 cm^{-1})⁷¹ on the FTIR spectrum so that its disappearance is the obvious signal of decomposition of 2-ethylhexanoate. In this case, peaks had almost disappeared after 3 hours' irradiation.



*Figure 14 FTIR spectrum of sample using $Fe_{80}^{*7.5}$ after different time periods of UV irradiation.*

2.3.2 Morphology and composition

2.3.2.1 Scanning Electron Microscopy (SEM) and Energy Dispersive Analysis of X-rays (EDX)

SEM was performed on the amorphous photoelectrode sample to examine the morphology. Linear sweep EDX and mapping EDX experiments were performed to get details of the composition and distribution of elements. SEM and EDX images are shown in Figure 15 and Figure 16.

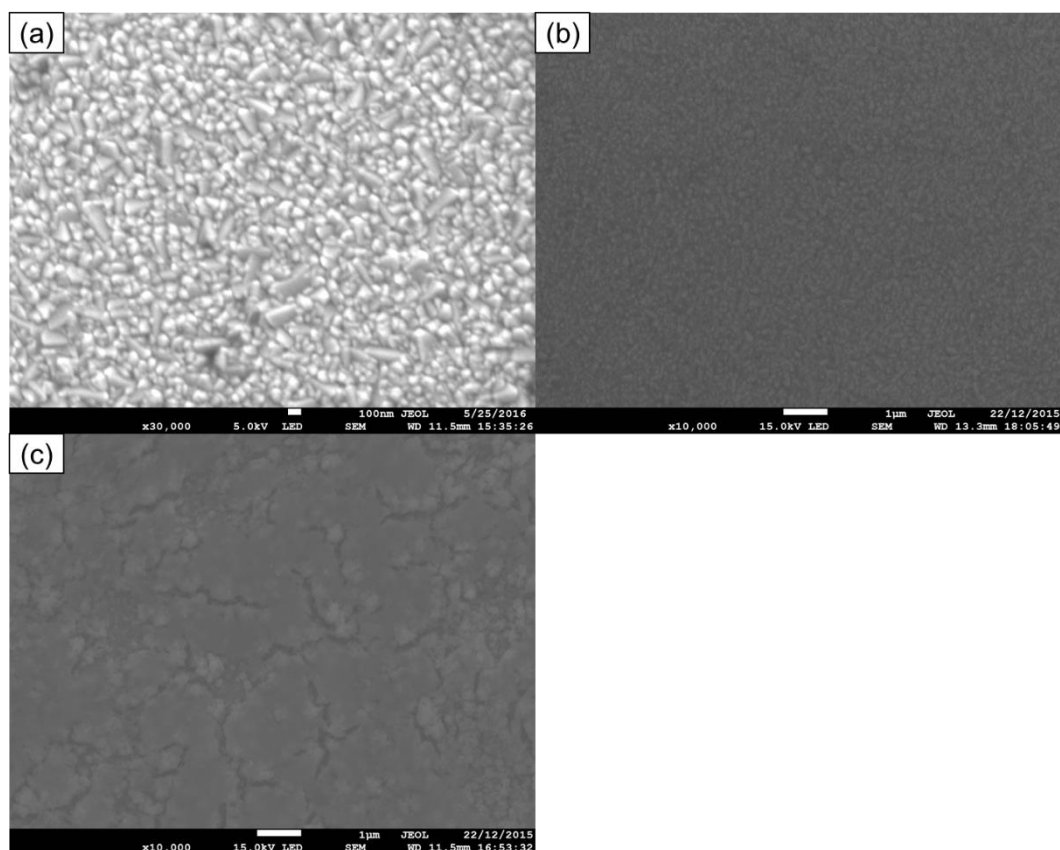


*Figure 15 Surface SEM images of (a) FTO glass, (b) $PbBiSn_{7.5*10}$ and (c) $PbBiSn_{52.5*40}$.*

Figure 15 shows the surface images of pure FTO glass and samples with different precursors. The surface of $PbBiSn_{7.5*10}$ is a thin film and the particles of FTO could clearly be seen. The film on $PbBiSn_{52.5*40}$, however, has some cracks due to its greater thickness.

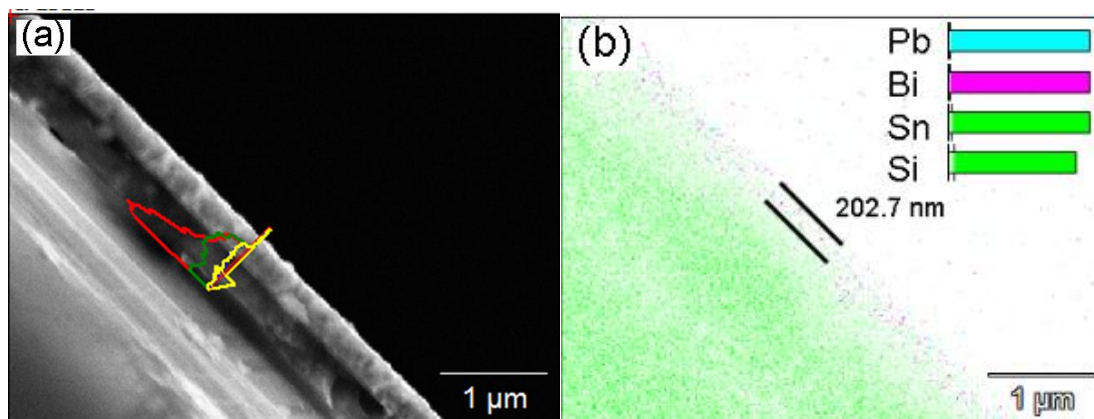
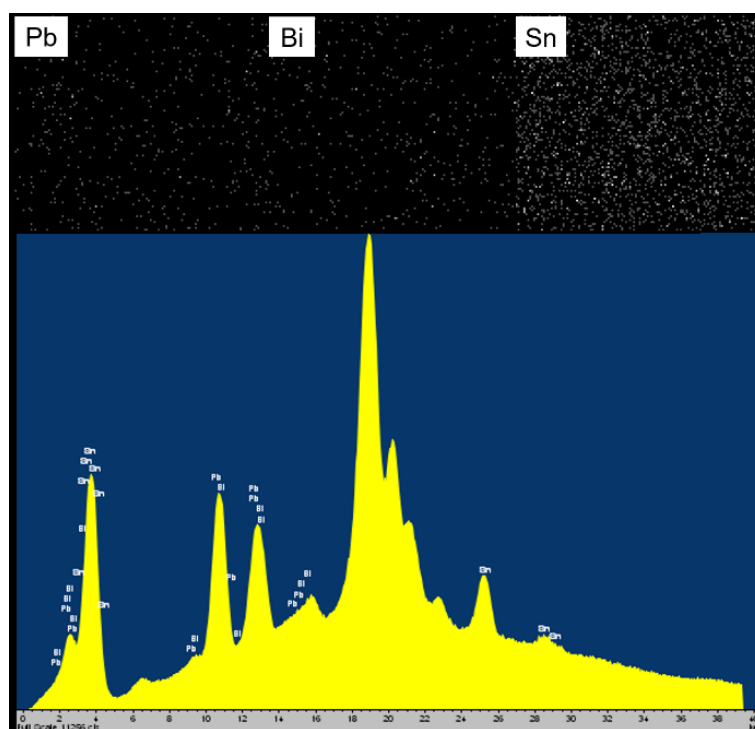


Figure 16 SEM/EDX images of $PbBiSn_{7.5*10}$ heated at $100^{\circ}C$. (a) SEM image and linear sweep EDX of cross section, where red line is for Si, green line for Sn, blue line for Pb and yellow line for Bi. (b) Elements mapping of cross section.

The SEM of the cross section shows that a flat thin film is attached to the surface of the glass which is in the bottom left area. Red, green, blue and yellow lines in Figure 16 (a) mean the intensity of the signal of Si, Sn, Pb and Bi, respectively. From left to right, the signal of Si, which corresponds to glass, is stronger than the others and then decreases significantly. The lines of Sn, Pb and Bi remain flat and only slightly increase along the line from left to right due to the Pb-Bi-Sn film. The signal of Sn is larger than that of Bi and Pb because there is a very thin film of FTO (F-doped SnO_2). The linear sweep EDX proved the existence of PbBiSn oxide film. However, due to the naturally poor conductivity, the amorphous metal oxide samples drifted seriously under high magnification, and the interface between PbBiSn film and FTO glass is not clearly seen. To get better evidence, mapping EDX images were obtained and put layer-over-layer in Figure 16 (b). In this mapping image, the bottom left area is green, corresponding to the glass. The amorphous film lies on the surface of glass clearly represented by the colourful layer. By calculation, the thickness of the film is about 200nm.

2.3.2.2 X-ray fluorescence (XRF)



*Figure 17 XRF mapping of Pb, Bi and Sn and XRF spectrum of central area of a PbBiSn_{7.5*10} film.*

XRF can provide details of element concentration from the thin films. Figure 17 shows the surface element mappings (top three figures) and EDX analysis (bottom). The mapping images show that the three metal elements Pb, Bi and Sn were homogeneous throughout the whole film on PbBiSn_{7.5*10}. Consistent with the SEM/EDX result mentioned in chapter 2.3.2.1, the intensity of Sn is greater than that of Pb and Bi because Sn is also present in the FTO substrate. The concentration of Pb and Bi are at almost the same level which is as

expected. The XRF spectrum in Figure 17 was obtained from the central area of the sample, and proves the existence of Pb, Bi and Sn.

2.3.2.3 X-ray photoelectron spectroscopy (XPS)

The previous EDX experiments are a type of observational measurement because of the low resolution. To get more details of the elements' distribution and concentration, X-ray photoelectron spectroscopy (XPS) was performed. XPS experiment uses x-rays to irradiate a sample and generate photoelectrons. The instrument detects the energy of the photoelectrons and obtains an analysis of the XPS spectrum, the oxidation state and concentration of elements in the surface.

*Table 3 The proportion of different valence states of Pb, Bi and Sn in PbBiSn_{7.5}*₁₀ films following changes during the PEC experiment. (Proportion of PbO was calculated from Pb₃O₄.)*

	Element source	Before PEC	After PEC
%Bi ₂ O ₃	100	100	96.06
%Bi metal	0	0	3.94
%PbO ₂	0	67.81	44.06
%PbO	100	32.19	55.94
%SnO ₂	0	39.54	0
%SnO	100	60.46	100

Here, XPS data were obtained of films before and after photoelectrochemistry (Table 3) and a depth profile analysis was obtained of a film before PEC (Figure 18). As the XPS experiments only detect the detail of atoms near the thin

surface rather than in the deeper area, this technique is always used to give information about the surface of samples (Table 3). However, as the technique developed, it began to be used additionally to detect depth details. To achieve this, the surface layer of the sample is removed using another combined technique (such as ion sputtering^{129, 130}) after measurement. The process is repeated and the data from each layer collected. By this method, we could ascertain changes to each element at different depths.

XPS measurements were performed for used $\text{PbBiSn}_{7.5*10}$, $\text{PbBi}_{7.5*10}$, $\text{PbSn}_{7.5*10}$ and $\text{BiSn}_{7.5*10}$ samples and fresh $\text{PbBiSn}_{7.5*10}$ samples. Here “fresh sample” means that the sample had not previously been used for the PEC experiment, whereas “used sample” means it had.

Table 3 shows comparison of fresh and used $\text{PbBiSn}_{7.5*10}$ which could provide information about what may have changed during the PEC experiment. According to the data, these three elements were to some extent reduced after PEC, and the average valence states of Bi, Pb and Sn were decreased. This is probably because the surface of the photoelectrode was activated in the aqueous electrolyte or due to the absorption of water species. Another notable point is that the valence states of Pb and Sn in the film were not the same as they were in the metal precursor. The possible reason is the preparing process, which includes UV irradiation and 100°C heat treatment in air. This may lead to the oxidation of metal elements.

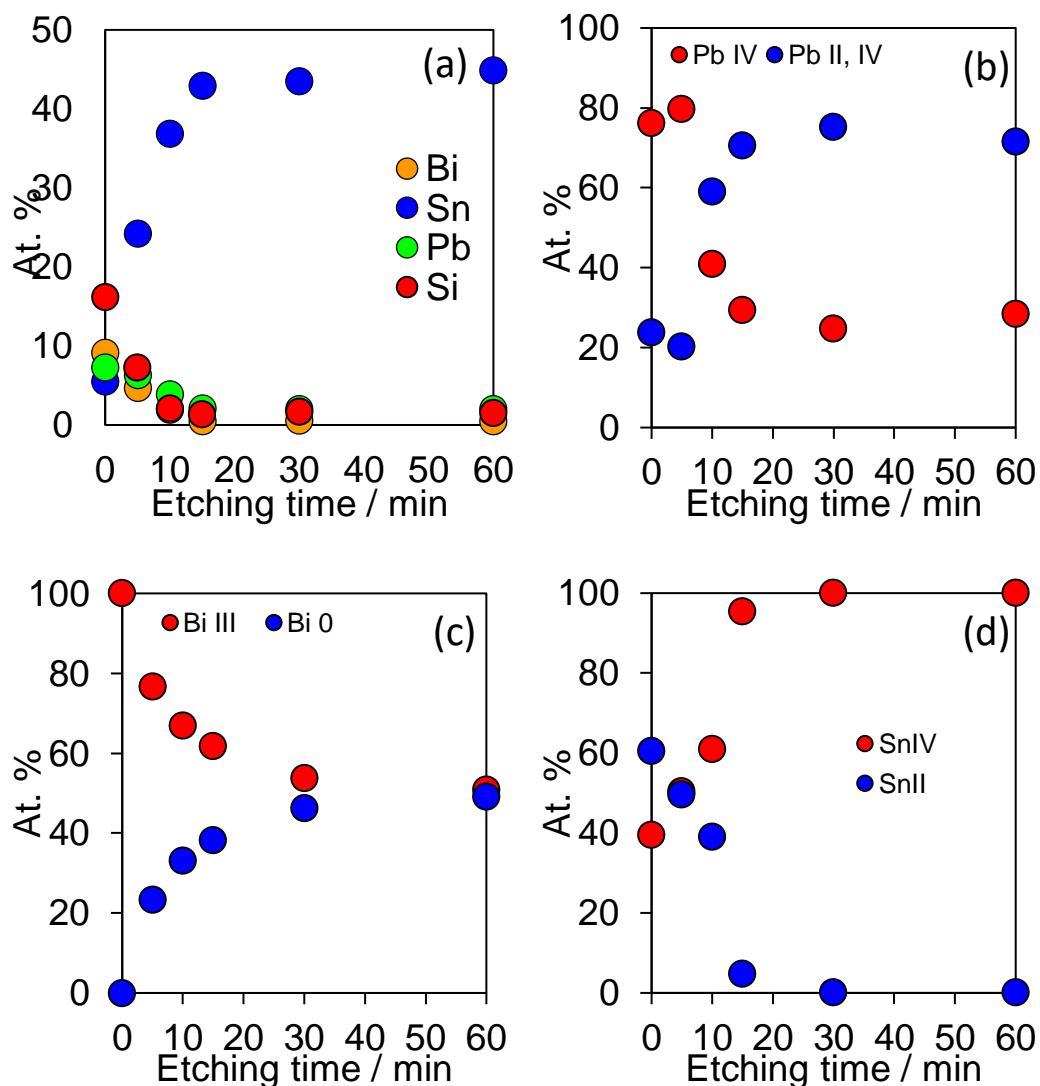


Figure 18 Etching depth profiling quantification of (a) all elements, (b) Pb, (c) Bi and (d) Sn in $\text{PbBiSn}_{7.5 \times 10}$ film before PEC (fresh $\text{PbBiSn}_{7.5 \times 10}$).

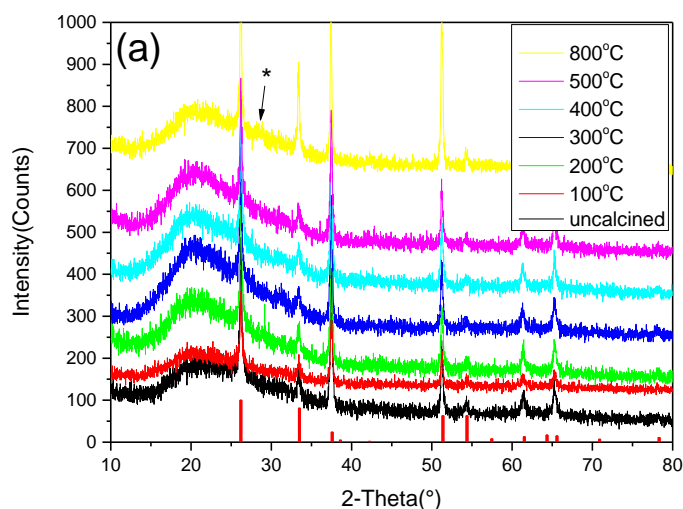
Etching XPS measurement was carried out and successive XPS spectra acquired in order to study further the differences to the metal elements throughout the film thickness. Figure 18 shows the depth profiling quantification of every element in fresh $\text{PbBiSn}_{7.5 \times 10}$ film. At the surface level of the film (etching time=0), the proportion of the three elements is almost equal to that in the data shown in Table 3. As the etching time grows, deeper levels were

measured. Figure 18 (a) shows that the proportion of Sn grows the fastest of all elements. After about 15 minutes of etching, it is almost 100 % SnO₂ due to the FTO substrate layer.

Figure 18 (b), (c) and (d) show the valence state change along the depth. According to the etching time, the data at 15 minutes could be interpreted as the bottom layer of the amorphous film. It seems that the proportion of different valence states in the bottom layer is similar to the data of used PbBiSn_{7.5*10} film, shown in Table 3. Considering the XPS experiment only measures the very top layer of the film sample, we assume that the photoelectrode was activated during the PEC experiment, and that due to the surface activation and species absorption, the valence states of the metal ions near the surface were reduced. When photoinduced electrons and holes were generated and transferred to the FTO glass and the surface, the higher holes transferred to the surface and oxidized the water, while some electrons reacted with metal elements before transferred to the FTO layer. The metal ions acted as electron acceptors.

2.3.3 Structure

2.3.3.1 X-ray diffraction (XRD)



v

Figure 19 XRD pattern of (a) $PbBiSn_{7.5*10}$ samples heated at different temperatures for 1 hour and (b) $PbBiSn_{7.5*10}$ samples prepared with different volumes of precursor. The red vertical bars are the standard spectrum of FTO glass.

XRD was carried out to study whether the films are amorphous. For crystalline materials, the ordered crystal lattice shows obvious sharp peaks in the XRD pattern, however, no peak will be found in amorphous materials. Figure 19 is the XRD spectra of $PbBiSn_{7.5*10}$ samples with different parameters. The patterns show clear peaks of FTO glass, and no other peaks have been found. All the samples obtained in this project have the same feature: that no obvious peak of Pb-Bi-Sn oxide could be found, even when the samples have been heating under 500°C in air. However, one peak not from FTO was observed in the XRD spectrum of the 800°C heated sample. We assume that the $PbBiSn$ oxide films could transform into crystalline structure after calcination at high temperatures in air, and that they were already to some extent crystallized when heated to 800°C. This proved that the temperature and volume of the precursor did not affect the amorphous structure which is stable under heating to 500°C.

2.3.3.2 Light absorption (UV-vis absorption and visible appearance)

Light absorption by photoelectrode materials is critical to the photo current obtained and to the solar-to-fuel efficiency. To study light absorption, UV-vis absorption experiments were carried out and the results are shown in Figure 20.

Different parameters were tested and shown in Figure 20, including the concentration and volume of the precursor and the doping ratio of different dopants. The absorbance increased for samples where the precursor was of higher concentration (Figure 20 (a)) or higher volume (Figure 20 (b)) due to more absorber ions. This is consistent with the colour is shown in the photograph (Figure 21). An exception is $\text{PbBiSn}_{37.5*10}$, which may be due to uneven film in the preparation process. Noticeably, the sample heated at 500°C shows a very low absorbance which is consistent with the photograph (Figure 21 (j)). The possible reason is that the heating treatment increased the crystallinity and decreased the defect density which acts as a key role in light absorption.

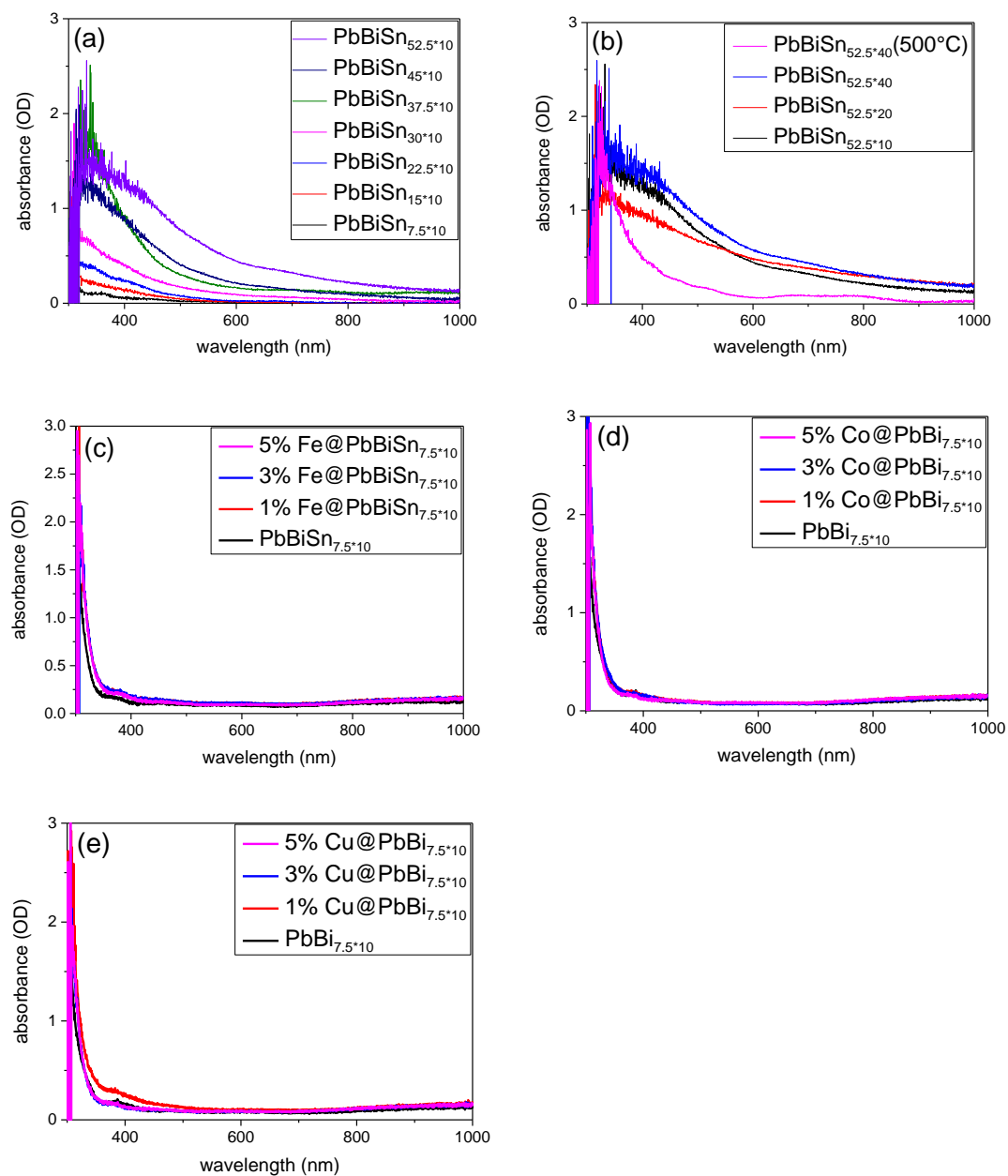
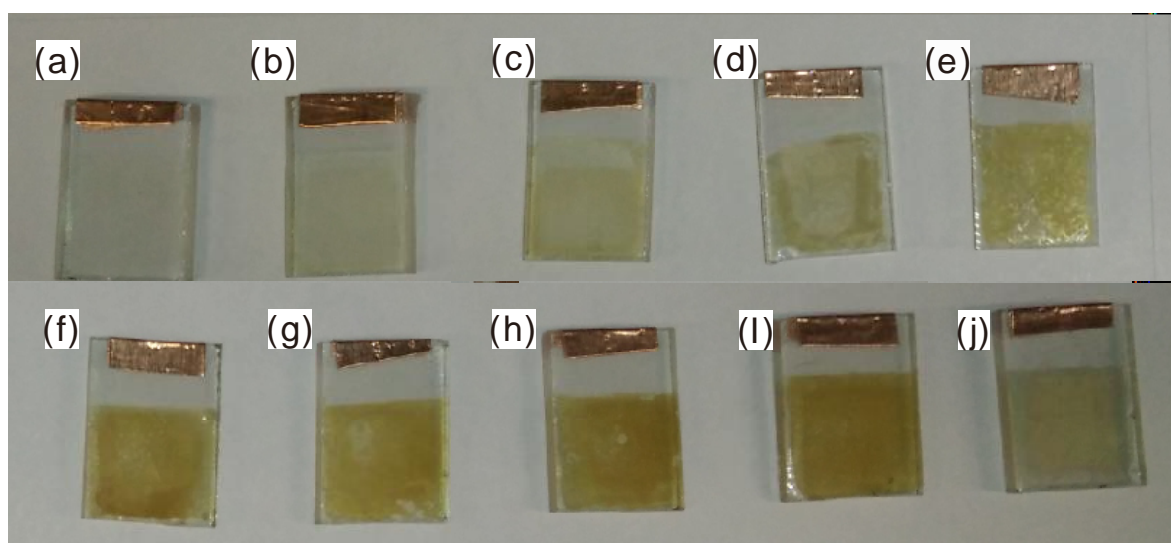


Figure 20 UV-vis absorption spectrum of a series of samples. (a) samples of different concentrations of precursor (b) samples with different volumes of precursor (c) samples doped with different amounts of amorphous iron oxide (d) samples doped with different amounts of amorphous cobalt oxide (e) samples doped with different amounts of amorphous copper oxide.

Figure 20(c) (d) and (e) shows the UV-vis absorption of $\text{PbBiSn}_{7.5*10}$ or $\text{PbBi}_{7.5*10}$ samples doped with amorphous iron, cobalt or copper oxide. Doping does not greatly improve absorbance, which indicates that the change of photo properties of doping samples is not owing to the change of light absorption. This will be discussed in the chapter on photoelectrochemistry experiment.

Figure 21 shows the photographs of samples with different precursors. Consistent with the results of UV-vis absorption measurement, the sample that was prepared using a higher concentration or greater volume of precursor appears darker. The dark colour shows most in samples with more PbO_2 as PbO_2 is not stable at high temperatures. It is likely that PbO_2 decomposed after heating to 500°C , and those samples became lighter in colour.



*Figure 21 Photographs of samples with change of colour. (a) $\text{PbBiSn}_{7.5*10}$, (b) PbBiSn_{15*10} , (c) $\text{PbBiSn}_{22.5*10}$, (d) PbBiSn_{30*10} , (e) $\text{PbBiSn}_{37.5*10}$, (f) PbBiSn_{45*10} , (g) $\text{PbBiSn}_{52.5*10}$, (h) $\text{PbBiSn}_{52.5*20}$, (i) $\text{PbBiSn}_{52.5*40}$ and (j) $\text{PbBiSn}_{52.5*40}$ heated at 500°C .*

2.3.4 Photoelectrochemistry

2.3.4.1 PbBiSn samples

Photoelectrochemistry (PEC) experiments on PbBiSnO_x samples were performed under a positive bias for oxidation of water (photoanode) in a three-necked flask. The whole cell includes an Ag/AgCl reference electrode and a platinum wire counter electrode. The electrolyte was 0.1M NaOH solution at pH=13, and a Xe lamp through a 420 nm band pass filter with an irradiance of 1 sun was used as the light source. All samples showed a photocurrent which can arise from the desired oxidation of water or oxidation of the electrode. Several series of samples were prepared and tested to study how various factors affected the photocurrent.

2.3.4.2 Effect of calcination temperature

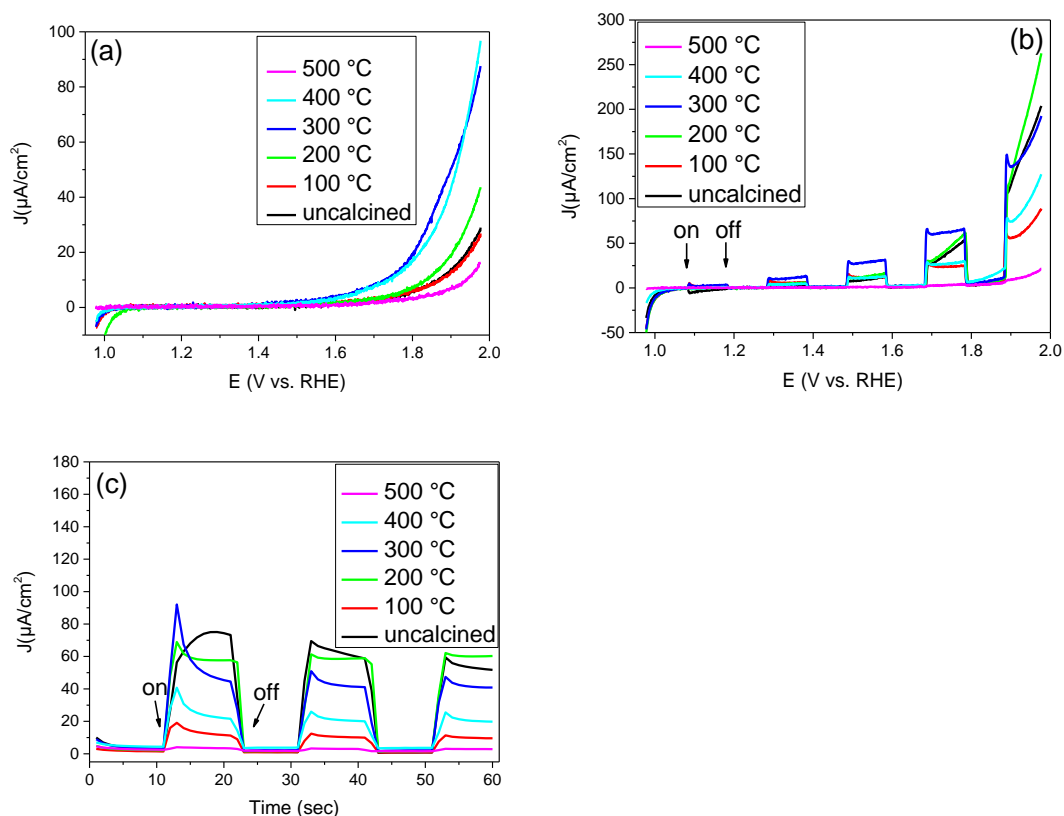


Figure 22 Photo electrochemistry on samples calcined under different temperatures ((a) LSV in the dark, where the large current after 1.6 V is due to water oxidation. (b) LSV-illuminated (on)-dark(off) and (c) CPE-photoresponse under bias of 1.78 V versus RHE). Samples were all prepared using 20 μ L 7.5% w/w PbBiSn precursor and heated at 100 $^{\circ}$ C.

Figure 22 shows the PEC results of samples heated at different temperatures. When heating was below 300 $^{\circ}$ C, the photocurrent increased as the temperature increased. The photocurrent attained its highest point around 300 $^{\circ}$ C to 400 $^{\circ}$ C, and significantly decreased when the heating temperature rose above 400 $^{\circ}$ C. Figure 22 (b) shows the photo response of these samples. The light was turned on and off during the LSV experiment to check the response time. All the samples show a very fast response, and it takes the photocurrent one second

to change in correspondence with the light. It was noticeable that when the light was turned on, the “300°C” sample could achieve higher potential than the “400°C” sample, even though they show almost the same spectrum in Figure 22 (a). The different crystallinity under different temperatures could be the reason. When examining the light response at the same bias potential, the samples’ performance revealed more details as shown in Figure 22 (c). The photocurrent lifted to a very high level at the moment the light turned on, and subsequently decreased. It is because of the accumulation of holes on the surface which may obstruct the carrier transfer¹³¹. Improvement of carrier mobility might be helpful to solve the transient anodic photocurrent peaks.

Heating affects the photocurrent and it was found that the optimum temperature is around 300°C. As different temperatures lead to different crystallinity, defect density is affected. For samples that were heated at low temperature, the low crystallinity structure has poor carrier mobility leading to low photocurrent and transient photocurrent peaks. On the other hand, where good crystallized samples were heated at high temperature, poor photocurrent is also generated due to the low defect density and low carrier density. In Figure 22, the “500°C” sample produced the lowest photocurrent. The main point for this variation is a balance of carrier mobility and number of defects. Amorphous materials have good defect density and low carrier mobility, which situation changes inversely as the calcining temperature increases.

2.3.4.3 Volume of precursor

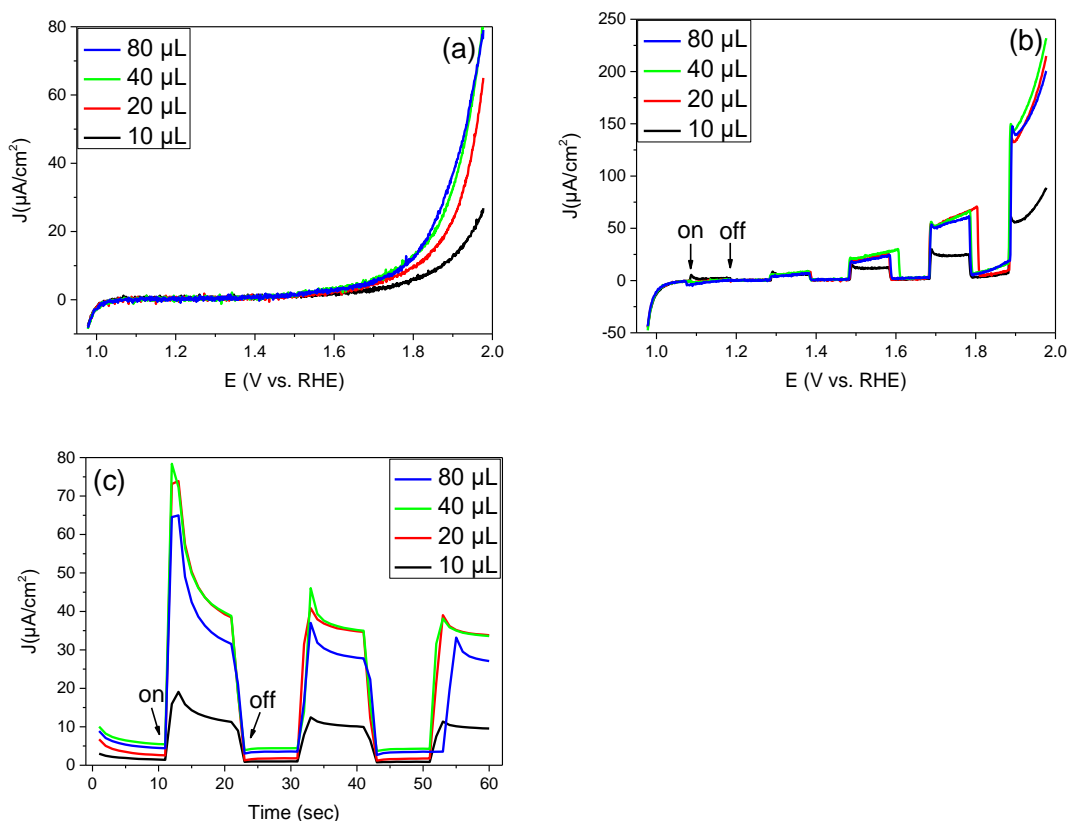


Figure 23 Photoelectrochemistry on samples prepared with different volumes of precursor ((a) LSV, (b) LSV-photo-dark and (c) CPE-photo-dark). Samples were all prepared using 7.5% w/w PbBiSn precursor and heated at 100°C.

Figure 23 shows the PEC results of samples prepared using different volumes of precursor. Ideally, the volume of the metal precursor would be directly proportional to the thickness of the film. However, some of the liquid precursor is lost during the spin-coating process. This may affect the final quantity of chemical on the glass, especially for samples using larger volumes of precursor. In fact, the photocurrent performance of “20 μL ”, “40 μL ” and “80 μL ” samples showed little difference (Figure 23 (b)). Nevertheless, Figure 23 (a) still proves that the sample using more precursor has a higher photocurrent. This series of samples also show fast light response, with the transient photocurrent peaks still occurring (Figure 23 (c)). In conclusion, the increase of photocurrent from

“10 μ L” to “20 μ L” sample is as large as expected, whereas there was little difference between samples “20 μ L”, “40 μ L” and “80 μ L” due to the loss of precursor during the preparation process.

2.3.4.4 Concentration of precursor

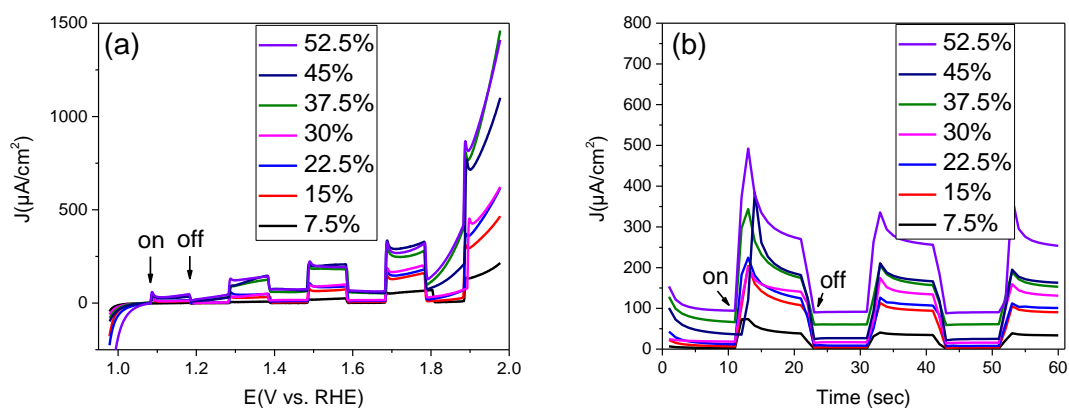


Figure 24 Photoelectrochemistry on samples prepared with different concentrations of precursor ((a) LSV-photo-dark and (b) CPE-photo-dark under bias of 1.78 V versus RHE). Samples were all prepared by 20 μ L PbBiSn precursor and heated at 100°C.

Since liquid precursor may be lost during the spin-coating process, an alternative method is to use a precursor with higher concentration. The increased viscosity of this precursor could decrease the loss during spin-coating. Figure 24 shows the PEC results of samples prepared using precursors of different concentrations. There is no doubt that the higher concentration precursors obtained samples with correspondingly higher photo current and dark current. The increased content was able to absorb more

photons and thus generate higher current, as shown in the UV-vis experiments (Figure 20 (a)). Note that the transient photocurrent peaks were obvious in Figure 24 (b).

Increased volume or concentration should result in thicker film. However, due to the losses during spin-coating, the thickness is not in a linear relationship with volume or concentration. The relationship between thickness and light absorption could be described as following the Beer-Lambert law:

$$A = K \cdot l \cdot c \quad \text{Eqn 6}$$

Where A is absorbance, K is coefficient, l is the thickness and c is concentration. Assuming that concentration of films is equal, the absorbance should be linear in relation to thickness. However, the thicker film does not always mean better photocurrent. As the thickness increases, it's more difficult for electrons and holes to transfer to the surface where reaction occurs. There will be a maximum photocurrent.

Figure 25 shows the relationship of concentration of precursor, absorbance and photocurrent. It shows that the increase rate of photocurrent slows as absorbance increases. The photocurrent is almost linear in relation to concentration of precursor which may be due to the samples being too small.

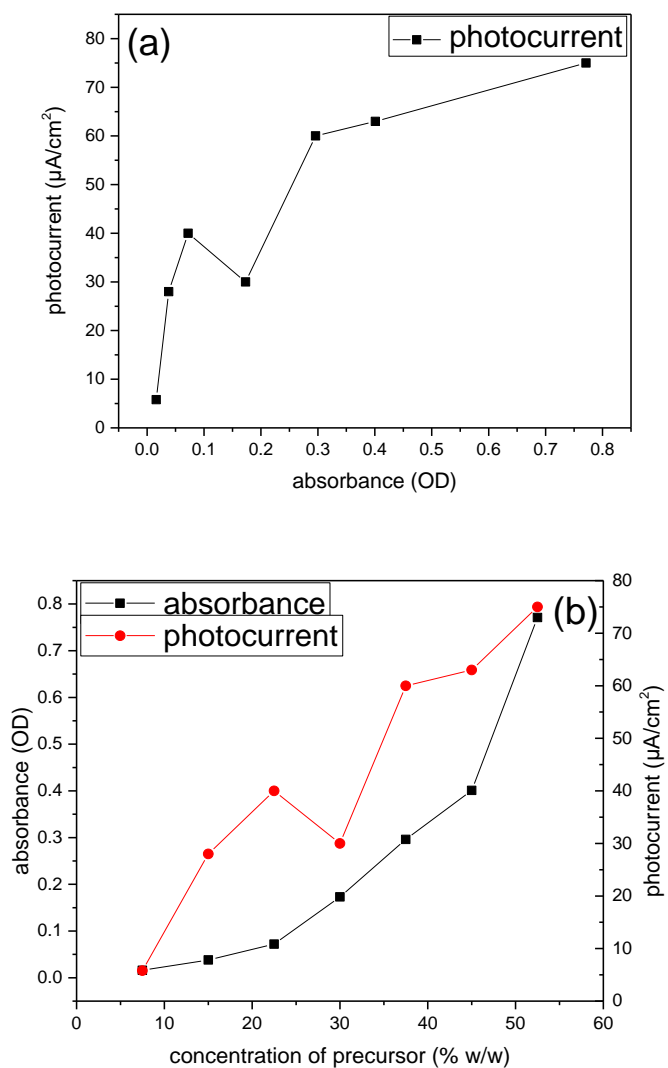


Figure 25 The relationship between (a) absorbance and photocurrent and (b) between concentration of precursor and absorbance or photocurrent. The data was collected from samples of $10 \mu\text{L}$ of different concentrations of PbBiSn precursor heated at 100°C . The photocurrent was collected at bias of 1.3 eV versus RHE. The absorbance data was collected at wavelength of 500 nm .

2.3.4.5 Stability

Stability of a photoelectrode is a very important factor and the photocurrent should not lose too much whether the experiment is repeated or over or long time period. Figure 26 shows the long-time photocurrent measurement for 300 seconds. The samples run in this experiment were PbBiSn 52.5% w/w precursor of different volumes, which were heated at 100°C for one hour. All the samples kept good stability, in fact the “20 μ L” sample retained 92% of photo current remained after 5 minutes. In the figure, the samples also show transient photocurrent peaks due to the poor efficiency of charge carriers at the surface. This indicates that addition of a cocatalyst to the surface of PbBiSnOx may be beneficial for improving steady state photocurrents.

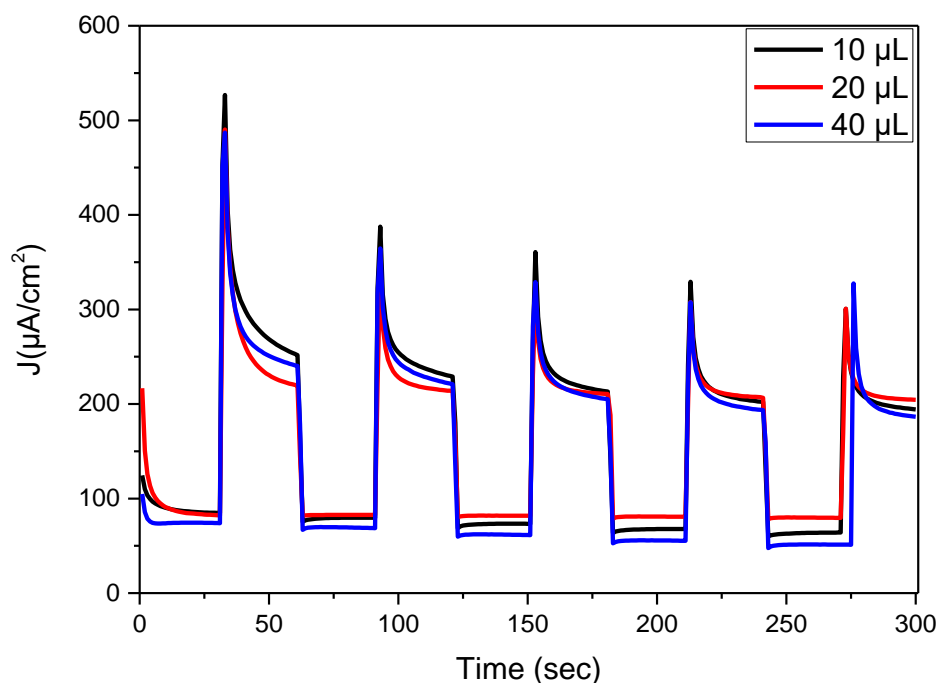


Figure 26 Stability test of samples with 52.5% w/w PbBiSn precursor.

2.3.4.6 Study of ratio of Pb-Bi-Sn in PbBiSnOx system

To optimize the metal ratio of PbBiSnOx, a series of samples were made and tested by photoelectrochemistry. The samples were prepared with 10 μL of 7.5 % w/w precursor with different metal ratios, as listed in Table 2. The results allow comparison and indicate the best metal phase.

Figure 27 is a three-phase overview of the relationship between the ratio of Pb-Bi-Sn and the photo current (= (current under visible light) – (dark current)) (Figure 27 (a)) and dark current (Figure 27 (b)) at condition of bias 800mV. Here the photo current is pure current induced by irradiation, which could accurately reveal the relationship between the photo-induced current and the metal ratio. As can be seen, the photo current is higher in the right-hand area in the three-phase figure and attains its highest value at $\text{Pb}_{1/2}\text{Bi}_{1/3}\text{Sn}_{1/6}$ 7.5*10.

The dark current figure did not show the same trend as the photo current figure. Three peak values are around $\text{Bi}_{1/4}\text{Sn}_{3/4}$ 7.5*10, $\text{Pb}_{1/2}\text{Bi}_{1/6}\text{Sn}_{1/3}$ 7.5*10 and $\text{Pb}_{3/4}\text{Bi}_{1/4}$ 7.5*10. This indicates that the best ratio for pristine electrochemistry property is not the same as that for photo properties. This research result is potentially beneficial for sample optimum.

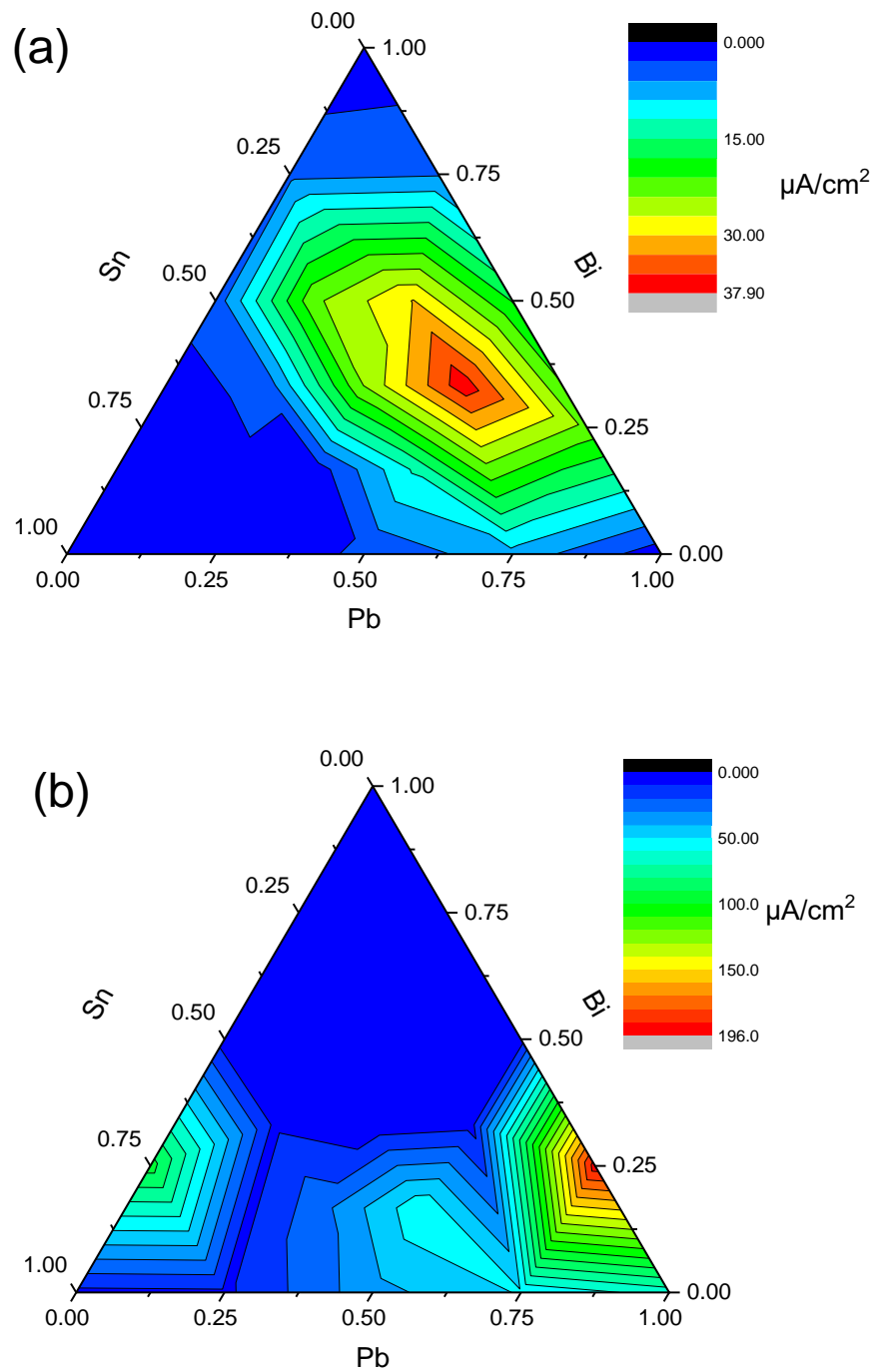
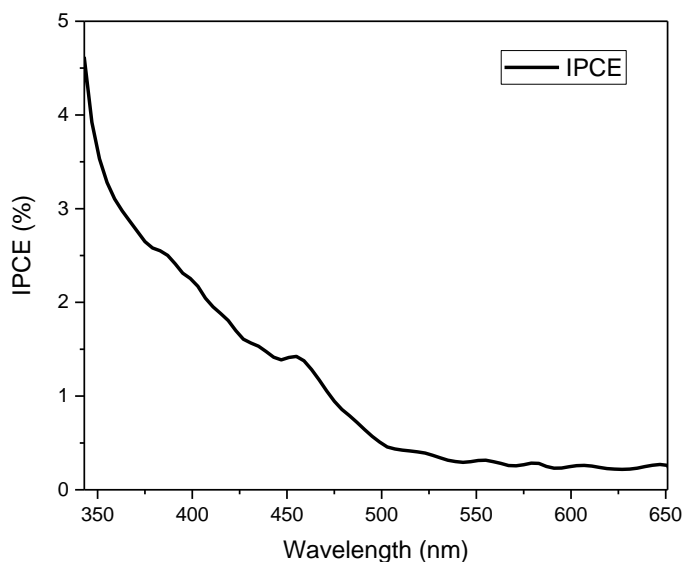


Figure 27 (a) Photo current (=current under visible light – current in dark) and (b) dark current of Pb-Bi-Sn oxide samples with different ratios.

2.3.4.7 Incident photon-to-current efficiency (IPCE) study



*Figure 28 Incident photon-to-current efficiency (IPCE) measured at 1.23V versus RHE. The test sample is $\text{PbBiSn}_{52.5*10}$.*

Better light absorption is not the sole condition for better photo current. Incident photon-to-current efficiency (IPCE) was carried out to determine which wavelengths of light are responsible for the photocurrent response and the results are shown in Figure 28. $\text{PbBiSn}_{52.5*10}$ was used due to the quality of its performance in photocurrent measurement.

The figure shows the conversion efficiency from photon absorption to current generation. The trend of conversion efficiency along the wavelength is in accordance with the absorption spectrum (Figure 20). The sample showed a sharp drop as the wavelength increased and showed higher conversion before 420 nm which is in UV range. High efficiency was also found in the range of visible light, between 420 nm and 500 nm (purple and blue light). According to

this absorption, the colour should be yellow which is consistent with the photograph (Figure 21). It proved that the Pb-Bi-Sn system samples have potential application as visible light active photoelectrode materials.

2.3.5 Modification of amorphous oxide films

In the aforementioned photoelectrochemistry experiments, all the Pb-Bi-Sn oxide samples showed photo response whilst the photocurrents showed transient anodic peaks due to poor carrier mobility. Modification experiments were performed in an attempt to improve light absorption and catalytic properties.

Amorphous Fe, Co and Cu oxide were doped in Pb-Bi-Sn system films. WO_3 nanoparticle was also added to the films for the purpose of increasing light absorption. Figure 29 shows the PEC results of these modified samples tested with bias potential of 800 mV vs Ag/AgCl. $\text{PbBiSn}_{7.5*10}$ doped with Fe retains photocurrent, the optimum amount being 3% w/w (Figure 29 (a)) which gave an increase of about 35 % to the photo current (from $24.4 \mu\text{A}/\text{cm}^2$ to $31.0 \mu\text{A}/\text{cm}^2$). However, the carrier mobility improved little due to the transient anodic current peaks. Further experiments showed that the improvement is affected by the Pb-Bi-Sn metal ratio. When the same Fe doping was applied in $\text{PbSn}_{7.5*10}$ (Figure 29 (b)) and $\text{PbBi}_{7.5*10}$ (Figure 29 (c)) samples, no improvements were shown. Moreover, the Fe doped $\text{PbSn}_{7.5*10}$ and $\text{PbBi}_{7.5*10}$ samples show no photo response and the photo currents are almost zero. Furthermore the photoresponse disappeared in Cu or Co doped $\text{PbBi}_{7.5*10}$ (Figure 29 (d) and (e)) samples. None of these doped samples showed significantly increased

photocurrent compared to the undoped samples. Nevertheless, these doped samples showed greatly enhanced dark current. This was especially noticeable in Fe doped $\text{PbSn}_{7.5 \times 10}$ (Figure 29 (b)), Fe doped $\text{PbBi}_{7.5 \times 10}$ (Figure 29 (c)) and Co doped $\text{PbBi}_{7.5 \times 10}$ (Figure 29 (e)), where the dark current could increase up to 5, 24.5 and 244.3 times compared to undoped samples.

Adding of WO_3 (Figure 29 (f)) could to some extent improve the photo current, while the dark current was not enhanced as much by this method as with Fe, Co or Cu doping. The right amount of WO_3 (2.5% w/w) could increase photo current by about 63 % (from $31.63 \mu\text{A}/\text{cm}^2$ to $19.39 \mu\text{A}/\text{cm}^2$) of $\text{PbBiSn}_{7.5 \times 10}$. It is noticeable that too much WO_3 had the opposite effect. When adding 10 % w/w of WO_3 , the photocurrent is only half that of the undoped sample.

Previous results show that the UV-vis absorption did not appear better than light absorption in doped samples (Figure 20) which means the dopant could not help the films to absorb more photons. The resulting decrease of photo current in some doped samples was probably because the dopant acted as a recombination centre. The photogenerated electrons and holes quickly recombined at these centres before they reached the reaction site on the surface. It therefore appears that the reason the addition of transition metal colour centres does not lead to any increase in photocurrent is because the optical transitions remain localised and, in heavily doped samples, act as recombination sites.

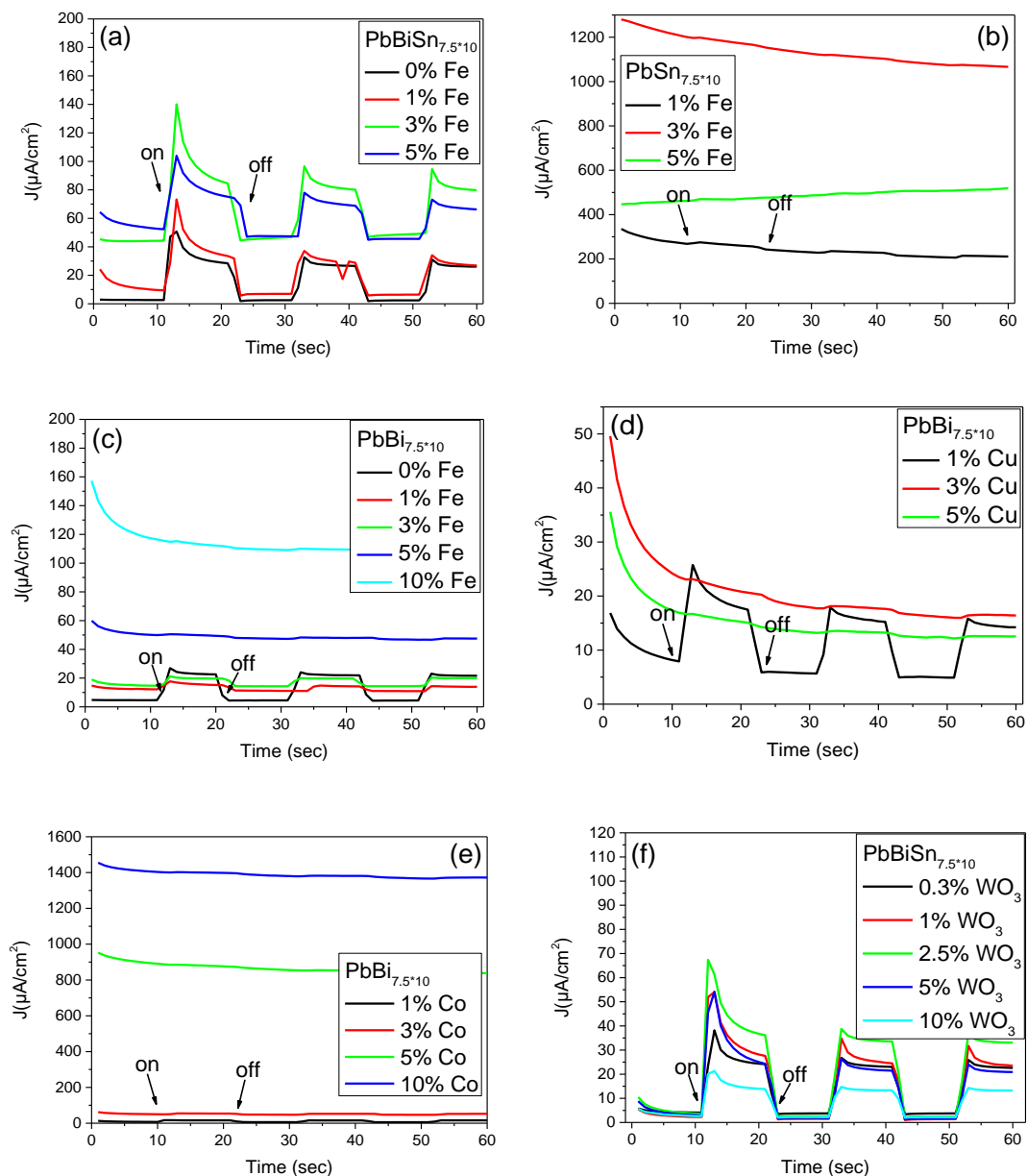


Figure 29 Adding different metals into Pb-Bi-Sn system. CPE of (a) $PbBiSn_{7.5*10}$ with Fe_2O_3 , (b) $PbSn_{7.5*10}$ with Fe_2O_3 , (c) $PbBi_{7.5*10}$ with Fe_2O_3 , (d) $PbBi_{7.5*10}$ with CuO , (e) $PbBi_{7.5*10}$ with Co_2O_3 and (f) $PbBiSn_{7.5*10}$ with WO_3 . The bias is 1.78 V versus RHE. The percentages are mass fractions (w/w).

Cobalt oxide has been widely used to improve photoelectrodes^{34, 107, 132, 133}. Here, Co-Pi (the common designation of CoO_x deposited in the presence of

phosphate electrolyte) was electrodeposited on $\text{PbBiSn}_{7.5*10}$ amorphous metal oxide photoelectrode as shown in Figure 30. In comparison with the undoped sample, the electrodeposition of Co-Pi increases the dark current but decreases the photo current. After deposition of Co-Pi, the photo current decreased from $31.0 \mu\text{A}/\text{cm}^2$ to $7.7 \mu\text{A}/\text{cm}^2$ under bias potential of 800 mV, while the dark current increased from $15.5 \mu\text{A}/\text{cm}^2$ to $218.8 \mu\text{A}/\text{cm}^2$. In literature⁸⁶, Co-Pi has been used to lower the onset potential and enhance the photocurrent of Fe_2O_3 because the Co-Pi deposition allows efficient photon absorption and hole transfer from hematite to Co-Pi. In our experiment, due to the amorphous structure the poor carrier mobility is more serious in the film but less so on the surface. The Co-Pi co-catalyst improved the efficiency of charge transport, but blocked the light from reaching the metal absorption centre.

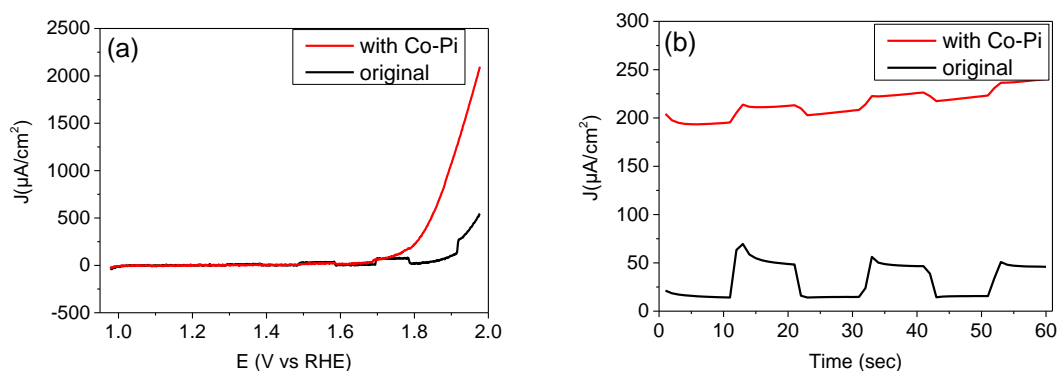


Figure 30 (a) LSV and (b) CPE test of $\text{PbBiSn}_{7.5*40}$. The CPE test was run under a bias potential of 800mV.

2.3.6 Layer by layer structures

Layer-by-layer structures were prepared in an attempt to improve hole-electron pair separation. First, a single layer was prepared on FTO glass, then after UV irradiation and 100°C heating, a second layer was prepared on the sample using the same method. Separate metal oxide layer-by-layer samples were finally prepared and tested, and the results are shown in Figure 31.

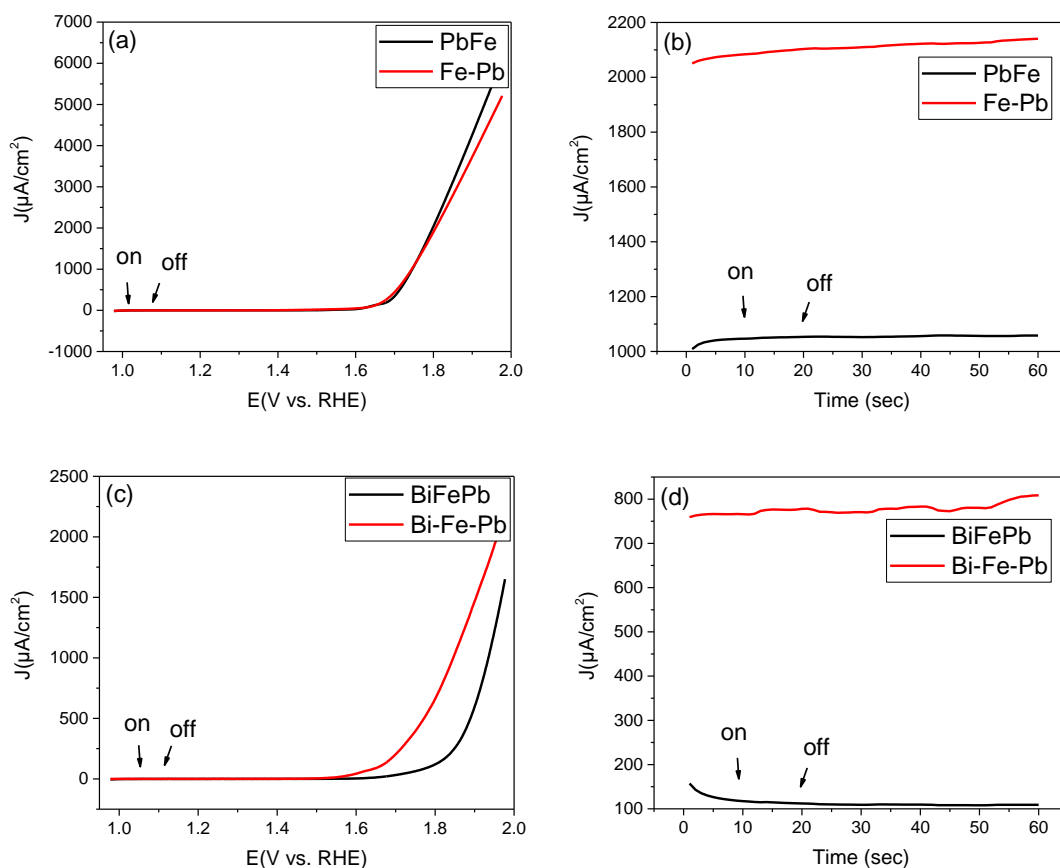


Figure 31 Comparison of mixed metal oxide film (black line) and layer-by-layer film (red line). (a) LSV and (b) CPE test of Pb/Fe sample and (c) LSV and (d) CPE test of Bi/Pb/Fe sample. The CPE tests were all running with a bias of 1.78 V versus RHE.

These layer-by-layer samples did not improve photo response, and the photocurrent is almost zero. The Fe-Pb sample increased the dark current little more than the mixed PbFe metal oxide film sample in the LSV result. But for Bi-

Pb-Fe sample, it has lower onset potential and a better electrochemistry performance compared to the mixed metal oxide film sample.

The energy band gap of the three-metal oxide in the Bi-Pb-Fe sample is overlapped, which could improve the photon absorption. Electron and hole separation could be enhanced due to the layer-by-layer structure so that the electrochemistry property is improved.

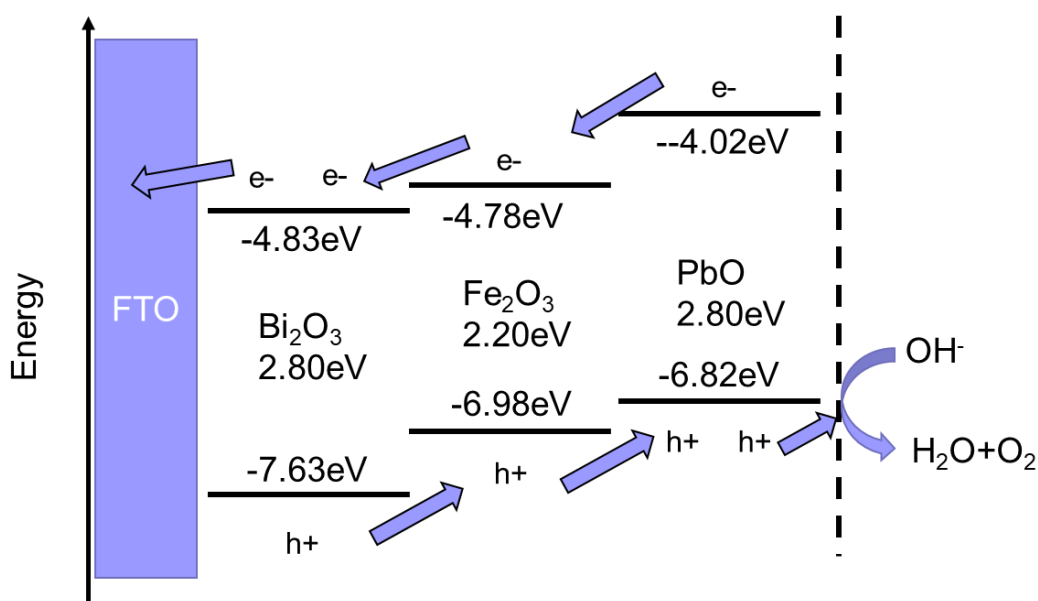


Figure 32 Energy band structure of Pb-Fe-Bi layer-by-layer film.

2.4 Conclusion

In this chapter, Pb-Bi-Sn oxide amorphous films were prepared on FTO glass as photo electrodes. Amorphous Pb-Bi-SnO_x films showed visible light response. The main valence state in the used film was Pb₃O₄, PbO₂, Bi₂O₃ and SnO indicating reduction of the films. The Pb, Bi and Sn cations improved carrier mobility. Calcining temperature affects the photoresponse, the optimum

being 200°C to 300°C presumably due to a combination of carrier density and carrier mobility. Volume and concentration of precursor used in spin-coating could improve photocurrent and the darker films deposited on substrate showed better absorption photons. Lead mainly existed as Pb_3O_4 and PbO_2 in the film and acted as a light absorber. Bi and Sn cations play key roles in improving carrier mobility. The Pb-Bi-Sn system overcomes the problem of amorphous metal oxide to perform photo response, and could therefore be used for oxygen evolution.

Many modification methods were used to try to improve the photo properties, including changing the ratio of Pb-Bi-Sn, and adding amorphous Fe_2O_3 , Co_2O_3 , CuO and nanoparticle WO_3 . Layer-by-layer structures were also prepared and tested for possible improvement. The PEC experiments show that the doping of Fe, Co and Cu could improve dark current as much as several hundred times compared to undoped samples. The right amount of WO_3 nanoparticle could improve photo current. A sample with 2.5 % w/w WO_3 nanoparticle showed photo current that was 63 % higher than that of undoped $\text{PbBiSn}_{7.5*10}$.

PEC experiments were performed to test the photoelectrochemistry properties. An IPCE experiment was carried out to demonstrate the wavelength-dependent photo response of Pb-Bi-Sn.

Although the photo current of these samples was not as high as many good crystalline photoelectrochemical materials, these amorphous films still have unique advantages and a potential application. The results show PbBiSn metal oxide films could be visible light active materials if surface catalysis could be improved and film thickness optimised.

Chapter 3

Surface Modification of Fe_2O_3
Anode for Photoelectrochemical
Water Oxidation

3 Surface Modification of Fe₂O₃ Anode for Photoelectrochemical Water Oxidation

3.1 Introduction

In chapter 2, amorphous metal oxide photoelectrodes were prepared and tested, and several methods were attempted for better photo properties. However, the most popular material for semiconductors is still crystalline.

α -Fe₂O₃ (hematite) is widely used as a photoanode material due to its abundance on earth, its nontoxicity, low cost and stability in aqueous electrolyte. The band gap of hematite is about 2.0 eV to 2.2 eV which allows absorption in visible light range. As a photo active material, hematite has some drawbacks, such as high electron-hole pair recombination rate, short hole-diffusion length ($\sim 2\text{--}4$ nm) and low carrier mobility ($\sim 10^{-1}$ cm² V⁻¹ s⁻¹)⁸⁶. All these deficiencies lead to a low conversion efficiency. Hematite also has a low rate of oxygen generation.

Hematite film photoelectrodes were prepared for oxygen evolution. To solve the previously mentioned deficiencies and improve the photo properties, examination was made of much previous research. Alexander Müller and his co-workers¹³⁴ prepared dual absorber Fe₂O₃/WO₃ host-guest architectures for PEC applications. The mesoporous Fe₂O₃ films were surface treated with WO₃ and this structure improved charge generation and transfer. Monica Barroso *et al.*⁵⁴ used CoO_x and Ga₂O₃ overlayers to surface-modify α -Fe₂O₃ photoanodes. Both CoO_x and Ga₂O₃ treatments induced a reduction of electron density in the hematite, reduced electron/hole recombination and increased the yield of long-

lived holes at the electrode surface. The presence of high densities of surface states is the primary problem which needs to be solved in order to enhance the photo properties.

As the main problem of hematite film is the surface defects which act as a recombination centre, many studies focused on the reduction of surface defects and surface modification¹³⁵⁻¹³⁷. The solution in most of these works is to overlay the surface of hematite by another layer of material. The improvement is not only effected by changes to the surface defects, but also by means of other factors, such as heterojunction formation or introduction of a co-catalyst.

3.2 Chapter aim

In this chapter, the main aim is to improve the photo property of a Fe_2O_3 film electrode by surface modification. The surface state could act as recombination centre and trap holes generated in the valence band and electrons generated in the conduction band. By decreasing the surface state, carrier mobility could be improved, recombination rate could be lower, and the photo current would be enhanced.

The following aims need to therefore be achieved:

- Develop simple and consistent experimental conditions. To make the experiments repeatable, several factors are required:
 - ⇒ The FTO glass should be fresh and cleaned by defined processes.

- ⇒ The metal salts should be operated on in a glove box to avoid the effects of water and oxygen.
 - ⇒ FTO glass to be covered by Teflon tape leaving only a 1 cm * 1 cm square window.
 - ⇒ FeCl₃ solution should be used in a Teflon container and measured to ensure it is the same in every autoclave.
 - ⇒ Dipping time and dipping area should be restricted.
 - ⇒ Irradiation position and light power to be measured every time to ensure consistency.
-
- Investigate the effect of different concentrations of the precursor.
 - Compare the metal ion surface-modified sample to the pure Fe₂O₃ sample.
 - Quantify and qualitatively analyze the samples through different characterization experiment results.
 - Analyse the EIS and Mott-Schottky data. Understand the mechanism of enhancement by surface modification.

3.3 Results and discussion

3.3.1 Synthesis of Fe₂O₃ film electrode

FTO glass (Sigma-Aldrich, L * W * D 300 mm * 300 mm * 2 mm) was cut into 30mm*10mm size slides as conductive substrate. After that, the small FTO slides were cleaned in ethanol, acetone and water using an ultrasonic cleaning machine and dried under nitrogen flow. To prepare Fe₂O₃ films in the same size for successive experiments, Teflon tape was used to partially cover the FTO substrate. As shown in Figure 33, the FTO slide is covered leaving only a 10mm*10mm window on the conductive side (Figure 33 (a) and (b)).

The FTO slide was placed in an autoclave with 14mL 0.15M FeCl₃ aqueous solution for a hydrothermal experiment which ran at 100°C for 6 hours. After natural cooling to room temperature, the grown slide was cleaned gently using Millipore water and dried under nitrogen flow. At this step, the slide looked yellowish, which was probably FeOOH¹³⁸. In the following calcination at 500°C for 2 hours and 800°C for 30 minutes, the slide reacted as per the following equation and thus the iron oxide slide was obtained.



On the obtained Fe₂O₃ slide, the Fe₂O₃ film only covered a small square area due to the coverage of Teflon tape, as shown in Figure 33 (d). When performing the PEC experiments, the bottom side of slide was covered again to avoid the contact of electrolyte (Figure 33 (c)).

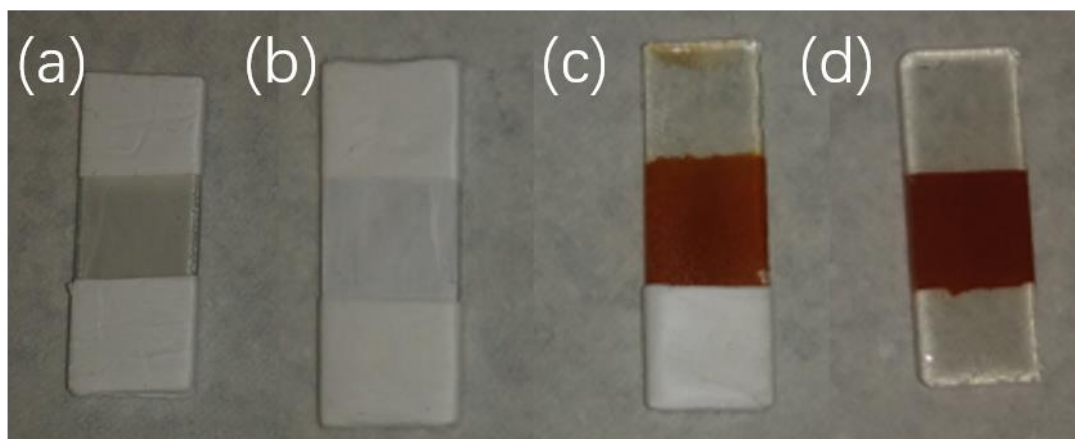


Figure 33 (a) Top view and (b) back view of FTO slide before hydrothermal experiment. Final sample (c) with Teflon tape (for PEC/EIS experiments) and (d) without Teflon tape.

3.3.2 Surface-modified iron oxide electrode with metal ions

The chemical used in this experiment is bis(trifluoromethane)sulfonimide metal salt ($M(\text{TFSI})_x$, $M=\text{Li, Na, K, Mg, Zn}$), which easily decomposes to metal oxide and has been used to deposit metal oxide on electrodes¹³⁹. In this chapter, the $M(\text{TFSI})_x$ salt was first dissolved in acetonitrile to form 5mM solution. The iron oxide slide was dipped into this precursor solution for 30 seconds and then dried under nitrogen flow. After 1-hour calcination at 450°C, the metal-modified iron oxide electrode was prepared. 450°C is enough for the decomposition of TFSI organic group, whilst the temperature is not so high that the metal ions move deeper in to the in Fe_2O_3 film and instead remain on the surface. Due to the very low quantity of metal on the surface, the colour of the electrodes changed little after surface modification, which could be proved in the following UV-vis absorption measurement in section 3.3.3.3.

3.3.3 Characterization

3.3.3.1 X-ray diffraction (XRD)

X-ray diffraction (XRD) was performed to study the structure of samples and the results are shown in Figure 34. For all samples shown in the XRD patterns, all peaks are referred to FTO and Fe_2O_3 and can be found in the PDF card. The samples represent good crystal structures of FTO and Fe_2O_3 and no peaks arise from other modified metals or metal oxides. This revealed that only trace amounts of modified metal ions remained on the surface of the Fe_2O_3 layer. Comparing the XRD patterns of pure Fe and the modified samples, the peaks of Fe_2O_3 are almost the same in each. This indicates that the surface modification make no obvious change to the Fe_2O_3 structure. It seems likely that the additional metal ions do not agglomerate..

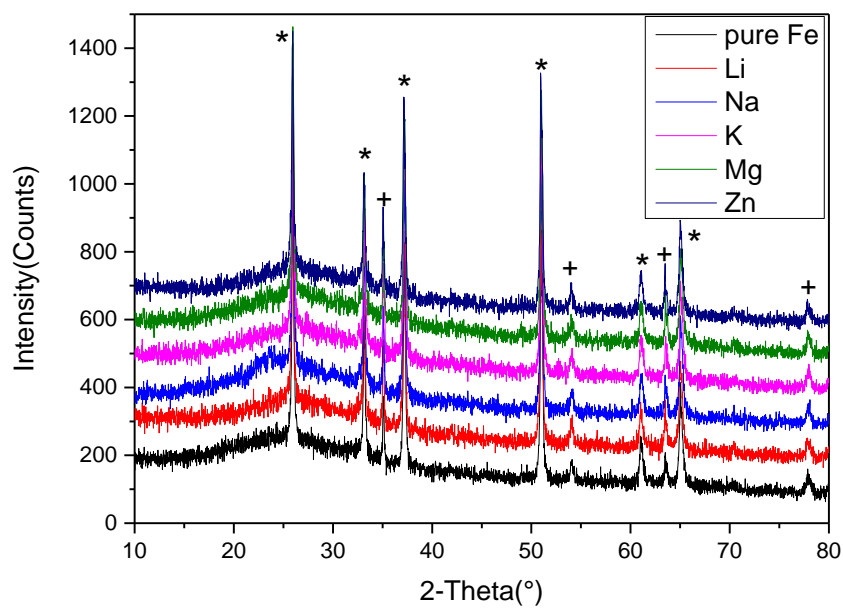


Figure 34 XRD figure of unmodified Fe and Li, Na, K, Mg and Zn modified samples. The peaks of FTO (PDF 46-1088) and Fe₂O₃ (PDF 33-0664) are marked using asterisk () and plus (+) respectively.*

3.3.3.2 Scanning electron microscopy (SEM) and Energy-dispersive X-ray spectroscopy (EDX)

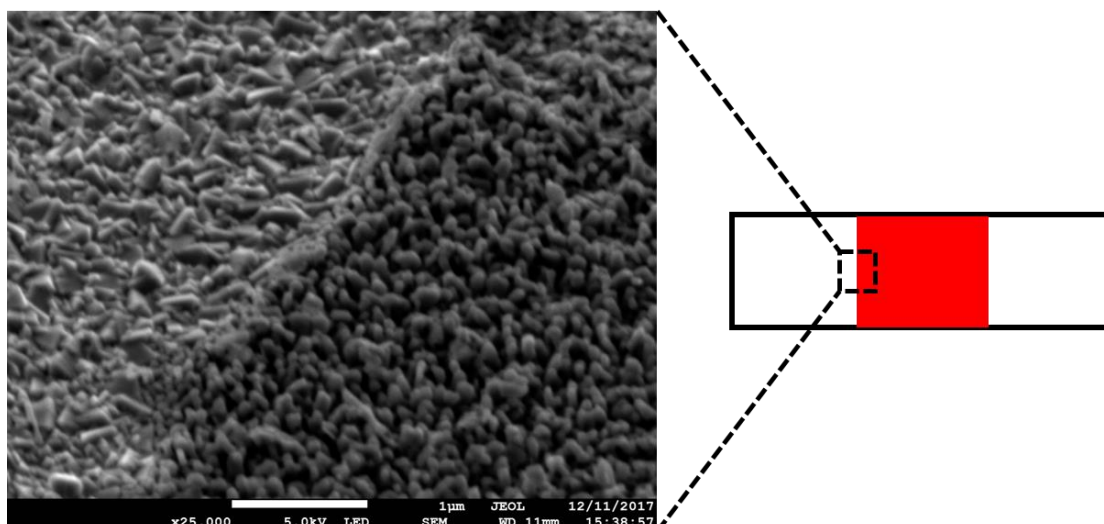


Figure 35 SEM image of FTO surface and Fe₂O₃ layer surface. The image was captured at the boundary of the Fe₂O₃ covered area. The left part in the image is lower level FTO particles and the right part is higher level Fe₂O₃ nanorods.

Scanning electron microscopy (SEM) was performed for detail of the surface morphology of the samples. The SEM image in Figure 35 was obtained at the edge area of the Fe₂O₃ square film, and the different morphologies in the image are from the FTO surface on the left side and the Fe₂O₃ surface on the right side. The FTO surface was composed of F-doped SnO₂ particles and the Fe₂O₃ part was vertical self-assembled nanorods. More surface SEM images are compared in Figure 36. Both unmodified and modified samples show a flat and homogenous Fe₂O₃ layer.

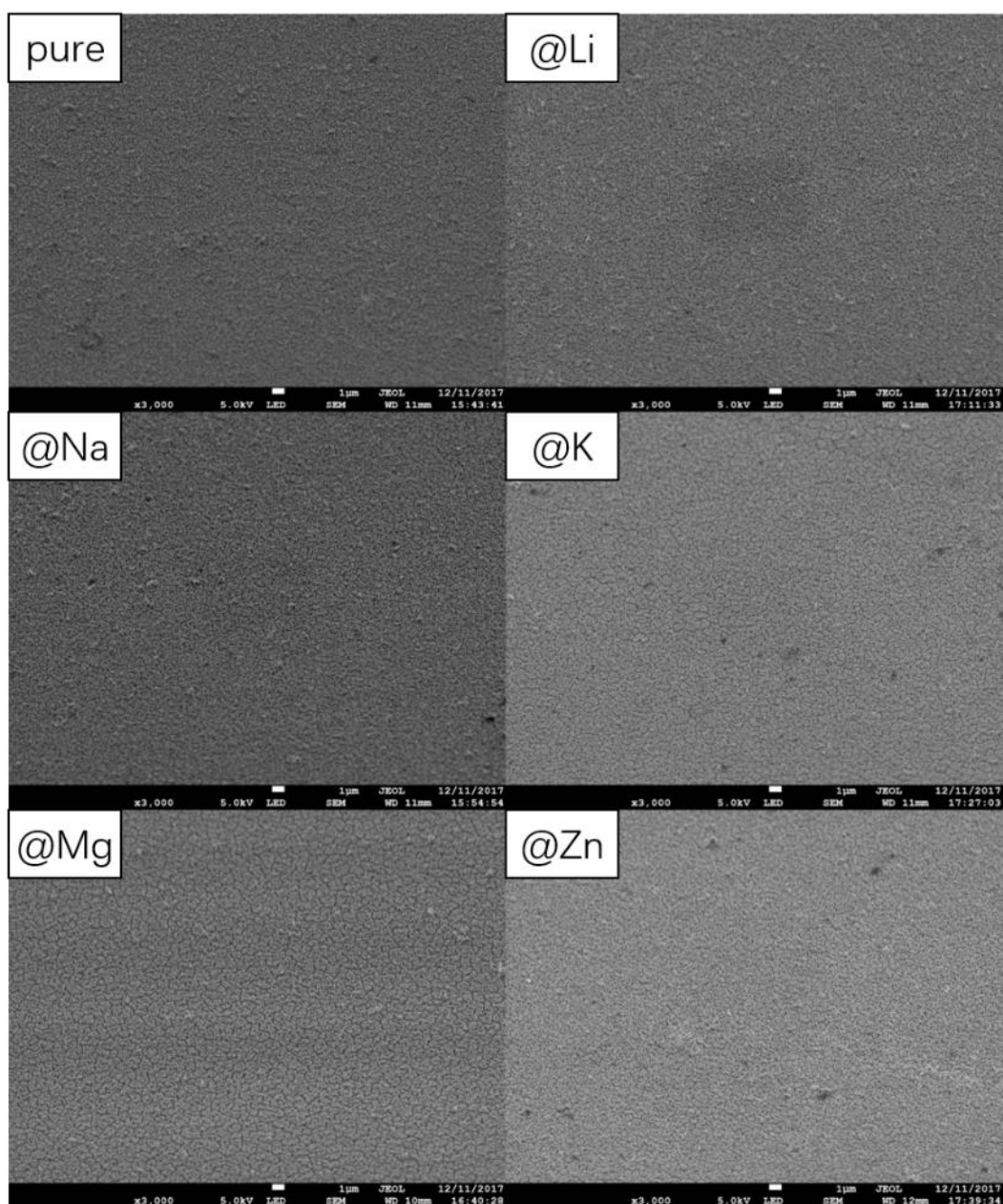


Figure 36 Low magnification SEM images of the surface of pure Fe and Li, Na, K, Mg and Zn modified samples. All the images are obtained at the same magnification.

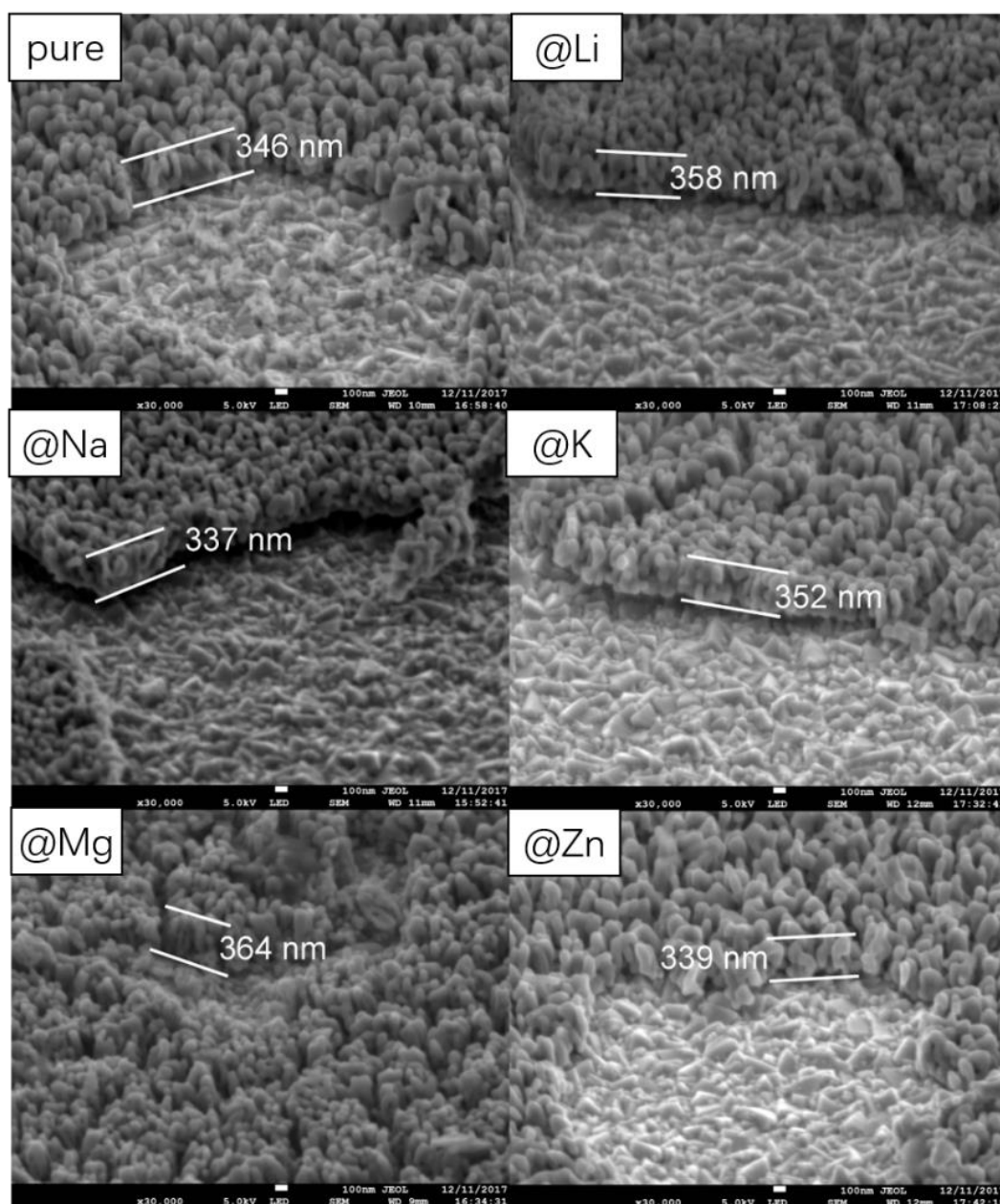


Figure 37 The SEM images of cracked surface area of unmodified and modified samples. The thicknesses are marked in every image.

Figure 37 shows images of the cracked area on the surface of these samples. In this way, the thickness of the Fe_2O_3 layer could be measured and compared. As shown in the figure, the thickness of the Fe_2O_3 layer of unmodified and Li, Na, K, Mg and Zn modified samples are 346 nm, 358 nm, 337 nm, 352 nm, 364 nm and 339 nm, respectively, and the thicknesses are almost the same. In fact,

by collecting thickness data at several different positions on every sample, it became evident that the Fe_2O_3 layer on all the samples, modified and unmodified, is around 350 nm (± 15 nm). This consistency in thickness was owing to the strict control of synthesis parameters during the preparation. Some uncontrollable conditions during the hydrothermal process, however, may still lead to slight differences in thickness.

3.3.3.3 UV-visible light absorption

Light absorption is important for photoelectrodes, especially the absorption in visible light range. The UV-visible absorption spectrum was collected before dip-coating, after dip-coating and after the PEC/EIS experiments, and is shown in Figure 38. A bandgap of 2.07 eV at the absorption edge of wavelength 600 nm was found for all data. The comparisons show that every modified sample has a decrease in absorption after dip-coating. The probable reason is that the modified metal oxide has slightly changed the surface defect which acts as an active centre. The opposite change occurred in the unmodified sample which performed an increased absorption after dip-coating. In addition, all samples improved the absorption after PEC/EIS because the samples were activated during these experiments.

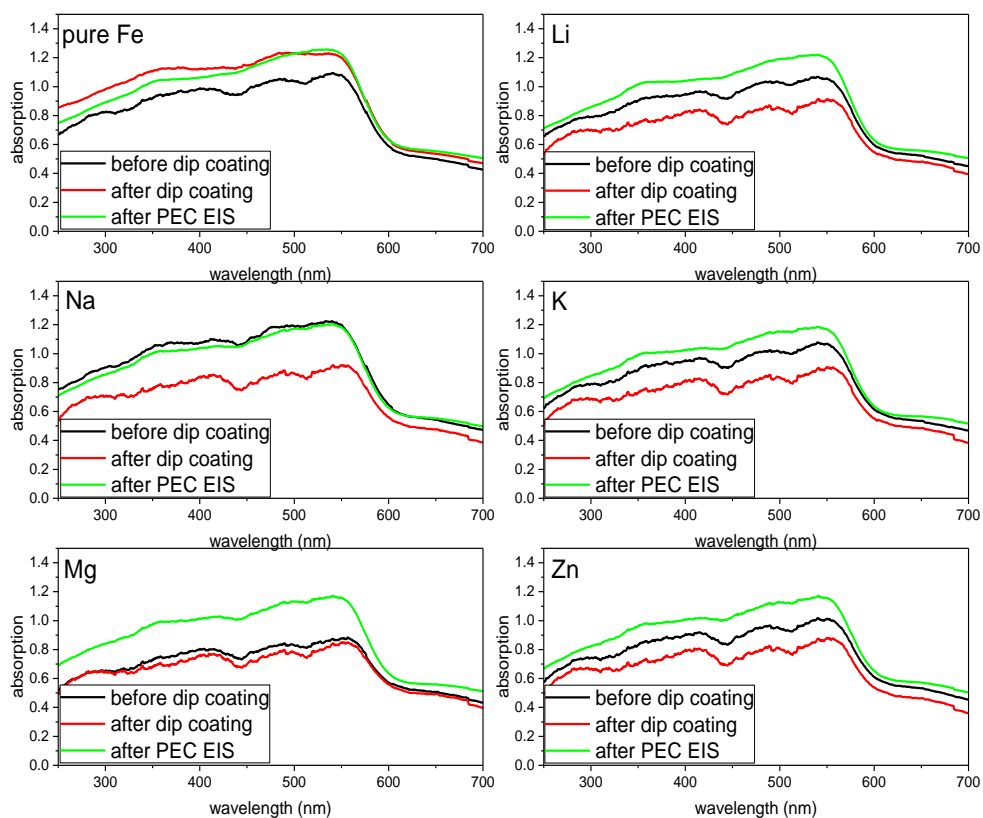


Figure 38 UV-visible absorption spectrum of unmodified and modified samples. The data was collected before dip-coating (black), after dip-coating (red) and after PEC/EIS experiments (green), respectively.

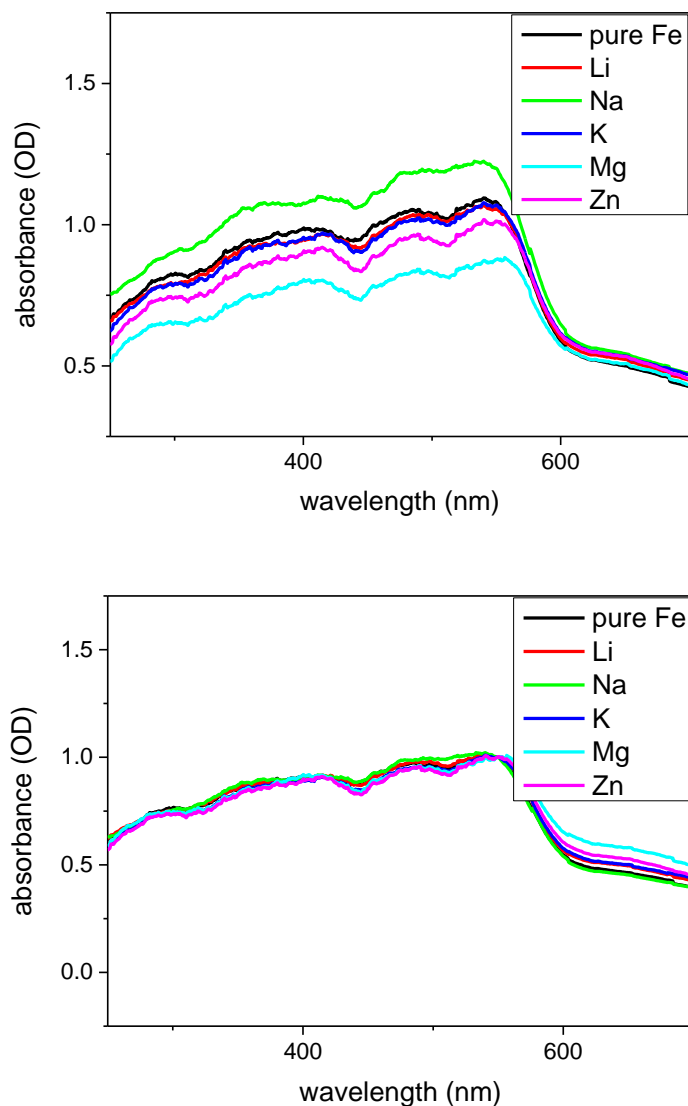


Figure 39 (a) Original and (b) normalized UV-visible absorption spectrum of unmodified Fe and Li, Na, K, Mg and Zn modified electrode samples.

Figure 39 (a) compares the UV-vis results of samples before dip-coating which represents the behaviour of pure Fe_2O_3 layer substrate. The values of the absorbance are different whereas the shapes of the spectrum are almost the same. This indicates that the light absorption of the substrates was probably affected by the surface appearance. The calcination temperature (800 C) is quite high so that the glass substrate would slightly melt. As a result, the surface of the slide would be wrinkled and affect the reflection and absorption of light,

and would further affect the photo current in PEC experiments. We used the normalization method to reduce the effect and set the base at same level (Figure 39 (b)). By this normalization, the main absorption range (before 600 nm) was consistent. Same normalization will be employed for the photo current experiments.

3.3.3.4 X-ray photoelectron spectroscopy (XPS)

This surface modification experiment only addresses the structure and composition of the surface layer, and does not affect any deeper layers. XRD and EDX were not suitable for surface measurement due to low resolution and accuracy. To obtain the surface sample details, fresh samples (unmodified and Li, Na, K, Mg and Zn modified electrode samples) were further characterized by X-ray photoelectron spectroscopy (XPS). A used Zn modified sample was also measured for comparison.

The high-resolution Fe 2p spectrum (Figure 40 (a)) shows the position of Fe 2p_{3/2} and Fe 2p_{1/2} at approximately 710.8 eV and 724.2 eV, respectively, and two satellite peaks with binding energies about 7 eV higher than the corresponding Fe 2p peaks. The fresh samples showed no obvious differences, whereas the used Zn modified sample showed a negative shift of about 0.9 eV. This shift reveals that the surface layer has been greatly changed during the PEC experiment. Moreover, the used sample showed weaker intensity in the higher binding energy area compared to fresh samples. Further analysis showed that the used Zn modified sample has relatively stronger Na peaks (Figure 41). These results indicate that NaOH from the electrolyte may deposit

and be physically adsorbed at the surface of the sample, therefore the XPS spectrum of the used sample shows weaker Fe_2O_3 peaks and stronger Na peaks. The NaOH deposition did not affect the PEC performance.

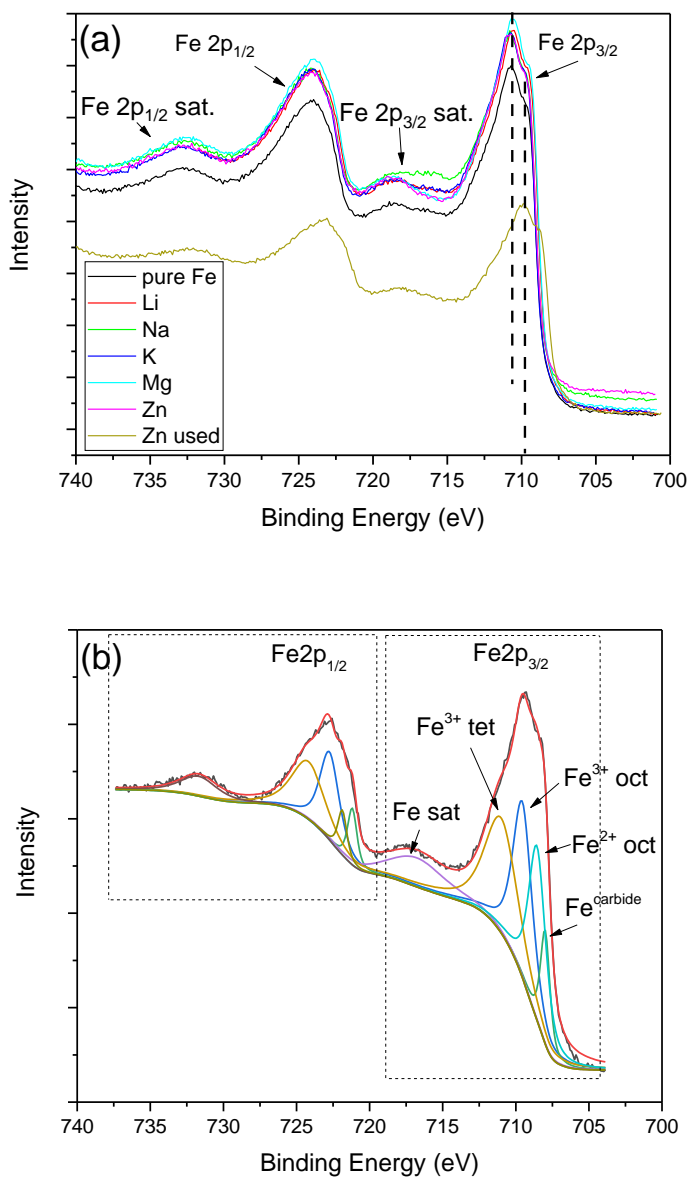


Figure 40 (a) XPS spectrum for Fe 2p. (fresh unmodified and Li, Na, K, Mg, Zn modified samples and used Zn modified sample) (b) Split XPS spectrum of fresh unmodified sample.

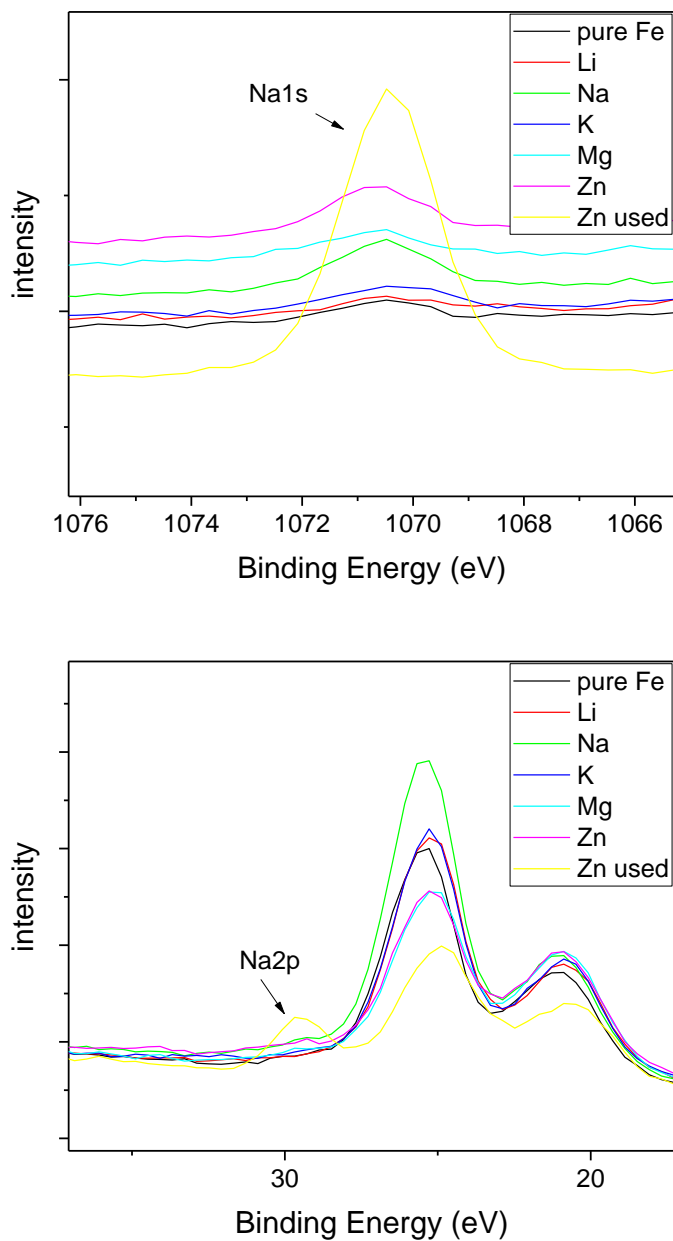


Figure 41 Relatively higher intensity Na peaks of used Zn modified sample.

The Fe 2p peak is convoluted and overlaid by several different iron species. According to the literature¹⁴⁰, a Fe 2p peak of fresh unmodified sample comprises several component signals as shown in Figure 40 (b) and Table 4. Typically, standard α -Fe₂O₃ comprises only octahedral Fe structure; and in Fe₃O₄, the Fe²⁺ occupy half of the octahedral sites and the Fe³⁺ occupy the

remaining octahedral and tetrahedral sites. Here the Fe 2p peak is split into different valence and geometry structures which can be explained by the surface effect. Due to the surface boundary effect, the surface structure is not complete and a higher density of defects are induced. This can be proved by etching XPS measurement shown in Figure 42(a). After etching of 180 seconds, the Fe 2p peak of internal Fe₂O₃ is symmetric which indicates that the Fe only comprises one state. This change could also be found in the comparison of O 1s (Figure 42(b)).

Table 4 Deconvolution parameters of the Fe 2p peaks measured for the fresh unmodified Fe₂O₃ sample. (oct, octahedral; tet, tetrahedral; sat, satellite)

Peak name	Position (eV)	FWHM (eV)	Line shape (G:L, %)	Area
Fe ^{carbide}	707.99	0.77	60:40	19042.16
Fe ²⁺ oct	708.54	1.39	60:40	35136.5
Fe ³⁺ oct	709.54	1.58	60:40	60394.27
Fe ³⁺ tet	710.99	2.65	60:40	66246.39
Fe sat	716.8	4.67	60:40	19757.53

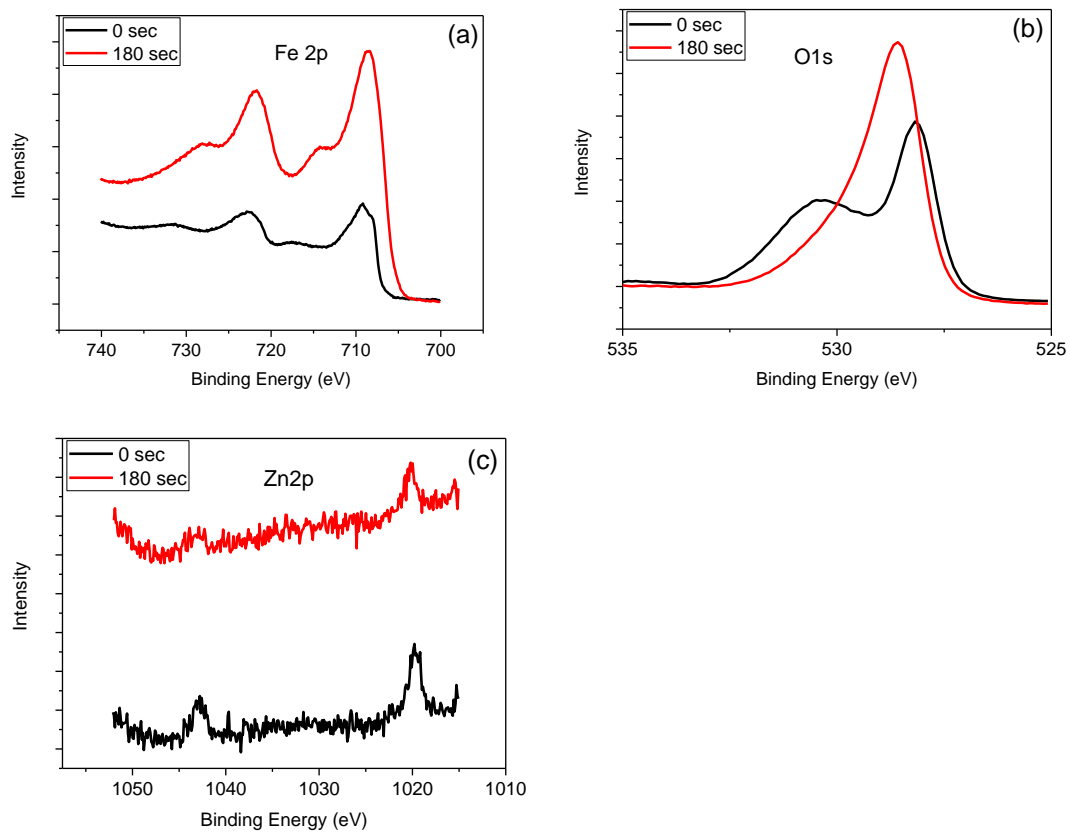


Figure 42 Etching XPS measurement of used Zn modified sample for (a) Fe 2p, (b) O 1s and (c) Zn 2p peak.

On the other hand, etching XPS measurement (Figure 42(c)) shows that the Zn²⁺ ion density is much lower internally than on the surface.

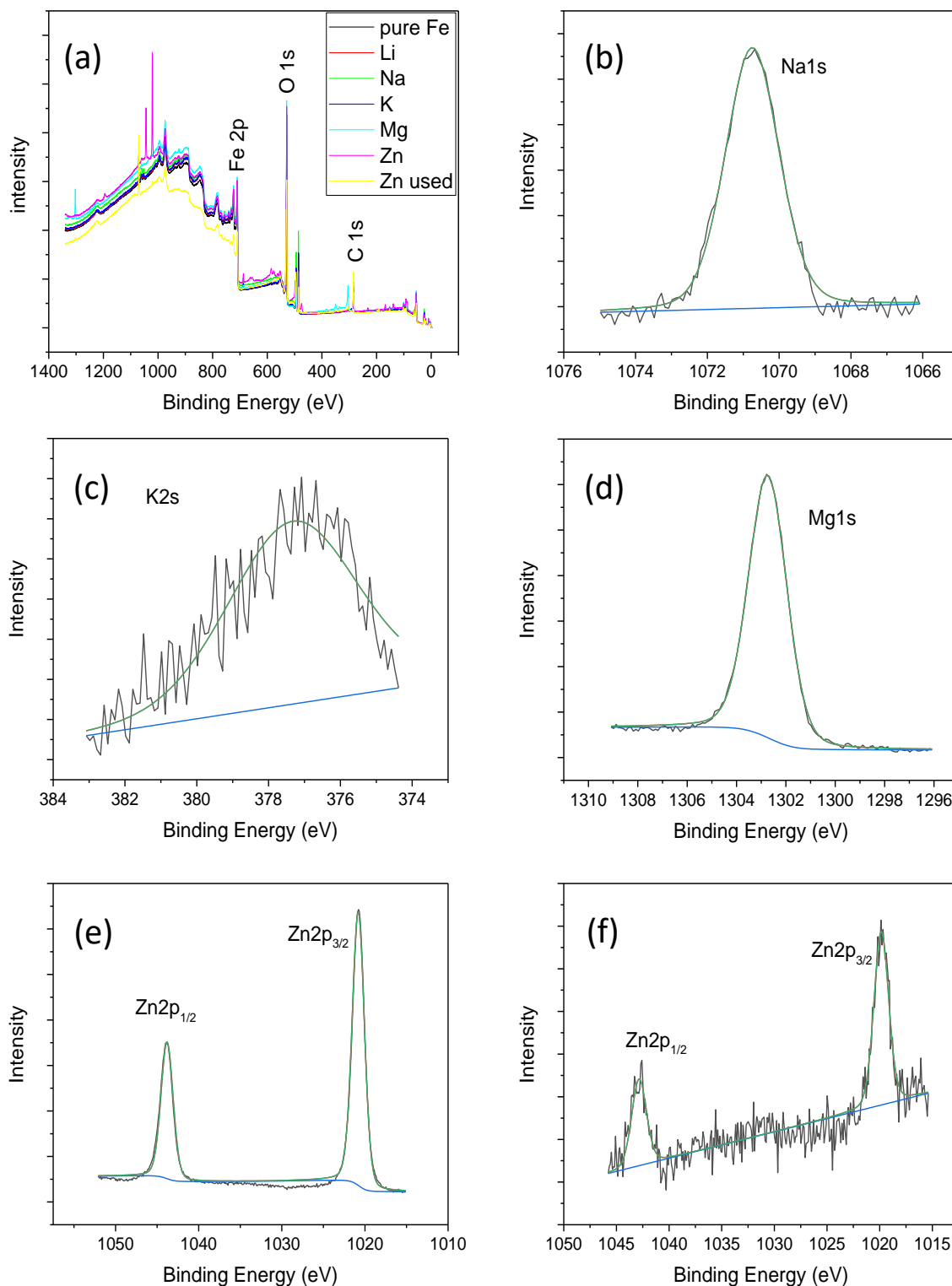


Figure 43 XPS spectra for (a) survey (b) Na 1s peak of fresh Na modified sample, (c) K 2s peak of K modified sample, (d) Mg 1s peak of fresh Mg modified sample, (e) Zn 2p peak of fresh Zn modified sample, (f) Zn 2p peak of used Zn modified sample.

XPS data could also give the approximate atomic ratio between different elements. The atomic ratio between two elements is calculated using equation 8.

$$\frac{n_1}{n_2} = \frac{a_1/S_1}{a_2/S_2} \quad \text{Eqn 8}$$

Here, n_1/n_2 is the atomic ratio, a is the peak area, and S is the relative sensitivity factors (R.S.F.).

The ratio between the doping metal and iron was calculated and is shown in Table 5. Owing to the overlaying of Li 1s peak (54.9 eV) and Fe 3p peak (52.6 eV), Li was not calculated. The results show that Na and K modified samples only doped about 7% on the surface, while Mg and Zn modified samples retained a higher ratio of doping metal ions. It should be noted that this data is for the surface layer and low resolution has reduced accuracy. However, it still proves that these surface-modified samples were not covered by a doping metal oxide layer, and even for Mg and Zn modified samples the doping ratio is still at a very low level.

Table 5 Surface relative sensitivity factors^{141, 142} and peak area. Ratio to Fe was calculated through equation 8.

element	Area (counts)	R.S.F.	Ratio to Fe(M:Fe)
Fe2p3	180819.32	2	1
Li1s	N/a		
Na1s	23326.29	4.0	0.0645
K2s	2242.231	0.34	0.0729
Mg1s	121412.7	4.06	0.33
Zn2p3	360557.7	7.4	0.539

3.3.3.5 Transmission Electron Microscopy (TEM)

To get nanoscale details of the surface-modified hematite electrode, transmission electron microscopy (TEM) images and electron diffraction patterns were obtained using a JEOL 2011 transmission electron microscope operated at 200 kV accelerating voltage. The glass slide was not suitable to put directly in the TEM chamber; instead, the film was scraped off to make samples for TEM.

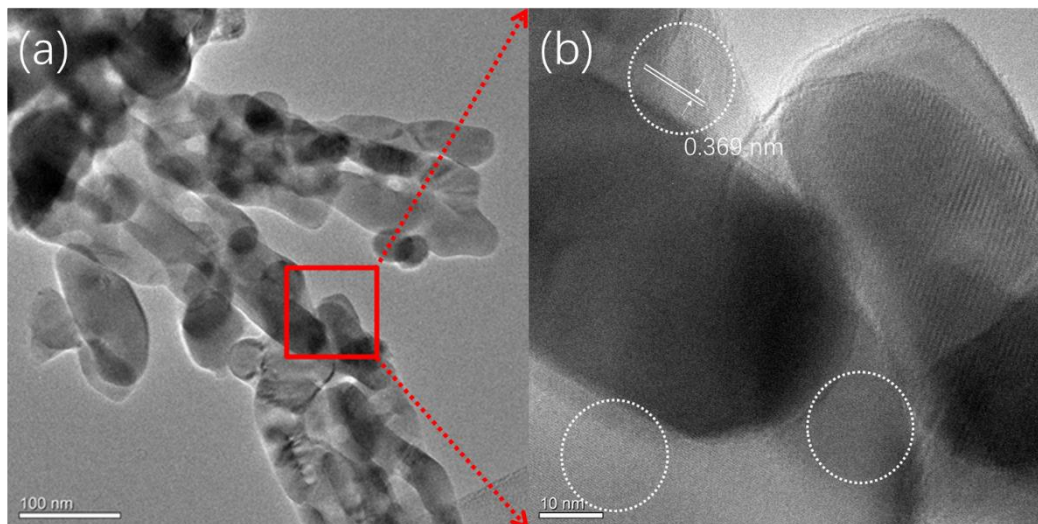


Figure 44 (a) TEM image of Zn doped Fe₂O₃. (b) High resolution image magnified the area in red box

Figure 44 (a) shows the high resolution of Zn doped Fe₂O₃. The Fe₂O₃ nanotubes were clear and show uniform size. The nanotubes are about 50 nm wide and 100 nm in length. No obvious other shape of particle was observed.

A high resolution image of the magnified area in the red box in Figure 44 (a) is shown in Figure 44 (b). In the high-resolution image, the lattice spacing is clear and shows parallel patterns. The lattice spacings in the round circle in the upper left, bottom left and bottom right areas are the same, and the spacing was measured to be 0.369 nm, corresponding to the (012) crystal plane of Fe₂O₃ (PDF 33-0664) which is proved by XRD measurement (Figure 34). The striped patterns on the righthand side were not lattice spacing; they are probably a Moiré pattern originating from the superimposition of two oblique crystals.

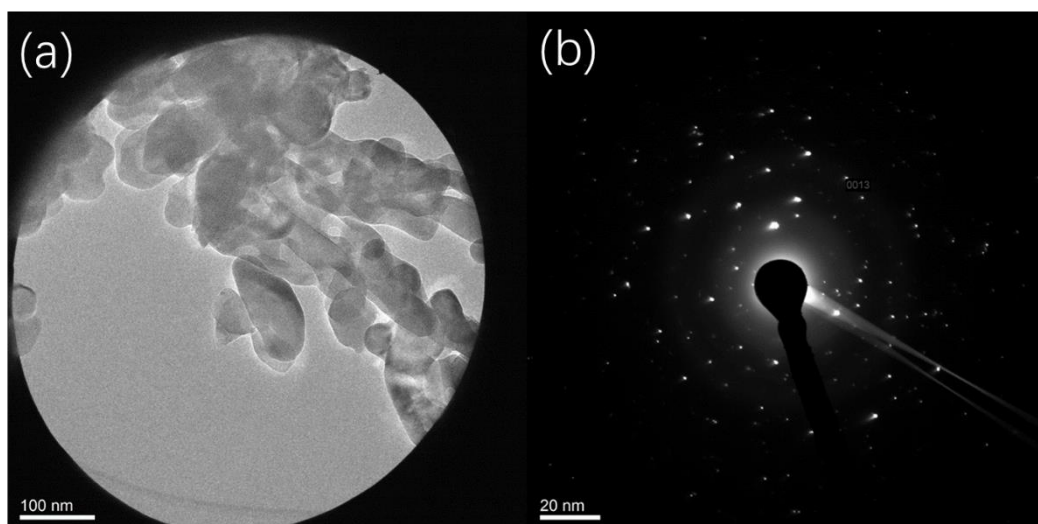


Figure 45 (a) TEM and (b) electron diffraction pattern of nanotubes samples.

Figure 45 shows the electron diffraction pattern of the nanotubes area. The pattern is made up of many crystallites so cannot be analysed. However, it still shows Zn doped Fe_2O_3 is crystalline.

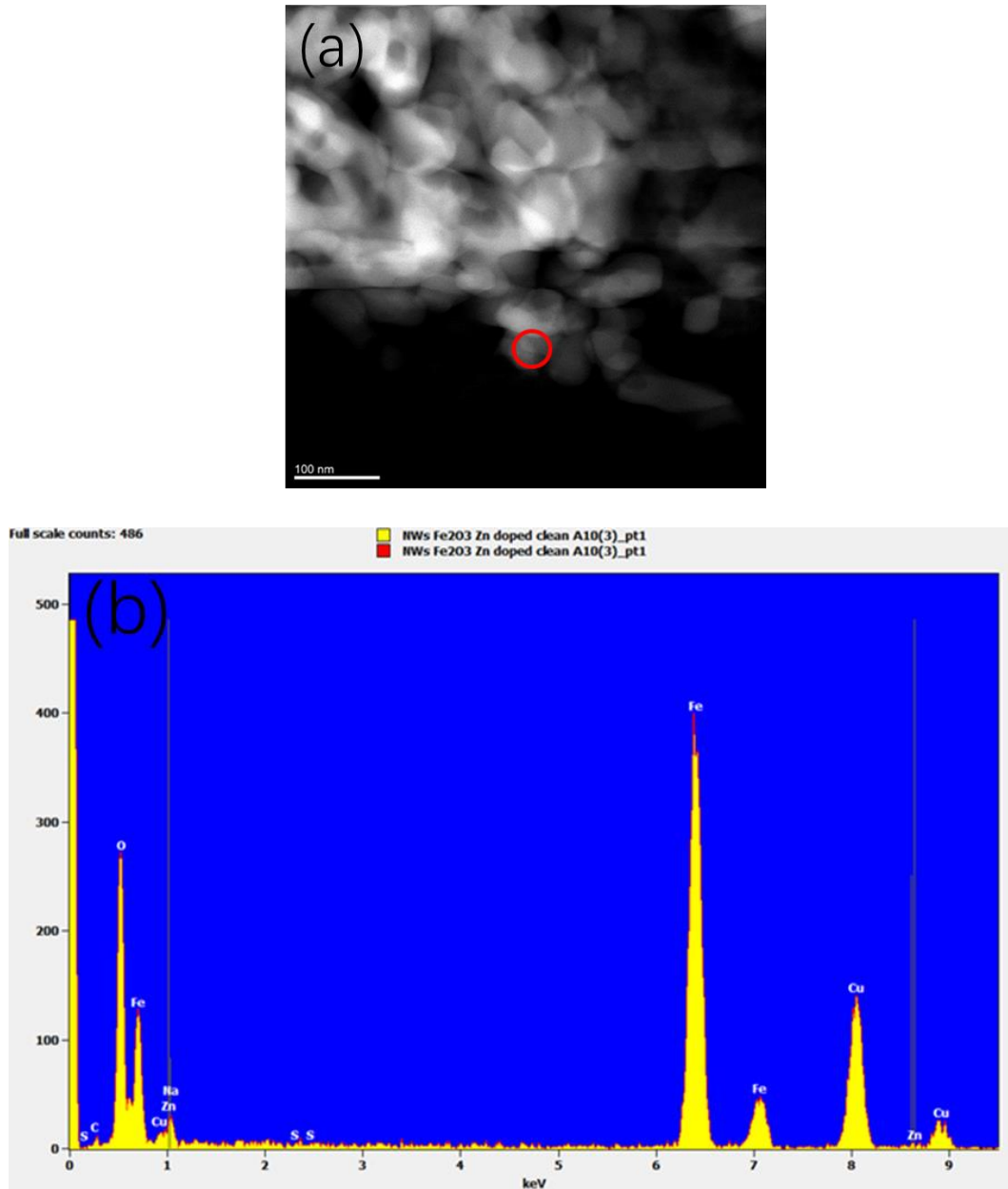


Figure 46 (a) STEM of Zn-doped Fe_2O_3 (b) EDX of red circled area showing Fe and Cu (from grid) but no Zn.

Figure 46 shows STEM and EDX of Zn-doped Fe_2O_3 sample. As shown in the EDX spectrum, Fe from hematite and Cu from the grid were clear and have strong peaks. However, there is no peak for Zn which means that there was no Zn (or only trace amounts) in this area.

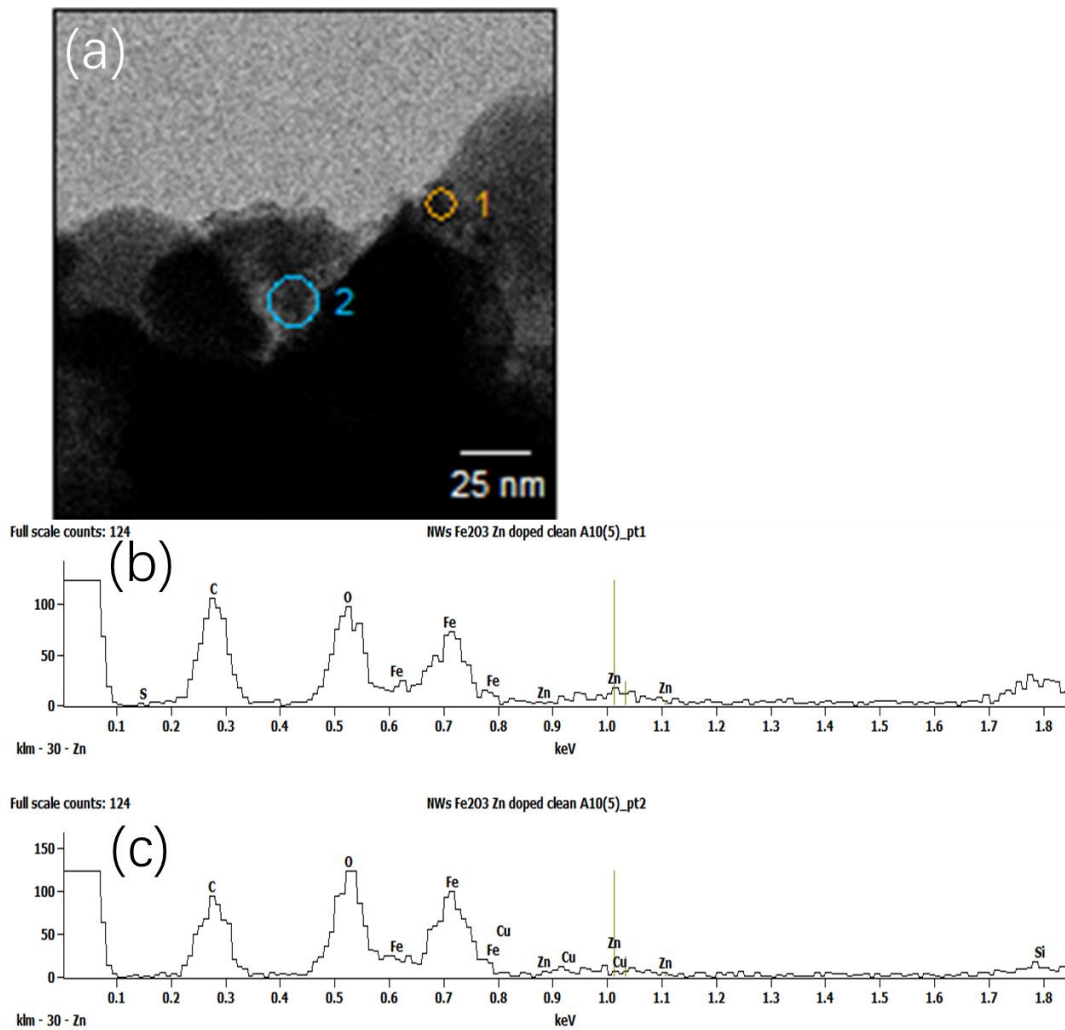


Figure 47 (a) STEM of Zn-doped Fe_2O_3 . EDX of (b) regions 1 (c) regions 2.

Figure 47 shows EDX data of different regions in STEM image in Figure 47 (a). Similarly, O and Fe from the Fe_2O_3 film and C from impurity show strong signals in both EDX spectrum. In region 1, a weak signal of Zn was found, the intensity of Zn at 1.01 keV was higher than that in region 2. It indicated that a small amount of Zn existed in some areas in the Zn doped Fe_2O_3 sample. However, considering the limit of sensitivity of EDX is about 1 part in 100, it would be very difficult to detect Zn if it was distributed evenly. The EDX results shows that the Zn probably is distributed evenly with no obvious concentrations in specific regions, which is consistent with expectations. In this experiment, the dopant only remains in trace amounts and is evenly distributed on the surface.

3.3.4 Photoelectrochemistry

3.3.4.1 Photocurrent and stability test

Photoelectrochemistry experiments were performed in a three-necked flask. 0.1M NaOH(aq) was used as the electrolyte solution. The Ag/AgCl reference electrode and platinum wire counter electrode were placed in the side necks and the sample was placed in the centre neck of the flask as the working electrode. An Xe lamp through 420 nm band pass filter with an irradiance of 1 sun was used as the light source. The potential was calculated using the following equation.

$$E_{RHE} = E_{Ag/AgCl} + -0.21V + 0.059 \times PH \quad \text{Eqn 9}$$

Where the E_{RHE} is the converted potential vs RHE and $E_{Ag/AgCl}$ is the potential measured by instrument.

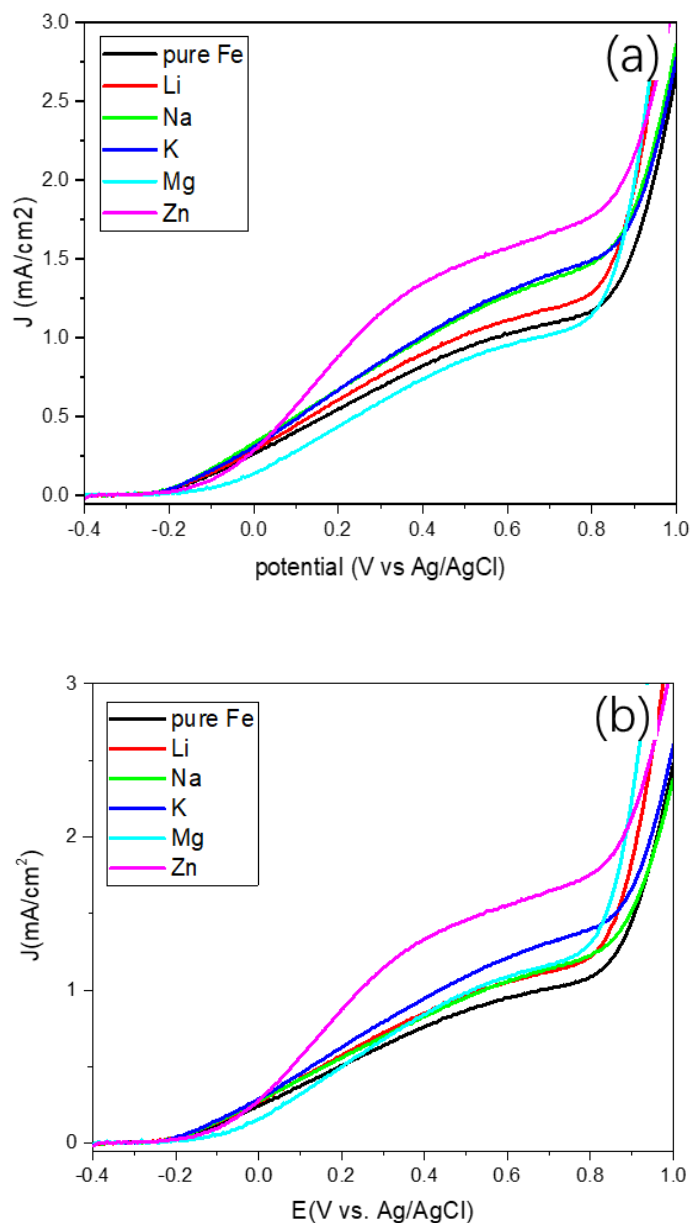


Figure 48 (a) Original and (b) normalized Linear sweep voltammetry results of unmodified and Li, Na, K, Mg and Zn modified samples. The normalizing method is the same as that which was used for UV-vis spectrum.

LSV results were normalized using the same method used for UV-vis spectrum (Figure 48 (b)) and showed that all these surface modifications have improved the photo current of the Fe₂O₃ electrode. The photo current at bias of 0.253 V (=1.23 V vs RHE) from highest to lowest are Zn, K, Li, Na and Mg modified

slides. The Zn modified slide, as the best one, performed a photo current of 1.03 mA/cm^2 at bias of 0.253 V , which is 77.6% more than that of the unmodified one (0.58 mA/cm^2). Considering they had the same substrate light absorption, these ion modifications have improved to varying levels. Compared to the published work in which a Zn-doped heteroepitaxial hematite photoanode was prepared and performed about 0.4 mA/cm^2 at 1.23 V vs RHE ^{143, 144}, similar samples prepared in this thesis show much higher photocurrent. Although those studies used a different synthesis method (pulsed laser deposition), it still proves that the surface modification method studied in this thesis is cheaper and more efficient.

To further study the stability of these electrode samples, two different experiments were run. Figure 49(a) shows that the photo current had a significant decline (about 25% at 0.253 V) after the EIS experiment compared to the data collected before EIS. However, a long-time continuous Chronoamperometry experiment (bias 0.253 V) showed that the sample was stable and only lost about 8% of photo current (Figure 49 (b)). The difference in stability performance indicates that the EIS experiment's conditions may be harmful for the electrode. The probable reason may refer to the alternative current applied in the EIS experiment. The high frequency may change the depletion layer between the electrode and electrolyte, thereby decreasing the photo current.

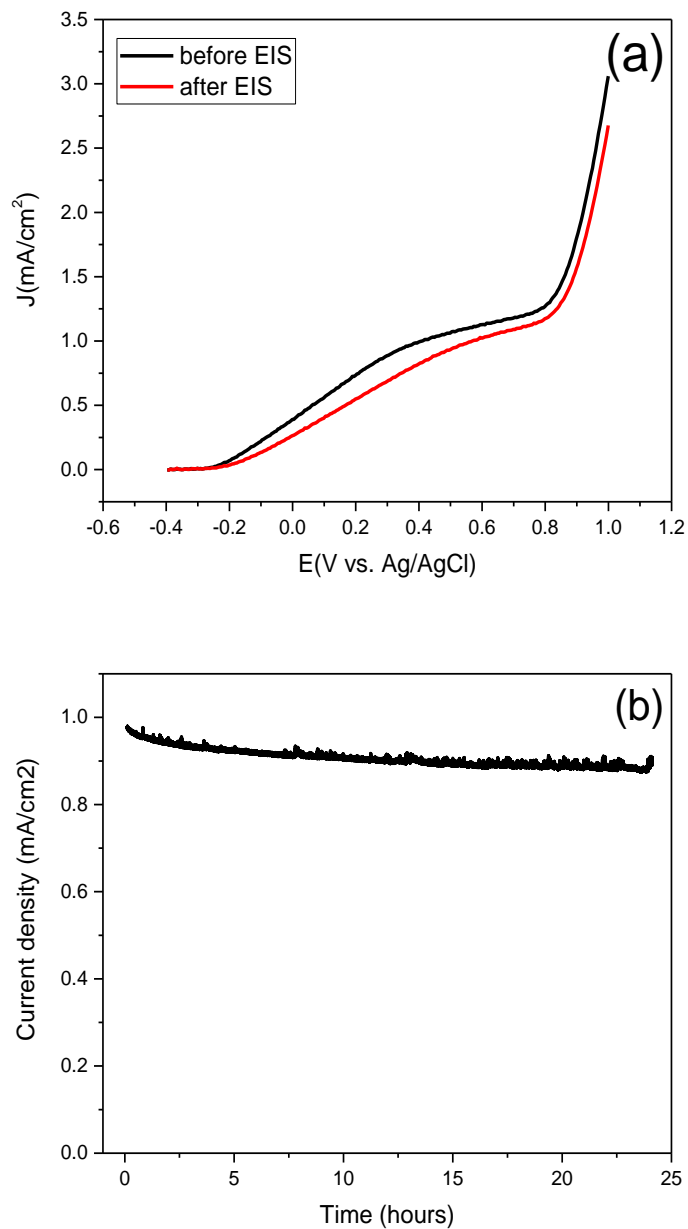


Figure 49 Two different stability experiments of unmodified Fe_2O_3 electrode. (a) Comparison of LSV results collected before and after EIS experiments. (b) Long time (24 hours) Chronoamperometry experiments.

3.3.4.2 Mott-Schottky plots

To further understand the photo electrochemistry behaviours, Mott-Schottky plots were recorded in the dark. Based on the positive slope, all samples are typical n-type semiconductors.

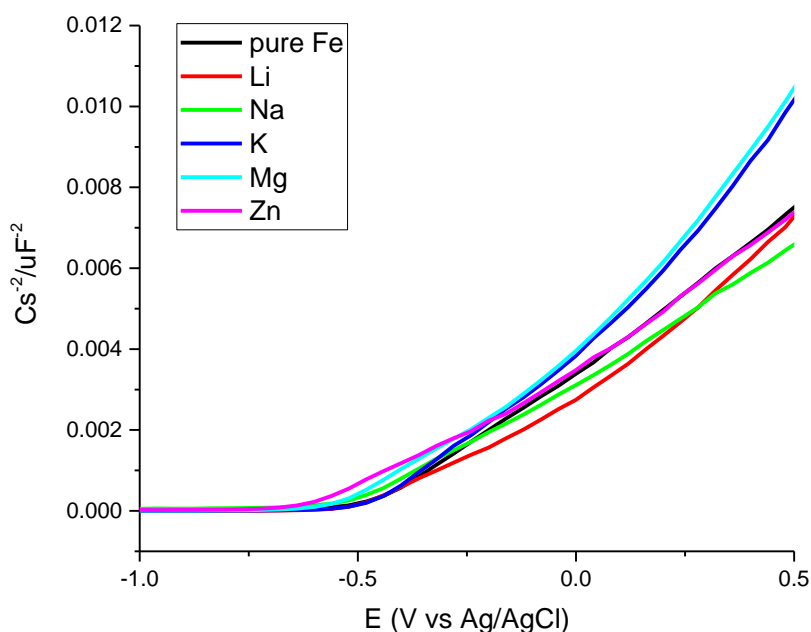


Figure 50 The Mott-Schottky plots of unmodified and Li, Na, K, Mg and Zn modified Fe_2O_3 electrodes.

From the Mott-Schottky plots, Donor density and flatband potential were calculated and are listed in Table 6. The ND values show that the Zn modified sample has the highest donor density among the electrodes. This high donor density could be evidence of the high photo current. It is assumed that the onset potential is approximately equal to the flatband potential. Table 6 shows that the Li and K modified electrode had no obvious change of flatband potential

compared to the unmodified pure Fe₂O₃ electrode. The Zn modified sample has the most negative flatband potential among the electrodes.

Table 6 The Donor density and Flatband potential calculated from the Mott-Schottky plots of unmodified and Li, Na, K, Mg and Zn modified Fe₂O₃ electrodes.

	Donor density (10²¹ cm⁻³)	FlatBand potential (V vs Ag/AgCl)
Pure Fe	1.403	-0.5066
@Li	1.675	-0.5041
@Na	1.718	-0.5636
@K	1.236	-0.5020
@Mg	1.326	-0.5568
@Zn	1.927	-0.6554

3.3.4.3 Impedance Spectroscopy (EIS) experiments

For further details of the underlying mechanism, the Nyquist plots of unmodified and Li, Na, K, Mg and Zn modified samples were measured under 1-sun light irradiation.

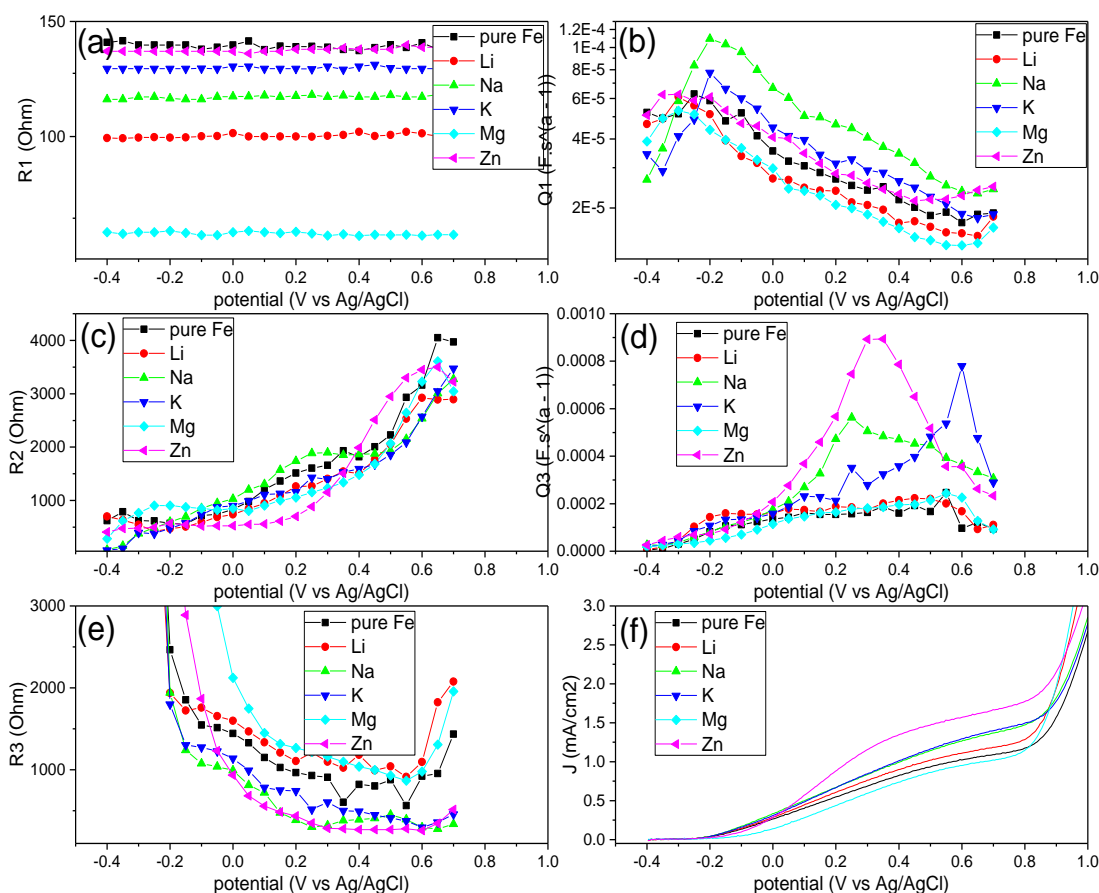


Figure 51 Analyzed (a) $R1$, (b) $Q1$, (c) $R2$, (d) $Q3$, and (e) $R3$ value change against the potential. (f) LSV figure for comparison.

The experiments were performed at potentials from -0.4 V to 0.7 V vs Ag/AgCl and recorded at intervals of 0.05 V. The data files were analysed using the software and obtained the change parameter value as shown in Figure 51. The $R1$ means the resistance from Fe_2O_3 to FTO, which is consistent and stable when the potential changed. The $R1$ of all samples are in a range from 70 ohms to 140 ohms owing to the different interfacial condition between Fe_2O_3 and FTO. However, these values are quite small compared to $R2$ and $R3$, so the differences are not considerable. $Q1$ is capacitance of bulk semiconductor, related to dielectric of hematite in origin. For all samples, unmodified and

modified, Q1 shows the same trend. R2 is also related to the bulk semiconductor. It represents the surface state as a recombination centre trapping holes from the valence band and electrons from the conduction band. As the potential increased, it facilitated recombination of holes and electrons at the surface state, and the resistance became higher, as shown in Figure 51(c). Q3 and R3 show the condition of interface between the surface of the electrode and the electrolyte solution. Q3 is termed the surface state capacitance (C_{ss}) with an expression given by:

$$C_{ss} = A \frac{N_{ss} q^2}{k_B T} f_{ss} (1 - f_{ss}) \quad \text{Eqn 10}$$

Where N_{ss} is the density of surface state, A is the area of electrode, k_B is Boltzmann's constant, T is absolute temperature, q is elementary charge and f_{ss} is the occupancy of the state.

As the potential increased, more carriers were excited and occupied more positions in state. According to the $f_{ss} (1 - f_{ss})$ part, the Q3 should trace a peak along the increasing potential. Moreover, two things could be understood from the equation. First, the more negative the position of the peak is, the easier the carriers are excited and recombination of the holes and electrons becomes more difficult. Secondly, the value of the peak point is related to N_{ss} . As a result, the Zn modified electrode has the most amount of surface state density where it is easier for holes to be excited and transfer to the donor species in solution. These behaved as high photo current in the LSV figure.

We also noted that the increase of Q3 is correlated to the decrease of R3. The converse changing trend indicated that the hole transfer for the oxygen evolution reaction occurred through the surface state.

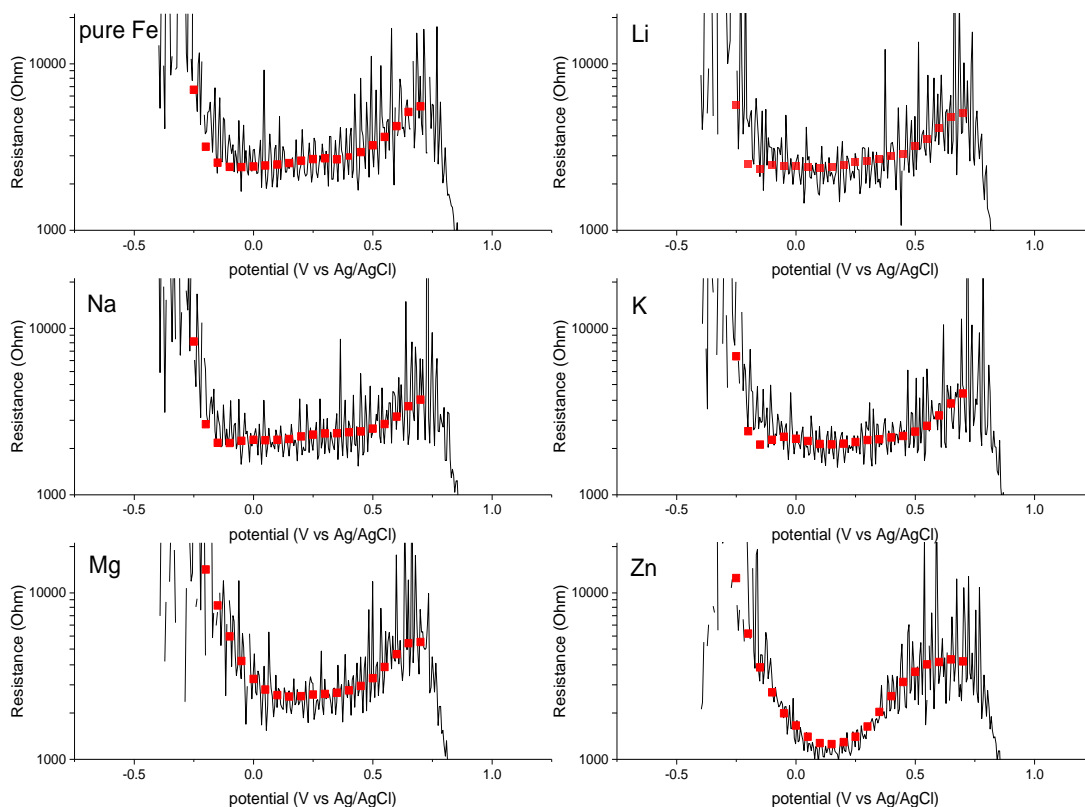


Figure 52 Total resistance calculated from LSV (black line) and sum of $R_1+R_2+R_3$ (red square point).

From the analysis results, the total resistance of the system could be easily calculated by the sum of three resistances, R_1 , R_2 and R_3 . On the other hand, total resistance (R_{tot}) could be worked out from the LSV figure¹¹⁰:

$$R_{tot} = \left(A \frac{\partial J}{\partial V} \right)^{-1} \quad \text{Eqn 11}$$

Here A is the surface area of electrode. By calculating differential for the LSV figure, total resistance could be obtained.

Figure 52 shows total resistance obtained from two methods. The two results matched well which is evidence that the analysis of EIS is correct. Compared to the resistances, the Zn modified sample showed an obvious decline and the lowest value from bias of -0.05 V to 0.35 V. This low resistance reflects in the highest photo current among the samples.

3.4 Conclusion

In this chapter, Fe₂O₃ film was prepared and surface modified with metal ions to improve photo properties. Fe₂O₃ is widely used as a photo electrode semiconductor for oxygen evolution reaction. However, it still has some disadvantages, especially the high carrier recombination rate and the poor hole transfer from semiconductor to solution. Here we used dip-coating and low temperature calcination to surface modify the Fe₂O₃ electrode. Among the several ion candidates, Zn was the most successful in improving the Fe₂O₃ electrode efficiency, the photo current at 1.23 V vs RHE reached 1.03 mA/cm² which is 77.6 % higher than unmodified pure Fe₂O₃ electrode. This improvement is higher than those samples which were surface modified through overlayer deposition^{145, 146}. By characterization experiments, the morphology and structure were studied. The surface modification did not change the surface morphology. The quantity of metal ions was too small to be detected on XRD or EDX. STEM EDX was carried out and detected several areas, in only one of which was found a weak signal of Zn. This proved that the dopant was distributed evenly on the surface of Fe₂O₃ film. UV-visible absorption spectrum showed that all the samples had the same Fe₂O₃ base with a similar shape of figure. A normalization method was applied to transfer the LSV figure and exclude the effect of distortions in the glass. XPS was

carried out to establish details about the composition of the surface layer. It proved that the metal ions dopant only existed in trace amounts on the surface. All the characterizations showed that the surface modification in this chapter was different from many previous studies where large amounts of dopants or co-catalysts are deposited on the surface. Hence the main cause of enhancement of the photo properties is the improvement of surface state and charge transport.

PEC experiments were performed, and all modified samples were shown to have improved for oxygen evolution efficiency. Zn modified samples took the highest photo current among the electrode samples. Mott-Schottky plots showed that the Zn modified sample had the highest donor density, considered as the vital role in OER experiments. The EIS data was analysed and parameters in detail were obtained and compared. This also gave evidence that the Zn modified sample had the most surface state density for the hole transfer take place, which could explain the significant improvement in the photoelectrochemistry experiments.

Chapter 4

Semiconductor coated F-SnO₂
nanofiber surface electrode

4 Semiconductor coated F-SnO₂ nanofiber surface electrode

4.1 Introduction

4.1.1 Electrospinning

As mentioned in chapter 1.8, preparing unique morphology with high specific surface areas is an effective method to synthesize photoelectrodes with high photo properties. The unique morphology may affect the diffusion length of photogenerated carriers, and the high surface area provides more reactive sites for water oxidation which take place.

Electrospinning is a promising method to prepare nanofibers with high surface areas and has been used to prepare many different nanomaterials. The electrospinning method requires a viscous precursor, normally PVA¹⁴⁷⁻¹⁴⁹, PVP¹⁵⁰⁻¹⁵² or similar polymers to generate continuous nanowire and so form a nonwoven mat. During the preparation, evaporation of the solvent forms microporous nanofibers which provide a high surface area. This makes it an ideal support for drug delivery^{153 154, 155}, tissue engineering¹⁵⁶⁻¹⁵⁸ and other similar applications.

Unlike in other methods, when using electrospinning to prepare film, the sample is not simply flat. Nanofibers cross and connect with each other and form a three-dimensional (3D) network which is a naturally good framework. Electrospinning has been widely used to prepare semiconductor nanofiber materials. Electrospun metal oxide nanofibers perform well in PECs¹⁵⁹⁻¹⁶¹, solar

cells¹⁶²⁻¹⁶⁴ and other areas due to their high surface area and porous structure. Moreover, because of the 3D structure and the nanofiber mat, the electrospun materials could be further modified.

Zhenjun Chang¹²⁷ reported firecracker-shaped ZnO/polyimide (PI) hybrid nanofibers. The electrospun PI fibres were dip-coated with ZnO nanoparticles which act as seeds in the subsequent hydrothermal process. The hybrid nanofibers exhibited high photocatalytic activity.

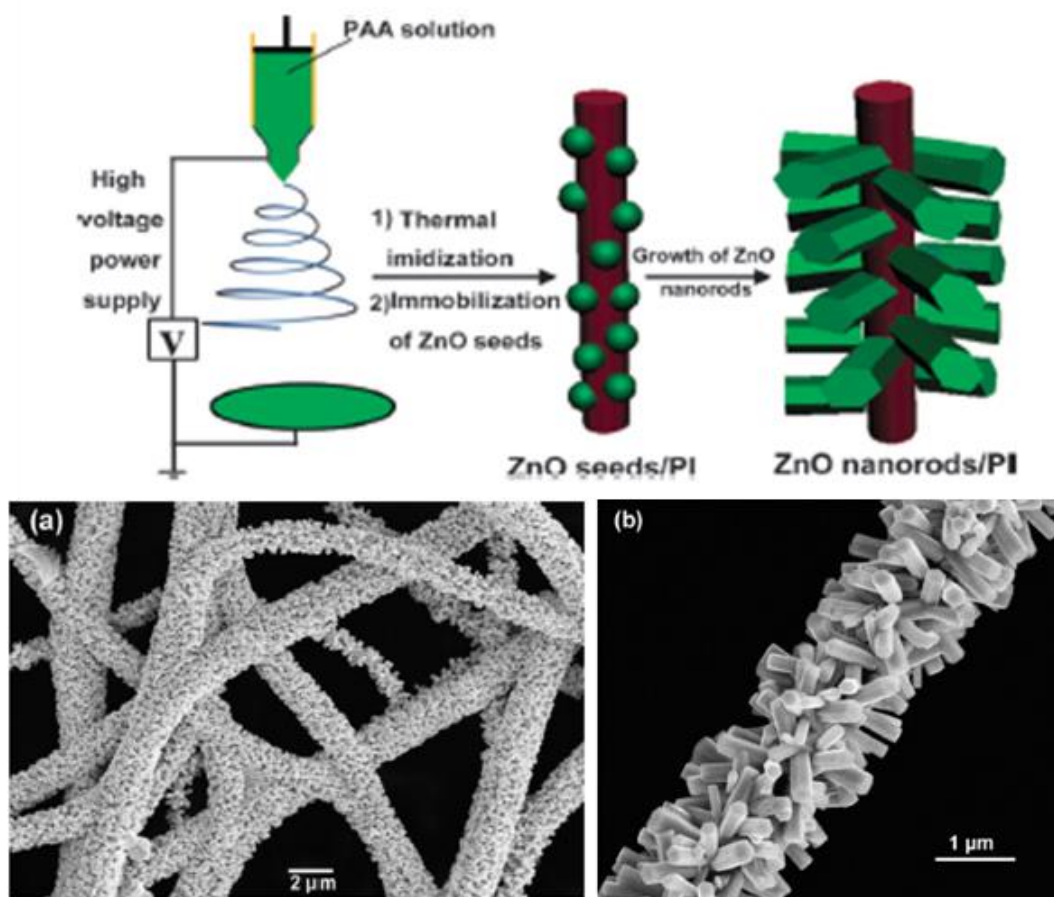


Figure 53 “Firecracker-shaped” ZnO/polyimide hybrid nanofiber (the upper diagram is the process of fabrication and the lower section is the (a) SEM image and (b) HR-SEM image of the sample’s fibres).¹²⁷

Christopher Drew and his co-workers¹⁶⁵ immersed an electrospun nonwoven polyacrylonitrile fibre membrane in an aqueous solution of metal halide salts and halogen scavengers at room temperature to apply the metal oxide coating. By this method, the core was successfully coated with tin dioxide and titanium dioxide and a homogenous metal oxide core with thickness of 20 to 80 nm was prepared.

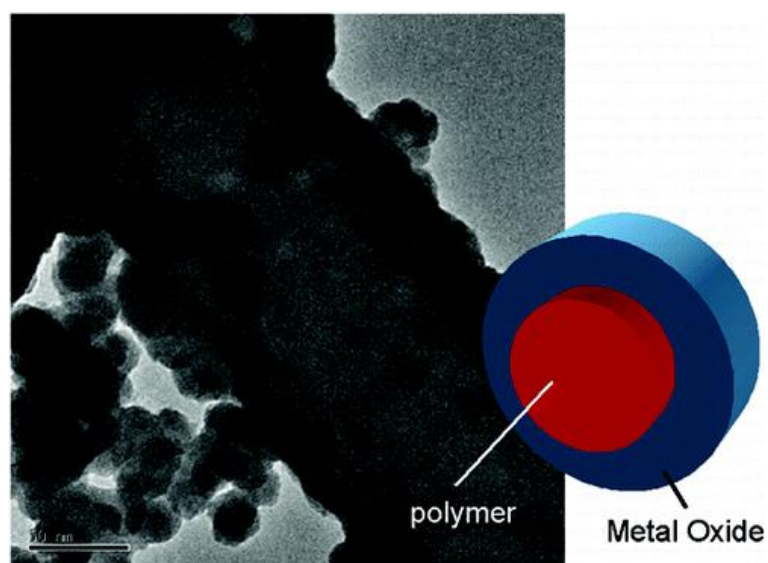


Figure 54 Core-shell metal oxide/polymer fibres.¹⁶⁵

D. Regonini *et al.*¹⁶⁶ prepared nanofibers from TiO_2 which were then dispersed in a sol-gel solution. After that, a clean FTO glass was dipped in the sol-gel solution and finally synthesized a TiO_2 photoelectrode. This photoelectrode showed significantly higher photoactivity than a commercially prepared P25 electrode.

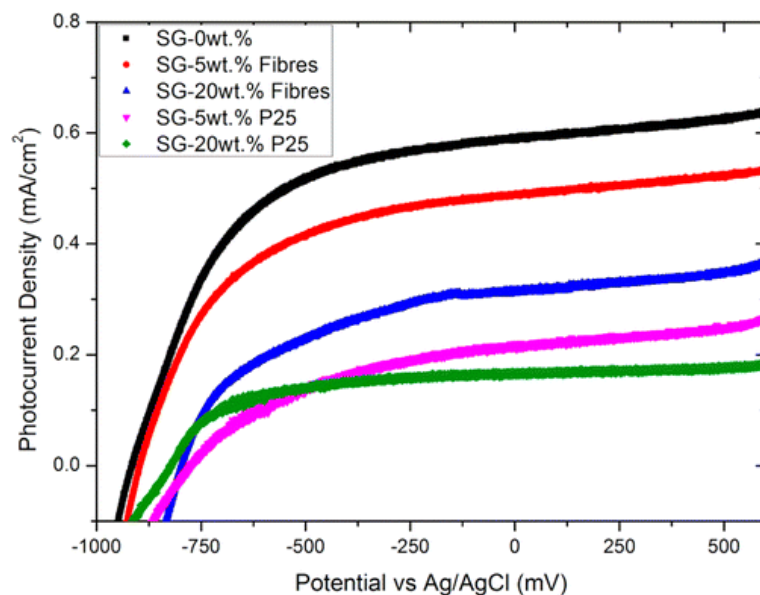


Figure 55 Photocurrent measurements performed at a light intensity of 1.5AM in 1M KOH, SG (sol-gel) and SG-fibres, as well as SG-P25 composite photoelectrodes.¹⁶⁶

Li Zhang *et al.*¹⁶⁷ reported Ag-TiO₂ nanofibers prepared by the electrospinning and photoreduction method. Compared to pure TiO₂ nanofibers, this Ag-TiO₂ photocatalyst showed higher photocatalytic activities. The Ag nanoparticles served as charge-transfer sites and broadened the spectral absorption band of the catalyst.

Electrospinning is a simple and versatile method and could be easily developed to industrial production. It has potential in preparing nanofiber semiconductor materials.

4.1.2 CdS photocatalyst

CdS is a popular photocatalyst with a small band gap of 2.3 eV¹⁶⁸ which allows an absorption of visible light. Also CdS is an n-type semiconductor and has long diffusion length for photogenerated carriers⁴⁶. All this makes CdS a promising photocatalyst and, in fact, it has been used for H₂ evolution reaction (HER) owing to the more negative conduction band edge than H₂O/H₂ reduction potential over a wide pH range. However, the CdS electrode can be easily photocorroded by the photogenerated holes.¹⁶⁹ As a result, CdS catalysts normally have to work in a solution containing Na₂S and Na₂SO₃ as sacrificial reagents to prevent the photocorrosion. Much research has been done to improve the stability and photoactivity of CdS.

Various methods have been tried to improve CdS as a catalyst, such as preparing by a co-catalyst or dopant (TiO₂¹⁷⁰⁻¹⁷², ZnO¹⁷³⁻¹⁷⁷, MoS₂¹⁷⁸⁻¹⁸⁰, FeSe¹⁸¹, WS₂¹⁸² and noble metal/metal oxides¹⁸³⁻¹⁸⁷) or by changing the synthesis method, for instance, one-pot synthesis¹⁸⁸⁻¹⁹¹, microwave irradiation¹⁹²⁻¹⁹⁴, organometallic precursors^{195, 196}, *etc.*

Dengwei Jing *et al.*¹⁶⁸ prepared a CdS photocatalyst by thermally treating the prepared CdO in the presence of H₂S. This CdS material had a higher stability against both air oxidation and photocorrosion during photocatalytic reactions. Meanwhile, the photocatalytic hydrogen evolution was also remarkably enhanced due to the special nanostep structure on the surface of the sulphide photocatalyst.

Similar methods have also been tried, in which the CdS was prepared by reacting Cd salt, such as CdO, with sulfide salt like H₂S gas or Na₂S. The reaction commonly takes place in aqueous solution or under H₂S atmosphere. Hongjian Yan and his co-workers¹⁹⁷ prepared CdS nanoparticles by adding

aqueous solution of Na_2S slowly to $\text{Cd}(\text{OAc})_2$ solution under vigorous stirring. With Pt and PdS as co-catalyst, the CdS sample was very stable and achieved a quantum efficiency of up to 93 % in HER in the presence of sacrificial reagents under visible light irradiation. Jum SukJang *et al.*¹⁹⁸ prepared a CdS photocatalyst by adding Na_2S aqueous solution drop-by-drop into $\text{Cd}(\text{NO}_3)_2$ solution which was dissolved in isopropyl alcohol. Then the CdS photocatalyst was coupled with TiO_2 to form a nanocomposite photocatalyst. Under visible light it performed high photoactivity of hydrogen production from water containing sacrificial reagent.

4.2 Chapter aim

In this chapter, the main aim is to develop a new nanofibered surface substrate photoelectrode which will provide 3D framework support for semiconductor coating. The surface is very important because it is the interface between the electrode and the electrolyte where the main reduction or oxidation reactions occur. The 3D nanofiber network has a large surface area which could load more semiconductor and provide a more reactive centre in the PEC experiment. We aim to use the electrospinning method to prepare such a substrate, and try to coat it with different photoactive semiconductors to obtain a photoelectrode with higher photo properties.

Therefore the following aims need to be achieved:

- By electrospinning prepare a stable, high surface area and conductive substrate. Deposit semiconductors like CdS and Fe_2O_3 on the nanofibered

substrate for better properties. To make the experiments repeatable, several points are required:

- ⇒ The FTO glass should be fresh and cleaned using same cleaning method.
 - ⇒ The precursor solution should be prepared and used immediately to avoid composition change.
 - ⇒ The electrospinning process should be carefully controlled. All the parameters, such as temperature, humidity, voltage, spinning distance, flow rate of precursor and conditions of syringe should be the same.
 - ⇒ Samples such as CdS/pure FTO and nanofiber/FTO glass, should be prepared for comparison with the measured samples.
 - ⇒ Dipping time of CdS coating process should be restricted.
 - ⇒ Irradiation position and light power used in PEC experiments should be carefully checked before experiment to ensure the measurements are taken under the same conditions.
- Investigate factors of electrospinning and adjust them to form stable and conductive substrates.
 - Characterize the samples and quantify and qualitatively analyse the effect of loading of semiconductors.

- Run photoelectrochemistry experiments for different samples. Analyse how the experiment process affects the photo properties. Find feasible ways to improve the photo performance of the samples.

4.3 Characterization

4.3.1 Synthesis of F-SnO₂ nanofiber film on FTO glass

F-SnO₂ nanofiber-covered FTO glass was prepared through electrospinning. In a typical experiment, 1.4 g of SnCl₄·5H₂O, 0.8 g of Polyvinylpyrrolidone (PVP), 6.89 g of ethanol and 2.3 g N,N-Dimethylformamide (DMF) was mixed and stirred for 5 hours to form a transparent and homogenous solution, to which was then added 143.1 μL of saturated NH₄F solution and stirred for one more hour to obtain the final precursor. The precursor was white due to the formation of particles from hydrolysis of SnCl₄ and had to be used immediately to avoid coagulation. The atomic ratio between F and Sn is 0.5, which has been proved to be the best ratio for FTO formation.

The solution was electrospun into nanofibers onto a 10 mm* 30 mm FTO glass. Note that the FTO glass was placed on grounded aluminium foil, fixed and connected to the foil using copper tape. Electrospinning was carried out using a 5 mL syringe with a needle of 0.514 mm inter diameter, and a high voltage from a DC power supply of 10 kV over a 6 cm gap between the spinneret and collector. A peristaltic pump was used to deliver the solution at a flow rate of 0.05 mL min⁻¹. After 7 minutes of spinning, the FTO glass was covered with white mat film and heated at 450°C for 2 hours at a rate of 1 °C/min. After

heating, the fiber film became black and stable on the FTO glass. Other ratios of precursor and temperature have been tried for comparison, as these samples remained white after the last process, and the films were fragile and not firm on the FTO glass substrate. The black film was estimated to have the best parameters owing to the carbon which will be discussed in the following chapters.

4.3.2 Decorating CdS on F-SnO₂ nanofiber photoelectrode and pure FTO glass

To obtain better photoactivity, CdS was coated on to F-SnO₂ nanofibers using the SILAR method.¹⁹⁹ This is a simple and controllable way to mildly coat a substrate with the semiconductor. Cd(CH₂COO)₂ was dissolved in ethanol to form Cd solution (50 mM) and 3 mL was placed in a glass vial (8 mL size). Meanwhile 3 mL of Na₂S aqueous solution (50 mM) was prepared as S solution and placed in another glass vial. The prepared F-SnO₂ nanofiber electrode was stood vertically in the glass vial of Cd solution for 1 minute and then dried under flow of N₂. The electrode was then put vertically in the glass vial of S solution for 1 minute and dried again under N₂. The process was repeated eight times and then the electrode was heated under argon at 400°C for 30 minutes with ramp rate of 1 °C/min. After cooling at room temperature, the completed CdS-coated F-SnO₂ nanofiber photoelectrode has a yellow colour. During the process, the Cd²⁺ and S²⁻ ions reacted on the surface of fibres and, after heating treatment became stable CdS particles.

By comparison, CdS was prepared using the same method, coated on a pure FTO glass. The properties of CdS coated fibres and pure FTO glass samples will be compared and discussed in the following chapters.

4.3.3 Characterization

4.3.3.1 Scanning electron microscopy (SEM) and Energy-dispersive X-ray spectroscopy (EDS)

SEM was performed to get the details of surface morphology. Figure 56 shows the SEM images of samples before and after CdS coating. As shown, the surface of the FTO glass was covered with F-SnO₂ nanofibers which form a complex framework and increase the surface area of the substrate (Figure 56 (a)). After CdS coating, the fibre can clearly be seen to be coated with membrane (Figure 56 (b)) which is proved as CdS in the following chapters. HRSEM images show more details of the fibres. Figure 56 (c) is the image of F-SnO₂ fibre which shows that the surface is wrinkled and covered by small particles. This is because after electrospinning the fibres contain large amounts of PVP and solvent which decomposed and evaporated during the drying and heating process. The large mass loss created not only the wrinkled surface but also a useful porous structure. This special surface morphology further improves the surface area and additionally, enhances the contact between CdS coating and the fibre support. Figure 56 (d) shows a layer of CdS coated on the fibre with a thickness of about 100 nm.

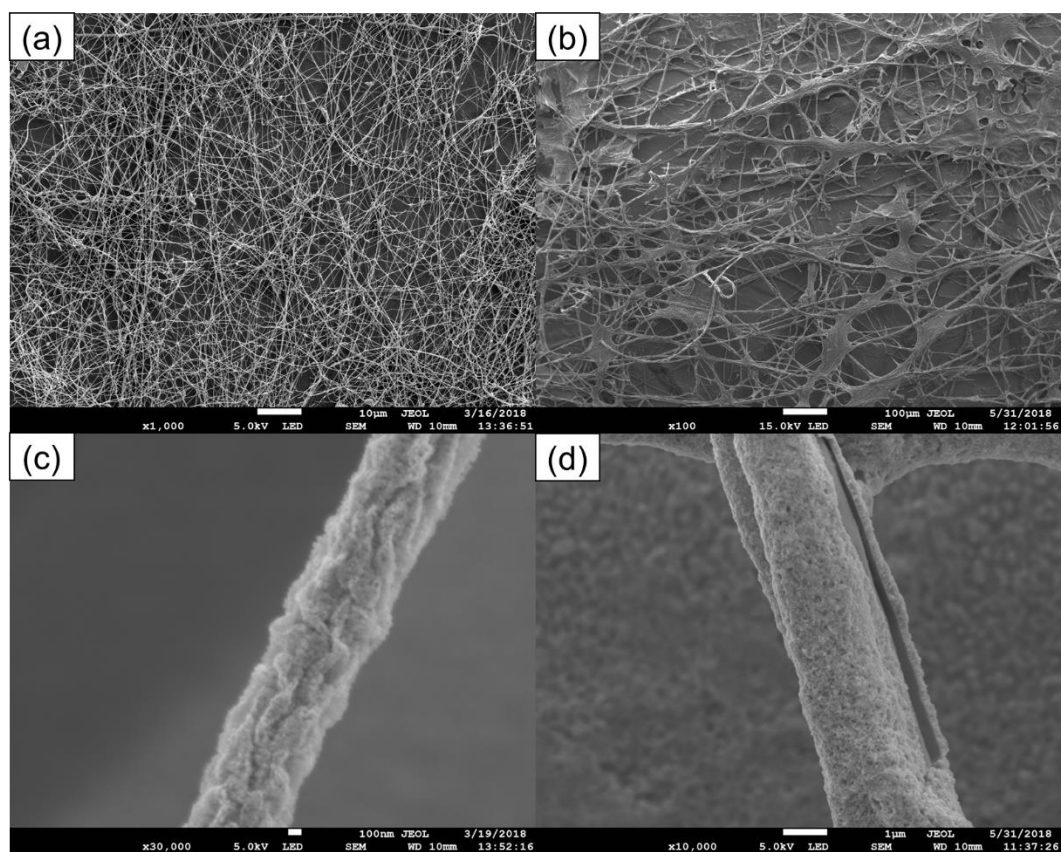


Figure 56 SEM and HRSEM image of fibre covered FTO glass (a)(c) before and (b)(d) after CdS coating.

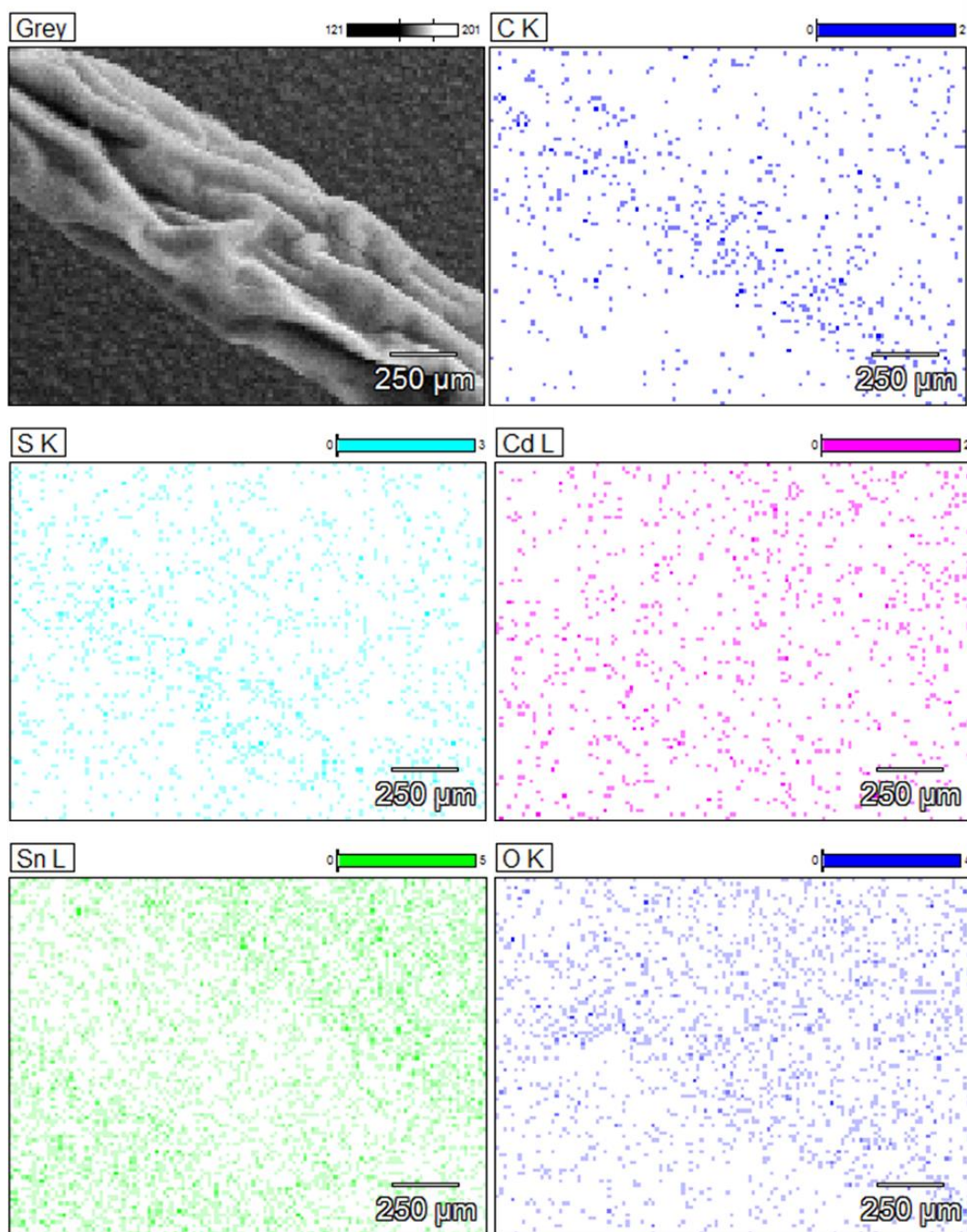


Figure 57 EDX mapping of C, S, Cd, Sn and O elements corresponding to SEM images.

EDX measurements were carried out to study the element dispersion on the surface of CdS-coated F-SnO₂ fibre substrate. Figure 57 shows the EDX mapping image around a piece of CdS coated fibre. As shown, the Cd and S

were homogenous throughout the image and no obvious concentration is shown at the surface of the fibre. A possible explanation is that due to the similar material, the CdS coated both the fibres and the surface of the FTO glass rather than accumulating on the fibres. However, by careful checking, we found that at the fibre area the signal of S is slightly stronger than Sn. It may be that the wrinkled surface of the fibres leads to increased coating by CdS. Another noticeable thing is that the carbon shows higher density in fibres area. This supports our hypothesis that the final samples still contained carbon in the fibres.

4.3.3.2 X-ray diffraction (XRD)

XRD was carried out to study the composition and structure in the samples. All the samples have strong peaks of FTO glass corresponding to standard peak data which are shown in the figure using vertical red lines. For CdS-coated 7 min electrospun electrode (purple line), several more peaks were found. Some of these extra peaks are of CdS which are marked using an asterisk (*). However, there are still two unknown peaks at low angle positions (7.45° and 10°). These unknown peaks do not belong to FTO, CdS or other possible chemicals. They may be unburnt organic impurities generated during the heating process.

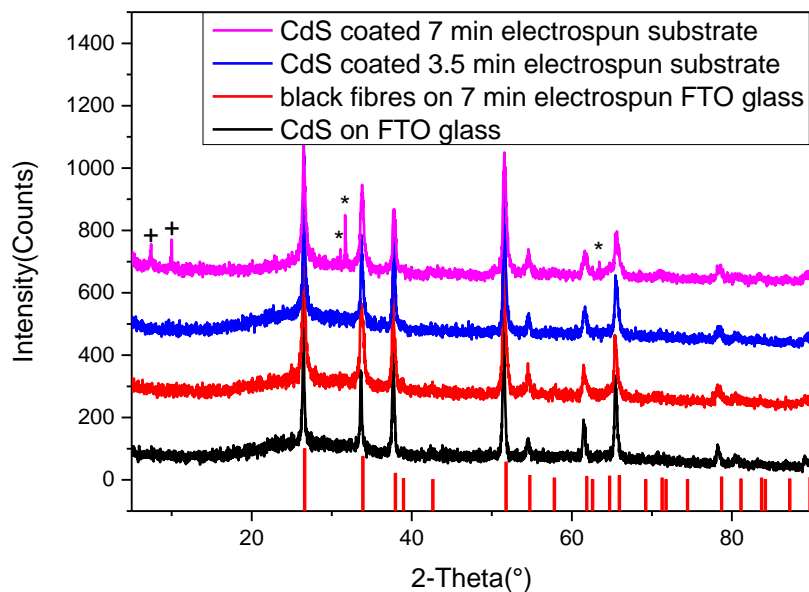


Figure 58 XRD pattern of samples with and without CdS coating. The peaks of FTO (PDF 46-1088) are shown using vertical red lines. The peaks of CdS (PDF 43-0985) are marked using asterisks (). Two unknown peaks are marked using plus (+).*

4.3.3.3 UV-visible spectroscopy and photography

UV-visible spectroscopy was performed on CdS-coated samples, as well as blank FTO glass and fibre-covered samples for comparison. Figure 59 shows the transmission and reflection spectrums. As shown in Figure 59 (a), the fibre-covered samples performed very low transmission over the visible light range. The CdS-coated 7 minute electrospun sample has lower transmission than that of the 3.5 minute electrospun sample. This proves that the electrospinning time is in inverse ratio to the transmission. The comparison between samples with and without CdS coating (purple and blue lines) show that the CdS coating has

decreased the transmission of the electrode. Furthermore, the difference between blank FTO glass and CdS coated FTO glass is smaller than the difference on the fibre-covered samples. This could be evidence that the complex surface structure of fibre-covered sample increased the loading of CdS on the substrate.

The transmission figure seems to prove that the CdS-covered sample has better photo absorption. However, on checking the reflection spectrum, it was found that the CdS-coated 7 minute electrospun sample shows higher reflection than both the 3.5 minute sample and the sample without CdS coating. The comparison of CdS coating on normal FTO glass (black and red lines) also show a higher reflection than on the CdS-coated sample. A possible explanation is that the coating of CdS makes the surface flatter and improves the reflection. To obtain the details about absorption which directly relate to the photo property, we used a simple equation (equation 12) to calculate UV-visible absorption spectrum as shown in Figure 60.

$$\text{absorption} = 100 - \text{reflection} - \text{transmission} \quad \text{Eqn 12}$$

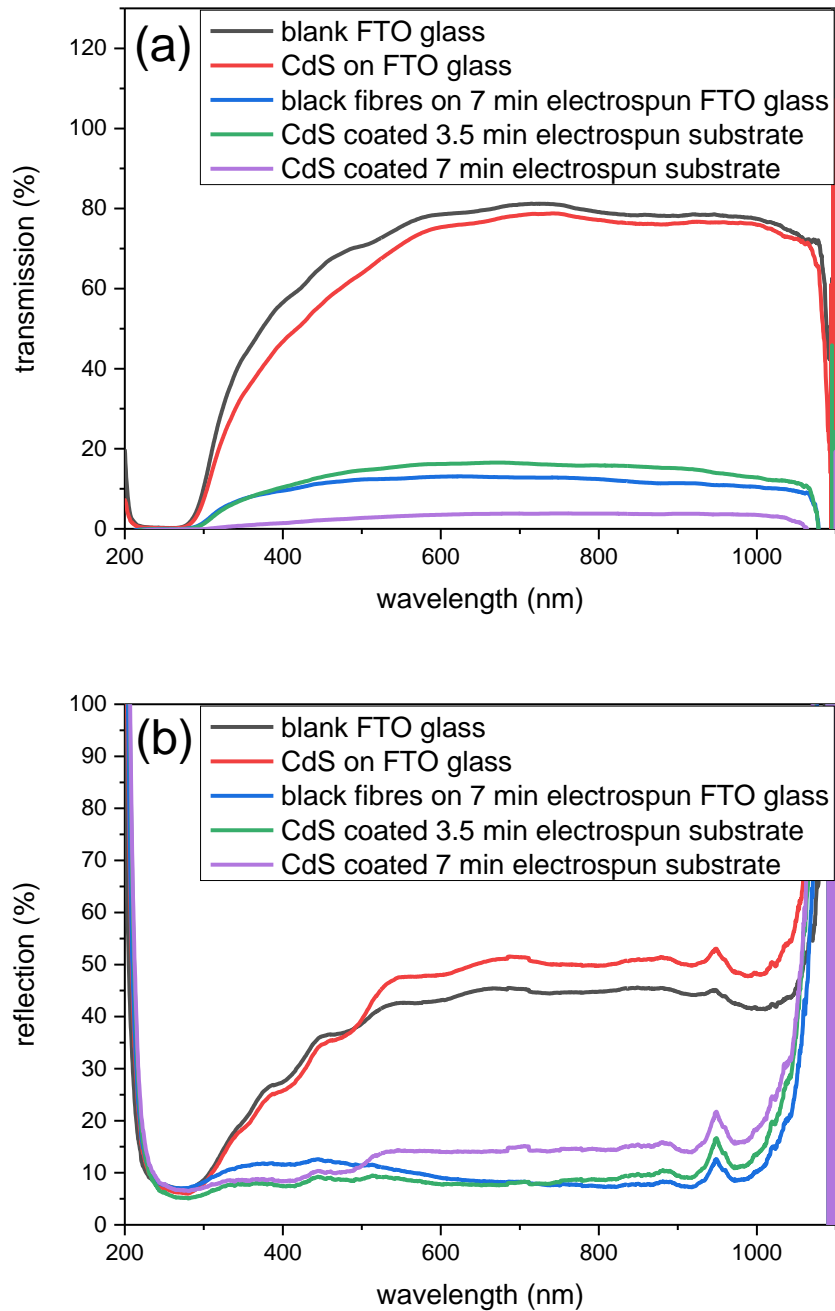


Figure 59 UV-visible measurement of (a) transmission and (b) reflection.

In this absorption spectrum, the CdS-coated samples show enhanced light absorption in a range from 300 nm to 700 nm which covers the UV and visible light range. Also, the fibre-covered sample shows extremely high light absorption.

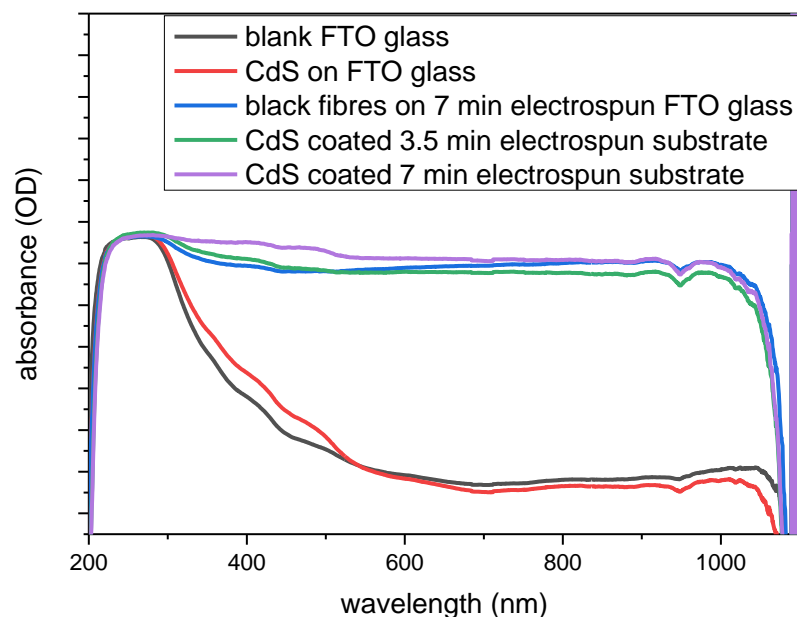


Figure 60 Calculated UV-visible absorption spectrum.

4.3.4 Photoelectrochemistry

Photoelectrochemistry experiments were performed on different samples to check the improvement of photoactivity. The experiments were studied in an aqueous electrolyte of Na_2S (0.25 M)/ Na_2SO_3 (0.35 M) at pH 11. The electrodes were irradiated using an Xe lamp through a 420 nm band pass filter with an irradiance of ca. 100 mW cm^{-2} , approximating to 1 sun.

CdS-coated F-SnO₂ fibered FTO as well as pure FTO and fibered FTO electrodes were compared and are shown in Figure 61. The LSV experiments were running in the dark and shown that the current of CdS/fiber sample is higher than fibered FTO which in its turn is much better than pure FTO glass.

Due to the higher surface area, fibres cover the FTO glass and provide more of a reaction centre for oxidation by holes. Coating of CdS also improved the current due to its better conductivity.

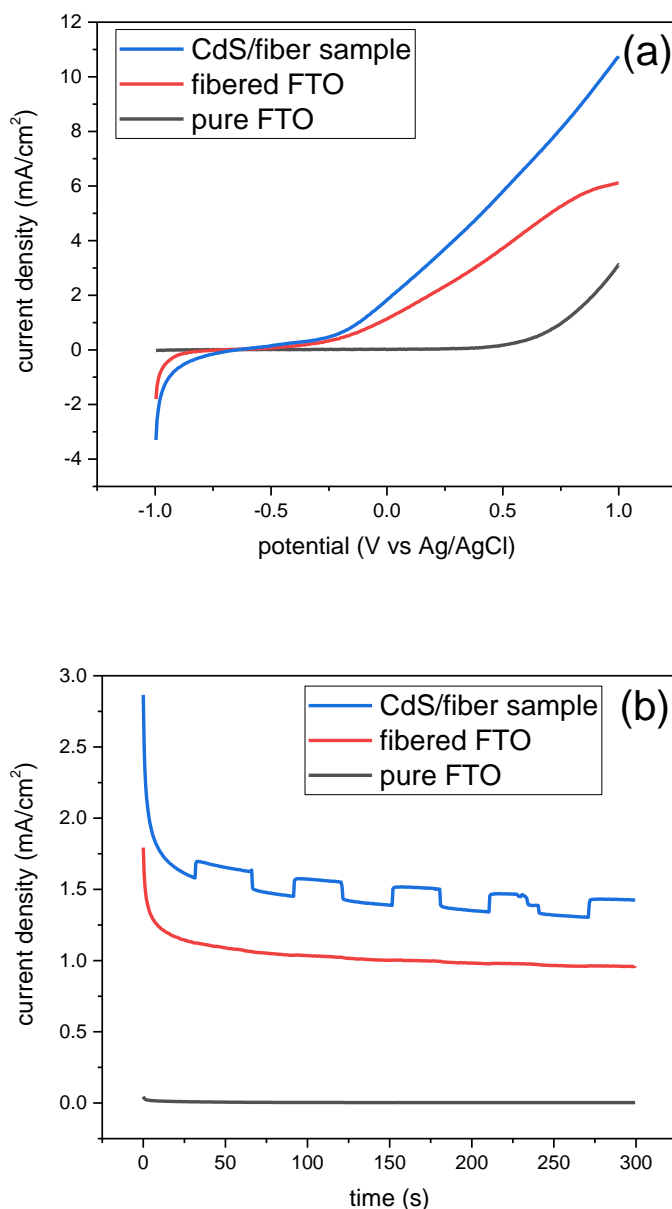


Figure 61 Test results of pure FTO, fibered FTO and CdS-coated fibered FTO. (a) Linear sweep voltammetry results in dark. (b) light/dark current switch test with 1 sun of Xe lamp through 420 nm band pass filter, 0 V vs Ag/AgCl (0.8 V vs RHE), Na₂S (0.25 M)/Na₂SO₃ (0.35 M) at pH 11.

Figure 61 (b) shows the light response of CdS-coated F-SnO₂ fibered FTO, pure FTO and fibered FTO electrodes irradiated with 1 sun of visible light under 0 V vs Ag/AgCl (0.8 V vs RHE) Na₂S (0.25 M)/Na₂SO₃ (0.35 M) (aq). The light was turned on and off every 30 seconds and no photocurrent is observed for both uncoated samples. For the CdS-coated fibre-covered FTO glass electrode, the photo current is about 0.15 mA/cm². For stability, both the fibre-covered samples retained the same photo current during the test, however, both of them showed a significant drop of dark current at the beginning of the test which may be owing to the low carrier mobility. The fibres may not have crystallized sufficiently. In the comparison experiment, high temperature calcination was applied. The film was burnt, leaving only a very fragile white film, easily removed by washing with water.

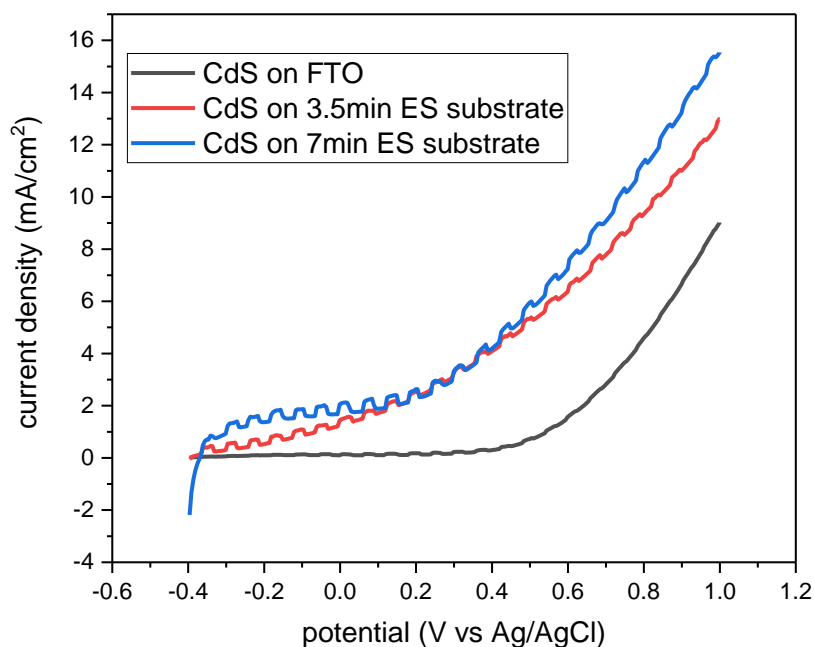


Figure 62 Linear sweep voltammetry results with light switch that shows light response of CdS coated samples on substrate of FTO, 3.5 minutes electrospun (ES) FTO and 7 minutes electrospun FTO glass.

Figure 62 shows the comparison of CdS-coated samples with different substrates. The electrospun F-SnO₂ film significantly improved the dark current compared to the sample with common FTO glass substrate. The sample of 7 minutes electrospun film showed slightly higher dark current than the 3.5 hr electrospun sample. However, the difference is less than double. For photo current, the “7 minute” sample (0.4 mA/cm²) also performed higher than the “3.5 minute” sample (0.23 mA/cm²), with a difference close to double. Based on the results we can estimate that the F-SnO₂ electrospun fibre layer was the main cause of improved dark current, whilst the CdS coating corresponded on the whole to the enhancement of photo current. As a result, we may assume that by loading more CdS on the substrate, the photo current could be further improved until a threshold value.

4.3.5 Fe₂O₃ decorated F-SnO₂ nanofiber photoelectrode

Electrospun F-SnO₂ nanofiber-covered FTO glass was also used as the substrate to grow Fe₂O₃ nanotubes for photoelectrodes.

Hematite is grown using a hydrothermal method. The prepared electrospun fibre FTO glass was placed in the autoclave, leaning on the wall with the fibered side down, with 14mL 0.15M FeCl₃ aqueous solution. The hydrothermal experiment ran at 100°C for 6 hours. After cooling to room temperature the

electrode was taken out and cleaned gently using Millipore water and drying under nitrogen flow. The electrode was then heated at 500°C for 2 hours and 800°C for 30 minutes and the hematite-coated fibre electrode was obtained.

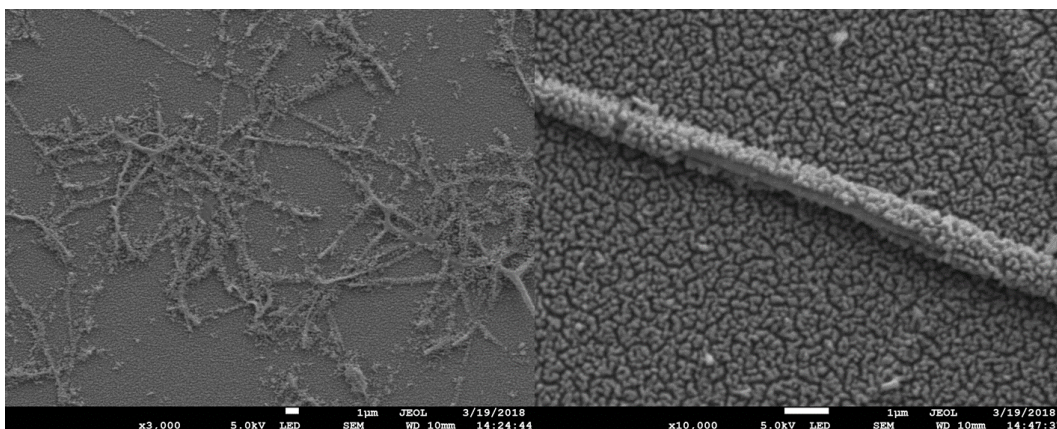


Figure 63 SEM and HRSEM images of Fe_2O_3 coated fibered FTO electrode.

Figure 63 shows the SEM images of Fe_2O_3 -coated fibered FTO photoelectrode. It is quite different from the Fibered FTO photoelectrode before Fe_2O_3 coating as shown in Figure 56 (a). There are fewer nanofibers on the surface than there were before coating. Although the fibres were totally covered with Fe_2O_3 nanotubes, the loading is not much higher than that on planar FTO glass. This is owing to the high temperature (800°C) during the hydrothermal process which makes the fibres unstable.

This instability is also related to the electrospinning time. The nanofibers were composed of small particles, which means that when applied long time electrospinning, a thicker nanofiber film covered the surface. This may have led to a change in structure after heating. In the previous experiment, due to the low temperature during the CdS-coating process, the carbon that remained acted as an adhesive, making the nanofibers solid. Because of this there was leeway for a small amount of deformation.

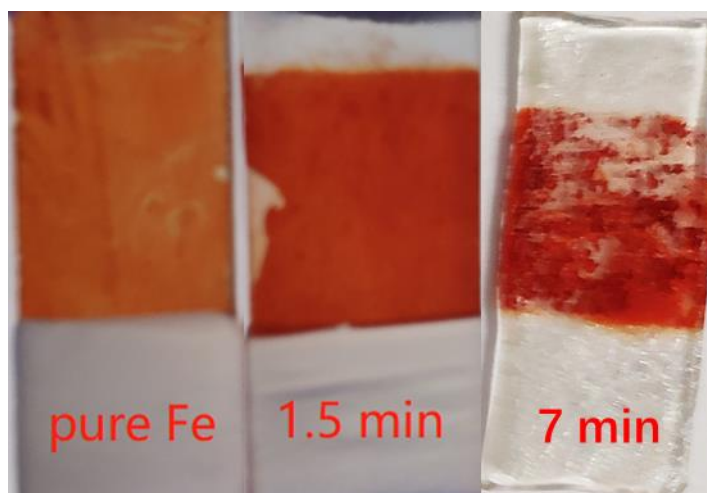


Figure 64 Photographs of Fe₂O₃ coated on pure FTO, 1.5 minute electrospun FTO and 7 minute electrospun FTO glass substrate.

Figure 64 shows the photographs of Fe₂O₃ coated on different substrates. The longer the electrospinning time, the darker the red colour of the Fe₂O₃. This is because the electrospun nanofibers provide a 3D structure on the surface which allows more loading of Fe₂O₃. However, the 7 minute electrospun sample shows cracked and incomplete coverage which is consistent with expectations. This broken film will certainly affect the photo performance in the photoelectrochemistry experiment.

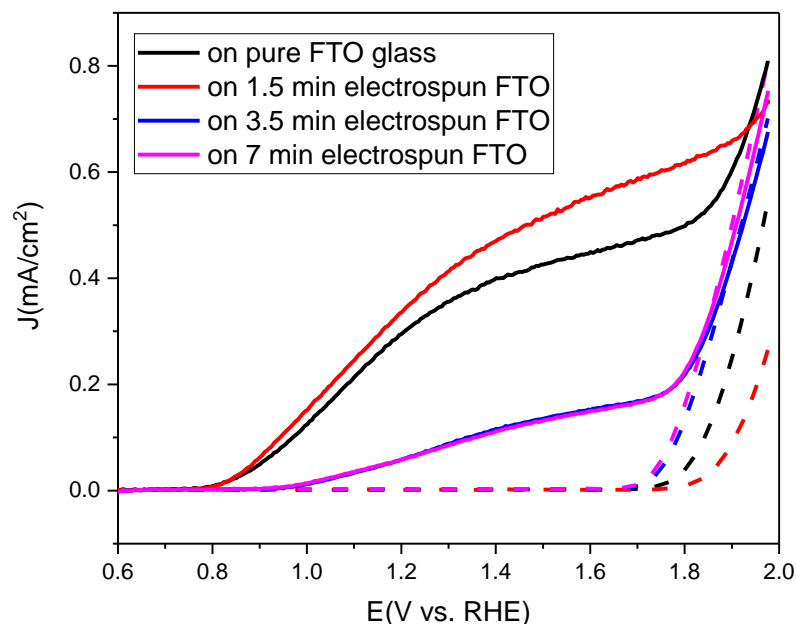


Figure 65 Linear sweep voltammetry results of Fe_2O_3 coated samples on different substrates. Solid lines are for results obtained under 1 sun light irradiation and the dash lines are for results got in the dark.

Figure 65 shows the LSV results of Fe_2O_3 coated samples on different substrates. The PEC experiments were performed under 1 sun of Xe lamp through 420 nm band pass filter, using an electrolyte of NaOH (0.1 M, aq). For same samples, results obtained under irradiation and in the dark are shown using solid line and dashed line, respectively. Compared to the “pure FTO” sample, the “1.5 min electrospun” sample was slightly improved (photocurrent at 1.23 V vs RHE was 0.3608 mA/cm² compared to 0.3164 mA/cm² for “pure FTO” sample). When the electrospinning time increased to 3.5 minutes, the photocurrent of the sample significantly dropped and only remained 65.2 $\mu\text{A}/\text{cm}^2$ at 1.23 V vs RHE. For the “7 min electrospun” sample, the photocurrent is almost the same as the “3.5 min electrospun” sample.

We can thus confirm that the high temperature treatment for these samples is a key factor. For samples with electrospinning time more than 3.5 minutes, the nanofiber film breaks and shows lower photocurrent than the “pure FTO” sample although the Fe_2O_3 nanotubes are still coated. However, for samples with short electrospinning time, for instance 1.5 minutes, the nanofiber structure remained intact after heating and could improve the photo properties due to the larger loading of Fe_2O_3 . This nanofiber structure could improve both the loading of the catalyst and the photo property of the electrode. However, this method should be avoided in higher temperature conditions. Even so, this method still has potential in the synthesis of high activity electrodes.

4.4 Conclusion

In this chapter, electrospinning was applied to prepare F-SnO₂ nanofiber film on FTO glass. This fibered substrate was conductive and high in surface area, and the crossed nanofibers formed a 3D structure which could be used as a framework for semiconductor coating. The fibered FTO substrate is black owing to the carbon which remained in the fibres during heating treatment. The substrate performed extremely high dark current in PEC experiment due to its conductivity and that there are more reaction centre on the surface.

CdS was coated on this fibered FTO substrate using SILAR method which is mild and easy to use. The CdS-coated sample looks yellowish and the UV-vis absorption calculated from the transmission and reflection spectra shows improved light absorption in the range from 300 nm to 700 nm, covering UV and visible light range. XRD spectra show no peaks of CdS in all samples except the CdS-coated 7 minute electrospun FTO electrode. The possible reason for

this is that the 7 minute electrospun substrate could load much more CdS on the electrode. PEC experiments on uncoated samples did not show any photocurrent, and the value of photo current is directly related to electrospinning time which is approximately equal to the loading of CdS.

Fe₂O₃ nanotubes were also coated onto fibered FTO substrate using the hydrothermal method. The results show that the electrospinning time affected the morphology of the film. When electrospinning time is more than 3.5 minutes, the film on the final sample is unstable and cracked, and the photocurrent is therefore decreased. However, when electrospinning time was applied in the correct range, for example 1.5 minutes, the film was to some extent stable and loaded more hematite nanotubes than that on pure FTO glass substrate, resulting in higher photocurrent.

The electrospun nanofiber-covered FTO glass substrate has a 3D structure and a high surface area, and could improve the photoactivity using appropriate methods. The limit of this method is the temperature: high temperature treatment will burn the carbon composition, reducing the stability of nanofibers and leading finally to fragile film. Nevertheless, this method still has potential in preparing high photoactivity photoelectrodes.

The aim of this chapter is to develop new substrates which could provide better photoactivity. The electrospinning method is simple and variable for different conditions. Electrospinning has many parameters that affect the final sample, which could be controlled and adjusted. However, it also means the electrospin process is easily affected by many aspects. By adjusting the parameters of the electrospin process, different semiconductors could be produced. Better

equipment would be necessary to have this measure of control and would solve many of the issues.

Chapter 5

Conclusions

5 Conclusions

5.1 Concluding Remarks

The aims of this project were to develop photoelectrodes with enhanced photo properties and investigate the effects of the different modifications and substrate materials. These aims have been demonstrated and studied, showing potential for improvements in photoelectrodes.

Several different substrate materials that have rarely been used in previous literature were prepared and tested. The amorphous material was thought to be poor in carrier mobility, and most of the photoelectrode materials were therefore crystalline. We proved that amorphous material could also be used to prepare photoelectrodes by proper design and modification. The Pb-Bi-Sn oxide amorphous photoelectrode was prepared in this project using mild and simple methods, and by doping, this amorphous material shows good photo properties which are better than some crystalline materials. However, it is still low in light absorption and carrier mobility, and more work is needed to study and improve it.

For electrodes of crystalline material (which is the type which has received most study) surface properties are most important as this is where the reactions take place. Unlike other research, we investigated a surface modification method to improve the photo properties of a hematite electrode. The modification only affects the surface state, which plays a key role in water oxidation. The final sample was still hematite with only trace amounts of modification metal ions on the surface. By this method, we successfully increased the photo current of the

hematite photoelectrode at 1.23 V vs RHE up to 77.6 % higher than the unmodified electrode. This provided a new direction in improving photoelectrodes. It is worth noting that there is no convenient and cheap method to obtain an accurate value of the modified metal ions absorbed on the surface of material. This makes modification difficult to precisely control.

A new substrate, not part of the main research direction, was studied and prepared in this project. Electrospinning was used to prepare nanofiber-covered FTO substrate. The nanofibers could keep stable after heating at the correct temperature and perform outstanding dark current. CdS and Fe₂O₃ were coated on this substrate for better photo property. The results show that the nanofibers improved the surface area and allowed more loading of semiconductors. When the fibres film remains complete, the nanofiber substrate could load more semiconductor and showed higher photocurrent than planar FTO glass. It also proved that the photo current is directly related to the load of coating semiconductor. It could be applied to any semiconductor which meets the requirements of this method, that is, low temperature. More research is still needed on how to make a solid framework.

In conclusion, we investigated several methods that could improve the properties of photoelectrodes. These methods are novel and rarely used or discussed in previous literature. We proved that, not only were they useful for improving photoelectrodes but they could be applied to any similar materials. Although they have some drawbacks, such as the low carrier mobility in amorphous material and the fragility of the 3D structure F-doped SnO₂ substrate, their special properties give them potential for more applications.

5.2 Future Direction

Photo electrochemistry is a low-cost and stable method to convert solar energy into chemical energy. We investigated some new ideas to prepare photo electrode with good photo properties. However, these results are not the end of the study. The method and samples could be improved in the future.

To be specific, (1) the amorphous material could be further improved. As the carrier mobility plays a key role in improving the photo properties, it could be further studied to discover the best doping modification method. On the other hand, the sample we prepared in this work showed a light colour. Attempts could be made to enhance the light absorbance so as to improve photo response. Light absorber materials could be helpful as dopant. (2) The Fe_2O_3 photo anode was improved using surface modification. In this experiment, we only controlled the dipping time and concentration of dipping solution. As the sample was directly taken out from solution and dried under nitrogen, there is no data on the quantity of solution and metal ion remaining on the surface. Due to the trace amount of the ions, it is hard to quantitatively analyse. This needs to be studied further. (3) The electrospun 3D structured substrate could load more catalyst due to the large surface area. However, this 3D structure is not as stable as other commercial electrode substrates. In this case, the electrode became fragile which might limit the application potential. Meanwhile, the electrospin method has a lot of adjustable parameters that can change the final sample.

In this project, we tried new materials, new modification methods and new substrates. All of these are novel with no previous experience. There is still the prospect of applying this research to other materials, for which there may be

Conclusions

commercial uses. It is hoped that these discoveries can be applied widely, and significantly contribute to PEC water splitting.

Chapter 6

Experimental

6 Experimental

6.1 Chemicals used

All the reagents and chemicals were used without any further purification unless stated otherwise.

Iron(III) 2-ethylhexanoate ($\text{Fe}(\text{EH})_3$, 50% w/w in mineral spirit, Alfa Aesar), Cobalt(II) 2-ethylhexanoate ($\text{Co}(\text{EH})_2$, 65% w/w in mineral spirit, Sigma-Aldrich Co Ltd), Lead(II) 2-ethylhexanoate ($\text{Pb}(\text{EH})_2$, 100%, Strem Chemicals, Inc.), Bismuth(III) 2-ethylhexanoate ($\text{Bi}(\text{EH})_3$, 92% w/w in ethylhexanoic acid, Alfa Aesar), Tin(II) 2-ethylhexanoate ($\text{Sn}(\text{EH})_2$, 95% w/w in mineral spirit, Sigma-Aldrich Co Ltd), Copper(II) 2-ethylhexanoate ($\text{Cu}(\text{EH})_2$, 100% powder, Sigma-Aldrich Co Ltd), Tungsten(VI) oxide (nanopowder, Aldrich Chem Co), 2-ethylhexanoate acid (Sigma-Aldrich Co Ltd) and Hexane (VWR Chemicals (BDH Prolabo)) were used.

Anhydrous iron chloride (FeCl_3), bis(trifluoromethane)sulfonimide metal salt ($\text{M}(\text{TFSI})_x$, $\text{M} = \text{Li, Na, K, Mg, Zn}$), acetonitrile (reagent grade), were purchased from Sigma Aldrich.

Tin (IV) chloride pentahydrate ($\text{SnCl}_4 \cdot 5\text{H}_2\text{O}$, 98%), ammonium fluoride (NH_4F , 98 %), polyvinylpyrrolidone (PVP, $\text{M}_w = 1,300,000$), ethanol (99%, reagent grade), N,N-Dimethylformamide (DMF, reagent grade), Cadmium acetate ($\text{Cd}(\text{CH}_2\text{COO})_2$ 99.99 %), sodium sulfide nonahydrate ($\text{Na}_2\text{S} \cdot 9\text{H}_2\text{O}$, 98 %) were purchased from Sigma Aldrich.

Fluorine doped tin oxide coated (FTO) glass used as substrate was from Sigma Aldrich (7 Ω /sq, 300 mm x 300 mm x 2 mm) and cut into 30 mm x 10 mm and 10 mm x 15 mm for different experiment, cleaned using acetone, ethanol and DI water, and was dried under nitrogen flow.

When preparing amorphous Pb-Bi-Sn oxide electrode, a round KBr disc with diameter of 25 mm was used as substrate to prepare films on and irradiated together with FTO glass for the FTIR experiment.

Where water been mentioned in any synthesis process in this project, it refers to Millipore water.

6.2 Techniques

6.2.1 Powder X-ray Diffraction (PXRD)

Wide angle PXRD patterns were recorded on a Bruker-AXS D8 Advance instrument with Lynx eye detector, using Cu K α radiation (1.54 Å) with a 1 mm slit on the source and 2.5 mm detector slit. Data was collected from 5-90 ° 2 θ , with 0.02 ° step size and a scan speed of 0.1 seconds per step. For most of the samples in this project which were prepared on FTO glass, the samples were put horizontally on a glass holder which will not show any peak on the detected XRD pattern.

XRD experiment is based on Bragg's law:

$$2d \sin\theta = n\lambda \quad \text{Eqn 13}$$

Here d is the spacing between lattice plane, θ is the incident angle, n is any integer and λ is the wavelength of the x ray beam.

6.2.2 Scanning electron microscopy (SEM)

SEM images were obtained using a FEI Sirion scanning electron microscope. Prior to imaging, samples were supported on an aluminium stub with an adhesive carbon tab and sputter coated with a 10 nm layer of carbon using an Agar auto carbon coater. For some samples with poor conductivity, such as amorphous materials, the coating process has to be longer to prevent the accumulation of electrons which will lead to “overexposure” on the surface and make it harder to get a clear image.

Energy Dispersive Analysis of X-rays (EDX) was performed using an attached EDAX Phoenix X-ray spectrometer. Scans were recorded at 10 kV accelerating voltage for 1 minute, over regions 50 μm by 35 μm in size. Elemental analyses of samples were averaged over at least 10 of these measurements. EDX on SEM equipment has low accuracy and could not provide reliable details from a very small region.

6.2.3 Transmission Electron Microscopy (TEM)

TEM images and electron diffraction patterns were obtained using a JEOL 2011 transmission electron microscope operated at 200 kV accelerating voltage. Dark field imaging and HAADF STEM imaging/EDX mapping were performed at the University of Leeds on a Tecnai TF20 FEGTEM operated at 200 kV. CCD images were extracted using Gatan Digital Micrograph software. Particle size distributions of nanoparticles were evaluated by averaging the diameter of >100 particles from TEM images.

Prior to analysis, solid samples for TEM imaging were ground in methanol and sonicated for 15 minutes to disperse. One drop of the dispersion was deposited onto 3 mm holey carbon coated copper grids and allowed to dry in air. FTO film samples were scraped off the slide, then ground in methanol/sonicated as above. For ligand stabilised nanoparticle dispersions in organic solvents, TEM samples were prepared by evaporation of a single drop of diluted solution onto a holey carbon copper grid.

6.2.4 UV-vis absorption, reflection and transmission spectroscopy

UV-Visible absorption, transmission and reflectance spectra were recorded on an Ocean Optics HR2000+ High Resolution Spectrometer with DH-2000-BAL Deuterium/Helium light source (200 – 1100 nm). An R400-7-UV-Vis reflection probe was used to record diffuse reflectance spectra. Powder samples were

deposited as a flat layer between two pyrex or quartz slides and placed beneath the reflection probe. Spectra were recorded using Spectra Suite software from an average of 10 scans, an integration time of 20 seconds and box car smoothing width of 20 nm. Solution UV-Visible absorption spectra were recorded with the same light source, in quartz cuvettes using a solution cell.

6.2.5 Fourier-transform infrared spectroscopy (FTIR)

Fourier Transform infrared spectroscopy (FTIR) was performed on a Thermo Nicolet AVATAR 370 FT-IR spectrometer. Spectra were recorded from 1000 to 4000 cm^{-1} over an average of 32 scans.

For amorphous photoelectrodes, a KBr disc was used to prepare film on it for FTIR measurement.

Powdered materials were deposited on the diamond surface. The pressure arm was tightened onto the sample until the force gauge displayed 100 N.

6.2.6 X-ray fluorescence (XRF) measurement

X-ray fluorescence (XRF) was performed on an XGT-7000V x-ray fluorescence (XRF) microscope (HORIBA scientific). For all electrode samples, there are two ways to take XRF experiments. The electrode could be put directly on to the

holder for measurement. In this way, distribution of elements on the surface could be detected. Another way is scraping the film off the electrode and detect this powder. In this way, accurate details of sample could be obtained in the measurement.

6.2.7 Photoelectrochemical measurement

6.2.7.1 Photoelectrochemistry experiments

Electrochemistry experiments were performed in a three-necked flask. 0.1M NaOH(aq) was used as the electrolyte solution in most experiments, while an aqueous electrolyte of Na₂S (0.25 M)/Na₂SO₃ (0.35 M) at pH 11 was used for CdS-coated samples. The Ag/AgCl reference electrode and platinum wire/mesh counter electrode were placed in the side-necks and the sample was placed in the centre neck of the flask as the working electrode. An Xe lamp through 1 420 nm band pass filter with an irradiance of 1 sun was used as light source. The potential is calculated using the following equation.

$$E_{RHE} = E_{Ag/AgCl} + 0.21V + 0.059 \times pH \quad \text{Eqn 14}$$

A Bio-Logic SAS SP-150 potentiostat was used to collect data. Cyclic voltammetry (CV) was obtained at a scan rate of 10 mV/s. Linear sweep voltammetry (LSV) was obtained at a scan rate of 10mV/s. Tafel data was performed using controlled potential electrolysis (CPE) mode (10 mV step, 1-

minute period, bias potential is 800 mV). The stability experiment was performed using Chronoamperometry mode (10 mV step, 30 minutes period, bias potential is 800 mV or 253mV).

6.2.7.2 Incident photon-to-current efficiency (IPCE) measurements

Incident photon-to-current efficiency (IPCE) were carried out in a quartz cell with a Ag/AgCl (sat. NaCl) reference electrode and platinum wire counter electrode. Samples were placed in the cell as the working electrode and illuminated with monochromated light with a slit width of 20nm. An International Light Technologies 1400-a Radiometer Photometer was used to measure lamp power. The equation of IPCE is as follows²⁰⁰:

$$\text{IPCE} = \frac{hcJ_{\lambda}}{\lambda W_{\lambda}} \quad \text{Eqn 15}$$

Where h is the Planck's constant, c the velocity of light, J_{λ} the photocurrent density, λ the wavelength and W_{λ} is the power of the monochromatic light flux.

6.2.7.3 Mott-Schottky measurement

Mott-Schottky plots were performed in the dark at 100 Hz frequency.

From Mott-Schottky, donor density and flatband potential could be obtained. The space charge capacitance (C_s) could be described by the Mott-Schottky equation:

$$\left(\frac{A}{C_s}\right)^2 = \frac{2}{\epsilon\epsilon_0qN_D}\left(E - E_{fb} - \frac{k_B T}{q}\right) \quad \text{Eqn 16}$$

Where the A is the area of electrode which is 1 cm^2 in the experiments, ϵ is the dielectric of semiconductor (14.2 for the Fe_2O_3), ϵ_0 is the vacuum permittivity ($8.854 \text{ E}^{-12} \text{ C/Vm}$), q is elementary charge, N_D is the donor density, E_{fb} is the flatband potential, k_B is Boltzmann's constant and T is absolute temperature. In Mott-Schottky plots, C_s^{-2} and E are y axis and x axis, thus the N_D could be obtained as following:

$$N_D = \frac{2}{\epsilon\epsilon_0qA^2(\text{slope})} \quad \text{Eqn 17}$$

6.2.7.4 Electrochemical Impedance Spectroscopy (EIS)

Potential Electrochemical Impedance Spectroscopy (EIS) was measured at different potentials with the frequency ranging from 500 kHz to 100 mHz under 1 sun light. The parameters analysis of EIS data was performed using Bio-Logic EC-Lab software V11.10.

The proposed structure of a working electrode is shown in Figure 66. The electrode could be thought of as three different layers, FTO layer, Fe_2O_3 bulk layer and surface and depletion layer. Considering the importance of surface

defect, we assume the model as shown in Figure 67. Here R1 is system resistance, Q1 and R2 is capacitance and resistance of the bulk semiconductor, Q3 and R3 is capacitance and resistance of the electrode surface and the interface between the electrode and the solution. All the EIS data were analyzed using this model and obtained separate parameter figures.

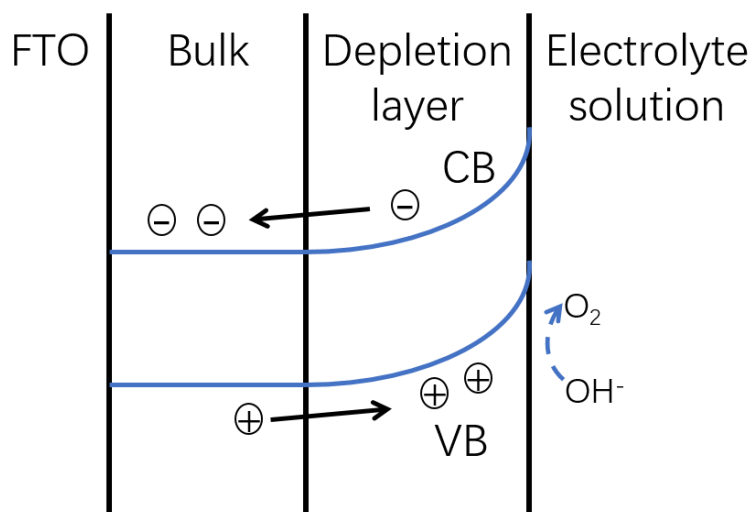


Figure 66 Proposed structure of a working electrode.

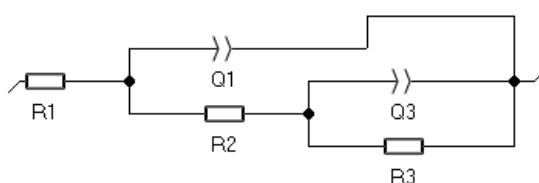


Figure 67 Scheme of module used to analyze the EIS data.

6.3 Synthetic methods

6.3.1 Synthesis of Pb-Bi-Sn oxides amorphous films on FTO glass

The method is based on previous work used to prepare amorphous films of Fe, Ni and Co oxides⁷¹. Typically, the metal 2-ethylhexanoate salts were used as the metal source and dissolved in hexane to form a precursor solution of 7.5 % w/w. The concentration affects the viscosity. A precursor of higher viscosity will be harder to spread homogenously in the spin-coating process, whilst a low viscosity will make the precursor easier to be thrown off the sample.

The precursor solution would change colour after several days, so generally, it was prepared and used within that time.

10 μL of precursor solution was dropped on the substrate, followed by spin-coating at the rate of 3000 rpm for 1 minute. After that the precursor formed an homogenous film on the substrate. The obtained substrate with precursor was irradiated under UV light (254 nm, 11 w) to decompose the organic acid group, followed by heat treatment under 100°C for 1 hour. Then the amorphous metal oxide film was obtained and ready for the next layer if necessary. Each layer was prepared using the same method.

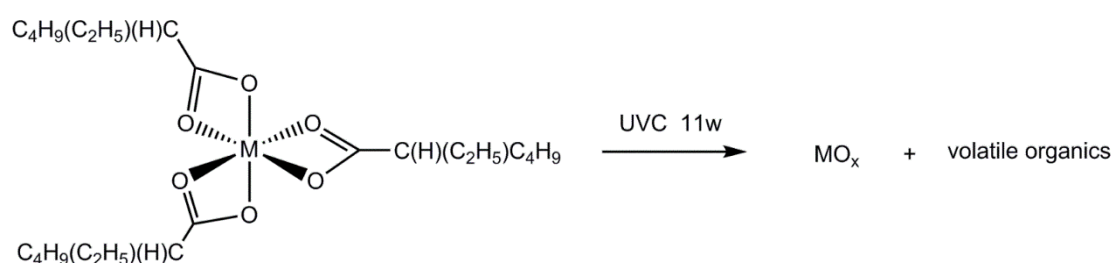


Figure 68 Reaction of decomposing ethylhexanoate (EH) metal salt to amorphous metal oxide.

This method is photochemical metal-organic deposition (PMOD)^{68, 70, 72, 128}. The sources of metal oxide are some organic acid metal salts, and these are easily degraded under UV light. The organic acid group used in this project is ethylhexanoate (EH) and the degradation reaction formula is shown below.

The metal salt could be dissolved in solution and then formed homogenous thin transparent film on FTO glass or similar substrate. Different solutes are mixed well to make sure that the ratio of elements in the final film are the same throughout. Then the precursor film samples were placed under UV light (254 nm, 11 w) for several hours. After irradiation, the samples were heated in the oven under 100°C for an hour.

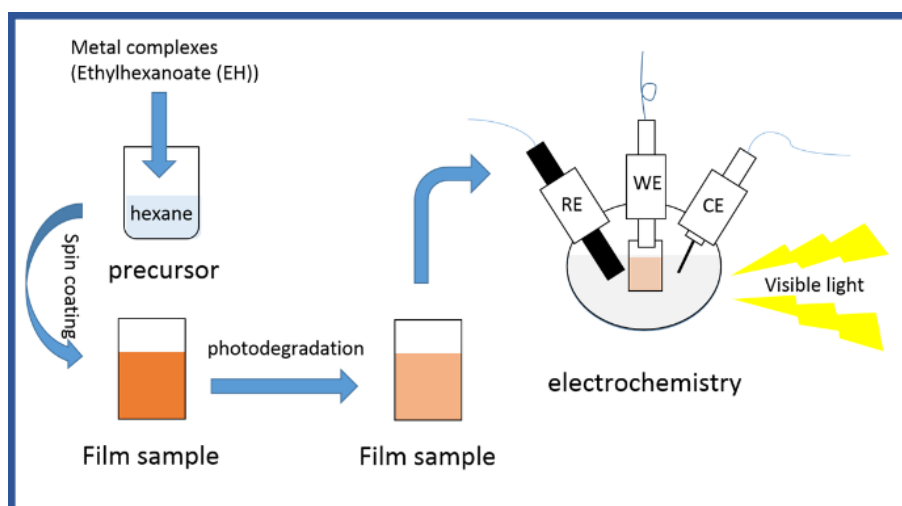


Figure 69 The schematic drawing that illustrates the experiment processing steps. The precursor was spin coated onto FTO glass to form a film sample as a working electrode (WE). The electrochemical experiment was performed in a three-electrode cell using 0.1 M NaOH (aq) as the electrolyte solution. A platinum wire was used as the counter electrode (CE). An Ag/AgCl (sat. NaCl) reference electrode (RE) was separated from electrolyte solution with a glass protector.

6.3.2 Synthesis of Pb-Bi-Sn oxide on KBr disc for FTIR

FTIR was used to confirm the decomposition of the organic groups. As the FTO glass substrate is not suitable to put directly in the FTIR equipment, an alternative choice is preparing same samples on KBr disc which is specific to the FTIR experiments.

As per preparing samples on FTO glass, the precursor solution was dropped on a KBr disc (radius of 1cm) for spin-coating and then irradiated under UV light (254 nm, 11 w). During the irradiation, FTIR experiments, are performed on the KBr disc every 3 hours until the vibration peaks of 2-ethylhexanoate ligand had disappeared.

6.3.3 Doping the amorphous electrode with Fe, Co and Cu dopant

The method of doping with Fe, Co and Cu is the same as the preparation of PbBiSn films. A certain amount of Fe, Co or Cu 2-ethylhexanoate salts was mixed in precursor solution of the Pb-Bi-Sn system. Then the mixed solution was stirred for 2 hours to ensure it was well-mixed and the dopant element was the same throughout.

The mixed solution was dropped on substrate and spin-coated for 60 seconds at 3000 rpm. After that the substrate was irradiated under UV light for several hours and then heated at 100°C to obtain the final sample.

6.3.4 Doping the amorphous electrode with WO₃ nanoparticles

Unlike from doping Fe, Co and Cu dopant, the WO₃ nanoparticles were not dissolved in the precursor. Hexane and 2-ethylhexanoate acid were mixed in a beaker and then WO₃ nanoparticles were dispersed in the mixture. The beaker with WO₃ dispersion was ultrasonicated for two hours to make sure the nanoparticles were totally dispersed and would not coagulated immediately. Typically, the weight ratio of WO₃, hexane and 2-ethylhexanoate acid is 3mg:200mg:400mg. This WO₃ precursor was mixed with Pb-Bi-Sn precursor under strong stirring to obtain WO₃ solution.

The solution was dropped on substrate and spin-coated for 60 seconds at 3000 rpm. Then this substrate was irradiated under UV light followed by heat treatment at 100°C to obtain the final sample.

6.3.5 Electrodeposition of Co-Pi on amorphous electrode

Following previous literature²⁰¹, Co-Pi was electrodeposited on amorphous Pb-Bi-Sn-oxide film in a three-electrode cell, using Ag/AgCl as the reference electrode and a Pt mesh as counter electrode. As the working electrode, the Pb-Bi-Sn oxide/ FTO electrode was submerged in a solution of 0.5 mM cobalt nitrate in 0.1 M pH 7 potassium phosphate (KPi) buffer. Typically, Co-Pi was electrodeposited at 900mV vs Ag/AgCl for 350 seconds. After deposition of Co-Pi, the sample remained red and no obvious change of colour was observed.

6.3.6 Preparing layer-by-layer amorphous films on FTO glass

This method is the same as the preparation of amorphous Pb-Bi-Sn oxide film. The metal 2-ethylhexanoate salts were separately used as metal sources and dissolved in hexane to form different solutions of 7.5 w%. 10 μ L of the precursor solution, which was planned to form the film at bottom, was dropped on the substrate before spin-coating at rate of 3000 rpm for 1 minute. The obtained substrate with precursor was irradiated under UV light (254 nm, 11 w) to decompose the organic acid group, followed by heat treatment under 100°C for 1 hour. In this way the first layer of amorphous metal oxide film was obtained and was ready for a second layer. By repeating the same process with precursor solutions of different metal salts, the other layers were prepared one by one. Finally, layer-by-layer amorphous metal film sample was obtained as planned. It was noticeable that the second layer of film need more irradiation time under UV light to ensure the decomposition of the organic group. Similarly, the third layer needed to be irradiated for more time than the second layer.

6.3.7 Synthesis of iron oxide slide

FTO glass (Sigma-Aldrich, L * W * D 300 mm * 300 mm * 2 mm) was cut into 30mm*10mm size slides. The FTO slide was successively cleaned in ethanol, acetone and water using ultrasonic cleaning machine and drying under nitrogen flow.

The cleaned FTO slide was partially covered using Teflon tape, leaving a 10mm*10mm window on the conductive side. With the conductive side facing downward, the FTO slide was leaned in the autoclave. The volume of autoclave was 20 mL and filled with about 70 % volume of 0.15 M FeCl_3 aqueous solution (14 mL). The hydrothermal experiment ran at 100°C for 6 hours with a ramp rate of 5 °C/min, and natural cooling to room temperature, then cleaned gently using Millipore water and drying under nitrogen flow. This precursor slide was then calcined at 500°C for 2 hours and 800°C for 30 minutes, and the iron oxide slide was obtained. The electrode is dark red which is typical of the colour of hematite film.

6.3.8 Synthesis of metal-modified iron oxide electrode

Bis(trifluoromethane)sulfonimide metal salt ($\text{M}(\text{TFSI})_x$ ($\text{M}=\text{Li}, \text{Na}, \text{K}, \text{Mg}, \text{Zn}$)) was dissolved in acetonitrile to form 5mM solution, and 2 mL of this solution was filled in a glass vials of 8 mL. An iron oxide slide was dipped into the glass vial with metal solution and the vials were placed horizontally on the lab bench to make sure the conductive side of the electrode was immersed in solution. After dipping for 30 seconds, the electrode was taken out and dried under nitrogen flow. 30 seconds is enough for metal ions adsorbed on the surface of hematite film. Comparison experiments showed that more dipping time did not improve the photocurrent considering the deviation. The electrode was then calcined for 1 hour at 450°C, which completed the synthesis of the metal modified iron oxide electrode.

6.3.9 Synthesis of F-SnO₂ nanofiber film on FTO glass

F-SnO₂ nanofiber-covered FTO glass was prepared through electrospinning. In a typical experiment, 1.4 g of SnCl₄·5H₂O (4 mmol), 0.8 g of Polyvinylpyrrolidone (PVP), 6.89 g of ethanol and 2.3 g N,N-Dimethylformamide (DMF) was mixed and stirred for 5 hours to form a transparent and homogenous solution. In this recipe, the PVP was the main component of the electrospinning nanofibers and affected the thickness and strength of the fibers. By contrast, the SnCl₄·5H₂O is the main part of the nanofibers after calcination. The ratio between PVP and SnCl₄·5H₂O was adjusted so that the fibres would not be hollow and crisp after calcination. The DMF and ethanol affect the electrospinning process so that the fibers are continuous. The obtained nanofiber electrode was added with 143.1 μL of saturated NH₄F solution (45 g in 100 mL under standard conditions) and magnetic stirred for one more hour to obtain the final precursor. This precursor is white due to formation of particles from hydrolysis of SnCl₄ and had to be used immediately to avoid coagulation. The atomic ratio between F and Sn was 0.5, which is the best ratio for FTO formation, as proved in previous work.

This solution was electrospun into nanofibers onto a 10 mm* 30 mm FTO glass. The FTO glass was placed on a grounded aluminium foil, and FTO glass was fixed with the conductive side upward, and connected to the foil with copper tape, ensuring the FTO glass was also grounded. In electrospinning, the precursor solution was placed in a 5 mL syringe with a needle of 0.514 mm inter diameter, and a DC power supply was used to apply a high voltage of 10 kV over a 6 cm gap between the spinneret and collector. The collector was heated to 100°C during the electrospinning to improve the solvent evaporation. A

peristaltic pump was used to deliver the solution at a flow rate of 0.05 mL min^{-1} . After 7 minutes of spinning, the FTO glass was covered with white mat film and then heated at 450°C for 2 hours at a rate of 1°C/min . After heating, the fiber film became black and stable on the FTO glass.

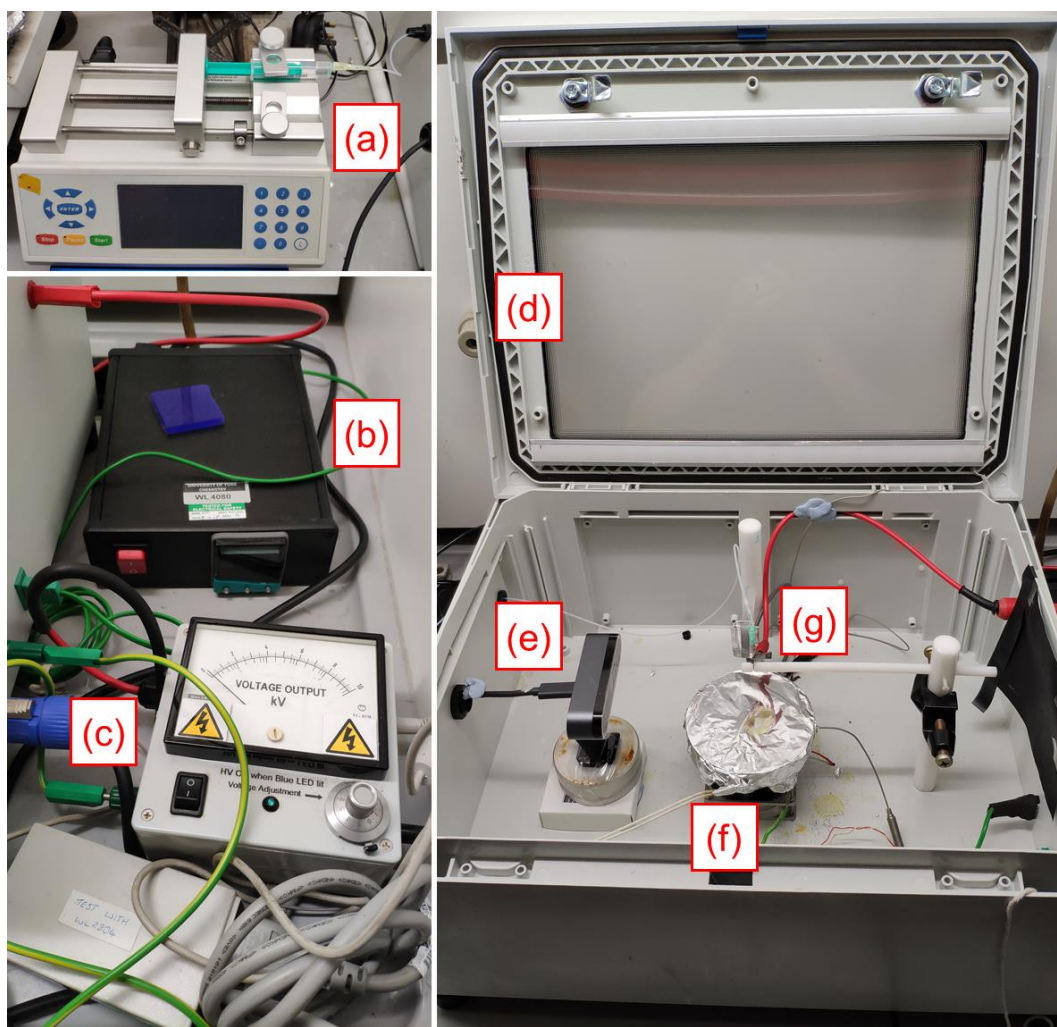


Figure 70 Scheme of electrospinning experiments. (a) peristaltic pump, (b) temperature controller for collector heating, (c) DC power supply, (d) electrospinning box with an observation window, (e) digital camera, (f) metal collector and (g) needle of syringe.

Other ratios of precursor and temperature have been tried for comparison as these samples remained white after the last process and the films were fragile

and not firm on the FTO glass substrate. The black film was estimated to have the best parameters owing to its carbon content.

6.3.10 Decorating CdS on F-SnO₂ nanofiber photoelectrode and pure FTO glass

To obtain better photoactivity, CdS was coated on F-SnO₂ nanofibers using the SILAR method.¹⁹⁹ SILAR is simple and controllable, and will mildly coat semiconductor onto a substrate. Cd(Ac)₂ was solved in ethanol to form cadmium (Cd) solution (50 mM) and an 8 mL glass vial filled with 3 mL. Meanwhile, 3 mL of Na₂S aqueous solution (50 mM) was prepared as sulphur (S) solution and placed in another glass vial.

The prepared F-SnO₂ nanofiber electrode was stood vertically in the glass vial of Cd solution for 1 minute and then dried under flow of N₂. After completely dried, the electrode was again placed vertically in another glass vial of S solution for 1 minute and dried again under N₂. This process was repeated for 8 times and then the electrode was heated under argon at 400°C for 30 minutes with a ramp rate of 1 °C/min. After cooling to room temperature, the CdS coated F-SnO₂ nanofiber photoelectrode was obtained which is of a yellow colour. During the process, the Cd²⁺ and S²⁻ ions were reacted on the surface of fibres and became stable CdS particles after heating treatment.

As a comparison, CdS was prepared using the same method, by coating on a pure FTO glass as well.

6.3.11 Growing Fe₂O₃ nanotubes on F-SnO₂ nanofiber photoelectrode and pure FTO glass

The growing of hematite is performed by using a hydrothermal method similar to the method described in chapter 6.3.7. The prepared F-SnO₂ nanofiber electrode was placed in the autoclave with 14mL 0.15M FeCl₃ aqueous solution. The nanofiber electrode was leant against the wall with the conductive fibered side downward.

The hydrothermal experiment ran at 100°C for 6 hours with a ramp rate of 5 °C/min. After cooling to room temperature, the electrode was taken out and cleaned gently using Millipore water and drying under nitrogen flow. Then the electrode was heated at 500°C for 2 hours and 800°C for 30 minutes to obtain the hematite-coated fibers electrode.

Abbreviations

Ac – Acetate

aq – Aqueous

CB – Conduction Band

CE – Counter Electrode

CPE – Controlled Potential Electrolysis

CV – Cyclic Voltammetry

CVD – Chemical Vapour Deposition

DC power – Direct Current Power

DMF – N,N-Dimethylformamide

DRUVS – Diffuse Reflectance UV-Visible Spectroscopy

EDX – Energy Dispersive X-ray Analysis

EH – 2-Ethylhexanoate

EIS – Electrochemical Impedance Spectroscopy

FTO – Fluorine Doped Tin Oxide

HRSEM – High Resolution Scanning Electron Microscopy

IPCE – Incident Photon to Current Conversion Efficiency

FTIR – Fourier Transform Infrared

ITO – Indium Doped Tin Oxide

LSV – Linear Sweep Voltammetry

Mesoporous – 2 to 50 nm

NHE – Normal Hydrogen Electrode

NP – Nanoparticles

P25 – 80 : 20 mixture of Anatase : Rutile TiO₂

PEC – Photoelectrochemistry

PVP – Polyvinylpyrrolidone

PXRD – Powder X-ray Diffraction

QD – Quantum Dot

QE – Quantum Efficiency

RE – Reference Electrode

RHE – Reversible Hydrogen Electrode

sat – Saturated

SEM – Scanning Electron Microscopy

SILAR – Successive Ionic Layer Adsorption and Reaction

STEM – Scanning Transmission Electron Microscope

TCO – Transparent Conductive Oxide

TEM – Transmission Electron Microscopy

TFSI – Bis(trifluoromethane)sulfonimide

UV – Ultraviolet Light

UV-vis – Ultraviolet and Visible light

VB – Valence Band

WE – Working Electrode

wt% – Weight Percentage of Nanoparticles as a Ratio to the Support Mass

XRD – X-ray Diffraction

XRF – X-ray Fluorescence

List of references

1. Global energy data, <https://www.iea.org/statistics/?country=WORLD&year=2015&category=Key%20indicators&indicator=TPESbySource&mode=chart&categoryBrowse=false>, (accessed 10th, August, 2018).
2. A. Fujishima and K. Honda, *Nature*, 1972, **238**, 37.
3. S. U. Khan, M. Al-Shahry and W. B. Ingler, Jr., *Science*, 2002, **297**, 2243.
4. R. Abe, K. Sayama and H. Arakawa, *Chemical Physics Letters*, 2003, **371**, 360.
5. G. Wang, H. Wang, Y. Ling, Y. Tang, X. Yang, R. C. Fitzmorris, C. Wang, J. Z. Zhang and Y. Li, *Nano Letters*, 2011, **11**, 3026.
6. M. Ni, M. K. H. Leung, D. Y. C. Leung and K. Sumathy, *Renewable and Sustainable Energy Reviews*, 2007, **11**, 401.
7. J. R. Swierk, K. P. Regan, J. Jiang, G. W. Brudvig and C. A. Schmuttenmaer, *ACS Energy Letters*, 2016, **1**, 603.
8. M. Ge, Q. Li, C. Cao, J. Huang, S. Li, S. Zhang, Z. Chen, K. Zhang, S. S. Al-Deyab and Y. Lai, *Advanced science*, 2017, **4**, 1600152.
9. K. R. Reyes-Gil, E. A. Reyes-García and D. Raftery, *The Journal of Physical Chemistry C*, 2007, **111**, 14579.
10. M. Meng, X. Wu, X. Zhu, X. Zhu and P. K. Chu, *ACS Applied Materials & Interfaces*, 2014, **6**, 4081.
11. K. R. Reyes-Gil, Y. Sun, E. Reyes-García and D. Raftery, *The Journal of Physical Chemistry C*, 2009, **113**, 12558.
12. J. G. Mavroides, J. A. Kafalas and D. F. Kolesar, *Applied Physics Letters*, 1976, **28**, 241.
13. K. Sayama and H. Arakawa, *The Journal of Physical Chemistry*, 1993, **97**, 531.
14. V. R. Reddy, D. W. Hwang and J. S. J. K. J. o. C. E. Lee, *Korean Journal of Chemical Engineering*, 2003, **20**, 1026.
15. H. M. Chen, C. K. Chen, Y.-C. Chang, C.-W. Tsai, R.-S. Liu, S.-F. Hu, W.-S. Chang and K.-H. Chen, *Angewandte Chemie*, 2010, **122**, 6102.
16. A. Wolcott, W. A. Smith, T. R. Kuykendall, Y. Zhao and J. Z. Zhang, *Advanced Functional Materials*, 2009, **19**, 1849.
17. X. Yang, A. Wolcott, G. Wang, A. Sobo, R. C. Fitzmorris, F. Qian, J. Z. Zhang and Y. Li, *Nano Letters*, 2009, **9**, 2331.
18. X. Zhang, Y. Liu and Z. Kang, *ACS Applied Materials & Interfaces*, 2014, **6**, 4480.
19. M. Shao, F. Ning, M. Wei, D. G. Evans and X. Duan, *Advanced Functional Materials*, 2014, **24**, 580.
20. W. Yuefan, K. Lin, K. Junhua, L. Hong, J. Zhihui, L. Xuehong, D. Hejun and S. Xiao Wei, *Nanotechnology*, 2012, **23**, 235401.

21. J. Li and N. Wu, *Catalysis Science & Technology*, 2015, **5**, 1360.
22. H. Tang, K. Prasad, R. Sanjinès, P. E. Schmid and F. Lévy, *Journal of Applied Physics*, 1994, **75**, 2042.
23. Q. Fu, *Radiation (solar)*, Academic Press, Amsterdam, 2002.
24. S. Tokunaga, H. Kato and A. Kudo, *Chemistry of Materials*, 2001, **13**, 4624.
25. S. J. Hong, S. Lee, J. S. Jang and J. S. Lee, *Energy & Environmental Science*, 2011, **4**, 1781.
26. S. M. Thalluri, S. Hernández, S. Bensaid, G. Saracco and N. Russo, *Applied Catalysis B: Environmental*, 2016, **180**, 630.
27. Y. Li, T. Jing, Y. Liu, B. Huang, Y. Dai, X. Zhang, X. Qin and M.-H. Whangbo, *ChemPlusChem*, 2015, **80**, 1113.
28. A. Iwase, S. Ikeda and A. Kudo, *Chemistry Letters*, 2017, **46**, 651.
29. H. J. Kong, D. H. Won, J. Kim and S. I. Woo, *Chemistry of Materials*, 2016, **28**, 1318.
30. S. Y. Chae, C. S. Lee, H. Jung, O.-S. Joo, B. K. Min, J. H. Kim and Y. J. Hwang, *ACS Applied Materials & Interfaces*, 2017, **9**, 19780.
31. X. Chang, T. Wang, P. Zhang, J. Zhang, A. Li and J. Gong, *Journal of the American Chemical Society*, 2015, **137**, 8356.
32. M. G. Lee, D. H. Kim, W. Sohn, C. W. Moon, H. Park, S. Lee and H. W. Jang, *Nano Energy*, 2016, **28**, 250.
33. H. Jung, S. Y. Chae, C. Shin, B. K. Min, O.-S. Joo and Y. J. Hwang, *ACS Applied Materials & Interfaces*, 2015, **7**, 5788.
34. M. Zhong, T. Hisatomi, Y. Kuang, J. Zhao, M. Liu, A. Iwase, Q. Jia, H. Nishiyama, T. Minegishi, M. Nakabayashi, N. Shibata, R. Niishiro, C. Katayama, H. Shibano, M. Katayama, A. Kudo, T. Yamada and K. Domen, *Journal of the American Chemical Society*, 2015, **137**, 5053.
35. Y. Ma, A. Kafizas, S. R. Pendlebury, F. Le Formal and J. R. Durrant, *Advanced Functional Materials*, 2016, **26**, 4951.
36. W. Erbs, J. Desilvestro, E. Borgarello and M. Graetzel, *The Journal of Physical Chemistry*, 1984, **88**, 4001.
37. J. R. Darwent and A. Mills, *Journal of the Chemical Society, Faraday Transactions 2: Molecular and Chemical Physics*, 1982, **78**, 359.
38. D. J. Ham, A. Phuruangrat, S. Thongtem and J. S. Lee, *Chemical Engineering Journal*, 2010, **165**, 365.
39. T. Jin, P. Diao, D. Xu and Q. Wu, *Electrochimica Acta*, 2013, **114**, 271.
40. J. A. Seabold and K.-S. Choi, *Chemistry of Materials*, 2011, **23**, 1105.
41. J. Augustynski, R. Solarska, H. Hagemann and C. Santato, 2006.
42. J. C. Hill and K.-S. Choi, *The Journal of Physical Chemistry C*, 2012, **116**, 7612.
43. R. Solarska, R. Jurczakowski and J. Augustynski, *Nanoscale*, 2012, **4**, 1553.
44. Q. Mi, A. Zhanaidarova, B. S. Brunshwig, H. B. Gray and N. S. Lewis, *Energy & Environmental Science*, 2012, **5**, 5694.

45. X. Xu, L. Hu, N. Gao, S. Liu, S. Wageh, A. A. Al-Ghamdi, A. Alshahrie and X. Fang, *Advanced Functional Materials*, 2015, **25**, 445.
46. T. Trindade, P. O'Brien and N. L. Pickett, *Chemistry of Materials*, 2001, **13**, 3843.
47. A. Pareek, R. Dom and P. H. Borse, *International Journal of Hydrogen Energy*, 2013, **38**, 36.
48. M. J. Nalbandian, M. Zhang, J. Sanchez, Y.-H. Choa, J. Nam, D. M. Cwiertny and N. V. Myung, *Chemosphere*, 2016, **144**, 975.
49. M.-C. Huang, W.-S. Chang, J.-C. Lin, Y.-H. Chang and C.-C. Wu, *Journal of Alloys and Compounds*, 2015, **636**, 176.
50. J. Kiwi and M. Grätzel, *Journal of the Chemical Society, Faraday Transactions 1: Physical Chemistry in Condensed Phases*, 1987, **83**, 1101.
51. M. A. Gondal, A. Hameed, Z. H. Yamani and A. Suwaiyan, *Applied Catalysis A: General*, 2004, **268**, 159.
52. Y.-S. Hu, A. Kleiman-Shwarsstein, A. J. Forman, D. Hazen, J.-N. Park and E. W. McFarland, *Chemistry of Materials*, 2008, **20**, 3803.
53. E. Thimsen, F. Le Formal, M. Grätzel and S. C. Warren, *Nano Letters*, 2011, **11**, 35.
54. M. Barroso, C. A. Mesa, S. R. Pendlebury, A. J. Cowan, T. Hisatomi, K. Sivula, M. Grätzel, D. R. Klug and J. R. Durrant, *Proceedings of the National Academy of Sciences*, 2012, **109**, 15640.
55. W.-G. Yang, F.-R. Wan, Q.-W. Chen, J.-J. Li and D.-S. Xu, *Journal of Materials Chemistry*, 2010, **20**, 2870.
56. H. Lewerenz, A. Heller and F. DiSalvo, *Journal of the American Chemical Society*, 1980, **102**, 1877.
57. G. Wang, H. Wei, J. Shi, Y. Xu, H. Wu, Y. Luo, D. Li and Q. Meng, *Nano Energy*, 2017, **35**, 17.
58. B. Tang, H. Chen, Y. He, Z. Wang, J. Zhang and J. Wang, *Composites Science and Technology*, 2017, **150**, 54.
59. J. Liu, Q. Jia, J. Long, X. Wang, Z. Gao and Q. Gu, *Applied Catalysis B: Environmental*, 2018, **222**, 35.
60. W. Ouyang, M. J. Muñoz-Batista, A. Kubacka, R. Luque and M. Fernández-García, *Applied Catalysis B: Environmental*, 2018, **238**, 434.
61. S. Chen, B. Pan, L. Zeng, S. Luo, X. Wang and W. Su, *RSC Advances*, 2017, **7**, 14186.
62. M. M. Maitani, T. Yamada, H. Mashiko, K. Yoshimatsu, T. Oshima, A. Ohtomo and Y. Wada, *ACS Applied Materials & Interfaces*, 2017, **9**, 10349.
63. N. Ohshima, *Journal of Applied Physics*, 1996, **79**, 8357.
64. *U.S. Pat.*, 5,385,863, 1995.
65. *U.S. Pat.*, 4,365,107, 1982.
66. S.-W. Song, K. A. Striebel, X. Song and E. J. Cairns, *Journal of Power Sources*, 2003, **119–121**, 110.

67. H. Kim, C.-S. Park, K.-M. Kang, M.-H. Hong, Y.-J. Choi and H.-H. Park, *New Journal of Chemistry*, 2015, **39**, 2256.
68. G. E. Buono-Core, A. H. Klahn, C. Castillo, E. Munoz, C. Manzur, G. Cabello and B. Chornik, *Journal of Non-Crystalline Solids*, 2014, **387**, 21.
69. G. E. Buono-Core, A. H. Klahn, G. Cabello and L. Lillo, *Polyhedron*, 2013, **62**, 1.
70. G. E. Buono-Core, A. H. Klahn, G. Cabello, E. Munoz, M. J. Bustamante, C. Castillo and B. Chornik, *Polyhedron*, 2012, **41**, 134.
71. R. D. Smith, M. S. Prevot, R. D. Fagan, Z. Zhang, P. A. Sedach, M. K. Siu, S. Trudel and C. P. Berlinguette, *Science*, 2013, **340**, 60.
72. R. D. L. Smith, M. S. Prévot, R. D. Fagan, S. Trudel and C. P. Berlinguette, *Journal of the American Chemical Society*, 2013, **135**, 11580.
73. C. Zhang, R. D. Fagan, R. D. L. Smith, S. A. Moore, C. P. Berlinguette and S. Trudel, *Journal of Materials Chemistry A*, 2015, **3**, 756.
74. H. Kisch, L. Zang, C. Lange, W. F. Maier, C. Antonius and D. Meissner, *Angewandte Chemie International Edition*, 1998, **37**, 3034.
75. H. Cao and S. L. Suib, *Journal of the American Chemical Society*, 1994, **116**, 5334.
76. X. Yu, L. Zeng, N. Zhou, P. Guo, F. Shi, D. B. Buchholz, Q. Ma, J. Yu, V. P. Dravid, R. P. H. Chang, M. Bedzyk, T. J. Marks and A. Facchetti, *Advanced Materials*, 2015, **27**, 2390.
77. Y. Li, L. Lan, P. Xiao, Z. Lin, S. Sun, W. Song, E. Song, P. Gao, P. Zhang and J. Peng, *Journal of Materials Chemistry C*, 2016, **4**, 2072.
78. P. R. Pudasaini, J. H. Noh, A. T. Wong, O. S. Ovchinnikova, A. V. Haglund, S. Dai, T. Z. Ward, D. Mandrus and P. D. Rack, *Advanced Functional Materials*, 2016, **26**, 2820.
79. X. Li, Y. Sun, T. Xiong, G. Jiang, Y. Zhang, Z. Wu and F. Dong, *Journal of Catalysis*, 2017, **352**, 102.
80. W. D. Chemelewski, H.-C. Lee, J.-F. Lin, A. J. Bard and C. B. Mullins, *Journal of the American Chemical Society*, 2014, **136**, 2843.
81. K. Nomura, H. Ohta, A. Takagi, T. Kamiya, M. Hirano and H. Hosono, *Nature*, 2004, **432**, 488.
82. R. J. Komp, *Practical Photovoltaics: Electricity from Solar Cells*, Michigan, 1995.
83. C. Wehrli, *Physikalisch-Meteorologisches Observatorium + World Radiation Center (PMO/WRC), Davos Dorf, Switzerland.*, 1985, **615**.
84. R. E. Bird, R. L. Hulstrom and L. J. Lewis, *Solar Energy*, 1983, **30**, 563.
85. W. B. Ingler, J. P. Baltrus and S. U. M. Khan, *Journal of the American Chemical Society*, 2004, **126**, 10238.
86. D. K. Zhong, J. Sun, H. Inumaru and D. R. Gamelin, *Journal of the American Chemical Society*, 2009, **131**, 6086.
87. Z. Li, W. Luo, M. Zhang, J. Feng and Z. Zou, *Energy & Environmental Science*, 2013, **6**, 347.

88. Y. Ling, G. Wang, D. A. Wheeler, J. Z. Zhang and Y. Li, *Nano Letters*, 2011, **11**, 2119.
89. J. S. Jang, J. Lee, H. Ye, F.-R. F. Fan and A. J. Bard, *The Journal of Physical Chemistry C*, 2009, **113**, 6719.
90. N. T. Hahn and C. B. Mullins, *Chemistry of Materials*, 2010, **22**, 6474.
91. M. Li, Y. Yang, Y. Ling, W. Qiu, F. Wang, T. Liu, Y. Song, X. Liu, P. Fang, Y. Tong and Y. Li, *Nano Letters*, 2017, **17**, 2490.
92. J. A. Glasscock, P. R. F. Barnes, I. C. Plumb and N. Savvides, *The Journal of Physical Chemistry C*, 2007, **111**, 16477.
93. C. X. Kronawitter, S. S. Mao and B. R. Antoun, *Applied Physics Letters*, 2011, **98**, 092108.
94. K. D. Malviya, D. Klotz, H. Dotan, D. Shlenkevich, A. Tsyganok, H. Mor and A. Rothschild, *The Journal of Physical Chemistry C*, 2017, **121**, 4206.
95. P. Kumar, P. Sharma, R. Shrivastav, S. Dass and V. R. Satsangi, *International Journal of Hydrogen Energy*, 2011, **36**, 2777.
96. R. Shinar and J. H. Kennedy, *Solar Energy Materials*, 1982, **6**, 323.
97. A. Kay, I. Cesar and M. Grätzel, *Journal of the American Chemical Society*, 2006, **128**, 15714.
98. L. Chen, S. Wu, D. Ma, A. Shang and X. Li, *Nano Energy*, 2018, **43**, 177.
99. V. R. Satsangi, S. Kumari, A. P. Singh, R. Shrivastav and S. Dass, *International Journal of Hydrogen Energy*, 2008, **33**, 312.
100. A. P. Singh, N. Saini, B. R. Mehta, G. Carraro and D. Barreca, *Journal of Nanoscience and Nanotechnology*, 2017, **17**, 8959.
101. L. Parent, J. P. Dodelet and S. Dallaire, *Journal of the Electrochemical Society*, 1987, **134**, 2226.
102. M. Kosa, H. N. Barad, V. Singh, D. A. Keller, K. Shimanovich, S. Rühle, A. Y. Anderson, A. Zaban and D. T. Major, *Physical Chemistry Chemical Physics*, 2016, **18**, 781.
103. E. L. Tsege, T. S. Atabaev, M. A. Hossain, D. Lee, H.-K. Kim and Y.-H. Hwang, *Journal of Physics and Chemistry of Solids*, 2016, **98**, 283.
104. C. Jorand Sartoretti, B. D. Alexander, R. Solarska, I. A. Rutkowska, J. Augustynski and R. Cerny, *The Journal of Physical Chemistry B*, 2005, **109**, 13685.
105. A. Lassoued, M. S. Lassoued, S. García-Granda, B. Dkhil, S. Ammar and A. J. J. o. M. S. M. i. E. Gadri, *Journal of Materials Science: Materials in Electronics*, 2018, **29**, 5726.
106. N. Mirbagheri, D. Wang, C. Peng, J. Wang, Q. Huang, C. Fan and E. E. Ferapontova, *ACS Catalysis*, 2014, **4**, 2006.
107. D. K. Zhong and D. R. Gamelin, *Journal of the American Chemical Society*, 2010, **132**, 4202.
108. A. A. Tahir, K. G. U. Wijayantha, S. Saremi-Yarahmadi, M. Mazhar and V. McKee, *Chemistry of Materials*, 2009, **21**, 3763.

109. W. Yaoming, Y. Tao, C. Xinyi, Z. Haitao, O. Shuxin, L. Zhaosheng, Y. Jinhua and Z. Zhigang, *Journal of Physics D: Applied Physics*, 2007, **40**, 3925.
110. B. Klahr, S. Gimenez, F. Fabregat-Santiago, T. Hamann and J. Bisquert, *Journal of the American Chemical Society*, 2012, **134**, 4294.
111. K. G. Upul Wijayantha, S. Saremi-Yarahmadi and L. M. Peter, *Physical Chemistry Chemical Physics*, 2011, **13**, 5264.
112. W. Luo, Z. Li, T. Yu and Z. Zou, *The Journal of Physical Chemistry C*, 2012, **116**, 5076.
113. N. T. Hahn, H. Ye, D. W. Flaherty, A. J. Bard and C. B. Mullins, *ACS Nano*, 2010, **4**, 1977.
114. E. A. Mayerberger, O. Urbanek, R. M. McDaniel, R. M. Street, M. W. Barsoum and C. L. Schauer, *Journal of Applied Polymer Science*, 2017, **134**, 45295.
115. C. Kim, Y. I. Jeong, B. T. N. Ngoc, K. S. Yang, M. Kojima, Y. A. Kim, M. Endo and J.-W. Lee, *Small*, 2007, **3**, 91.
116. J. J. Santiago-Avilés and Y. Wang, *Carbon*, 2003, **41**, 2665.
117. A. Le Viet, R. Jose, M. V. Reddy, B. V. R. Chowdari and S. Ramakrishna, *The Journal of Physical Chemistry C*, 2010, **114**, 21795.
118. B. H. Lee, M. Y. Song, S.-Y. Jang, S. M. Jo, S.-Y. Kwak and D. Y. Kim, *The Journal of Physical Chemistry C*, 2009, **113**, 21453.
119. P.-P. Wang, Q. Qi, R.-F. Xuan, J. Zhao, L.-J. Zhou and G.-D. Li, *RSC Advances*, 2013, **3**, 19853.
120. Q. Qi, P.-P. Wang, J. Zhao, L.-L. Feng, L.-J. Zhou, R.-F. Xuan, Y.-P. Liu and G.-D. Li, *Sensors and Actuators B: Chemical*, 2014, **194**, 440.
121. G. Larsen, R. Velarde-Ortiz, K. Minchow, A. Barrero and I. G. Loscertales, *Journal of the American Chemical Society*, 2003, **125**, 1154.
122. D. Li, Y. Wang and Y. Xia, *Advanced Materials*, 2004, **16**, 361.
123. E. Shaulsky, S. Nejati, C. Boo, F. Perreault, C. O. Osuji and M. Elimelech, *Journal of Membrane Science*, 2017, **530**, 158.
124. D. Zhang and J. Chang, *Advanced Materials*, 2007, **19**, 3664.
125. Y. Jin, D. Yang, D. Kang and X. Jiang, *Langmuir*, 2009, **26**, 1186.
126. R. A. Caruso, J. H. Schattka and A. Greiner, *Advanced Materials*, 2001, **13**, 1577.
127. Z. Chang, *Chemical Communications*, 2011, **47**, 4427.
128. G. E. Buono-Core, G. Cabello, A. H. Klahn, A. Lucero, M. V. Nunez, B. Torrejon and C. Castillo, *Polyhedron*, 2010, **29**, 1551.
129. J. Y. Wang, U. Starke and E. J. Mittemeijer, *Thin Solid Films*, 2009, **517**, 3402.
130. L. Wang, X. Nie, M. J. Lukitsch, J. C. Jiang and Y. T. Cheng, *Surface and Coatings Technology*, 2006, **201**, 4341.
131. Z. Fu, T. Jiang, L. Zhang, B. Liu, D. Wang, L. Wang and T. Xie, *Journal of Materials Chemistry A*, 2014, **2**, 13705.
132. M. Barroso, A. J. Cowan, S. R. Pendlebury, M. Grätzel, D. R. Klug and J. R. Durrant, *Journal of the American Chemical Society*, 2011, **133**, 14868.

133. D. K. Zhong, M. Cornuz, K. Sivula, M. Gratzel and D. R. Gamelin, *Energy & Environmental Science*, 2011, **4**, 1759.
134. M. Alexander, K. Ilina, F. Alena, F.-R. Dina, B. Thomas and S. Christina, *Materials Research Express*, 2017, **4**, 016409.
135. M. Pyeon, T.-P. Ruoko, J. Leduc, Y. Gönüllü, M. Deo, N. V. Tkachenko and S. Mathur, *Journal of Materials Research*, 2018, **33**, 455.
136. N. Yatom, O. Neufeld and M. Caspary Toroker, *The Journal of Physical Chemistry C*, 2015, **119**, 24789.
137. M. Antuch, P. Millet, A. Iwase and A. Kudo, *Applied Catalysis B: Environmental*, 2018, **237**, 401.
138. Q. Liu, C. Chen, G. Yuan, X. Huang, X. Lü, Y. Cao, Y. Li, A. Hu, X. Lu and P. Zhu, *Journal of Alloys and Compounds*, 2017, **715**, 230.
139. F. Giordano, A. Abate, J. P. Correa Baena, M. Saliba, T. Matsui, S. H. Im, S. M. Zakeeruddin, M. K. Nazeeruddin, A. Hagfeldt and M. Graetzel, *Nature Communications*, 2016, **7**, 10379.
140. P. Tan, *Journal of Catalysis*, 2016, **338**, 21.
141. C. D. Wagner, L. E. Davis, M. V. Zeller, J. A. Taylor, R. H. Raymond and L. H. Gale, *Surface and Interface Analysis*, 1981, **3**, 211.
142. C. D. Wagner, *Journal of Electron Spectroscopy and Related Phenomena*, 1983, **32**, 99.
143. A. Kay, D. A. Grave, D. S. Ellis, H. Dotan and A. Rothschild, *ACS Energy Letters*, 2016, **1**, 827.
144. A. Tsyganok, D. Klotz, K. D. Malviya, A. Rothschild and D. A. Grave, *ACS Catalysis*, 2018, **8**, 2754.
145. T. Hisatomi, F. Le Formal, M. Cornuz, J. Brillet, N. Tétreault, K. Sivula and M. Grätzel, *Energy & Environmental Science*, 2011, **4**, 2512.
146. D. K. Zhong, M. Cornuz, K. Sivula, M. Grätzel, D. R. J. E. Gamelin and E. Science, *Energy & Environmental Science*, 2011, **4**, 1759.
147. X. Liu, J. I. Yang, L. y. Tong, Q. Zhang, X. w. Li and J. d. J. C. R. i. C. U. Chen, *Chemical Research in Chinese Universities*, 2015, **31**, 1062.
148. S. Saallah, M. N. Naim, I. W. Lenggoro, M. N. Mokhtar, N. F. Abu Bakar and M. Gen, *Biotechnology Reports*, 2016, **10**, 44.
149. A. M. M. Sousa, H. K. S. Souza, J. Uknalis, S.-C. Liu, M. P. Gonçalves and L. Liu, *Carbohydrate Polymers*, 2015, **115**, 348.
150. W. Samprasit, P. Akkaramongkolporn, T. Ngawhirunpat, T. Rojanarata, R. Kaomongkolgit and P. Opanasopit, *International Journal of Pharmaceutics*, 2015, **487**, 213.
151. T. L. Yang, C. T. Pan, Y. C. Chen, L. W. Lin, I. C. Wu, K. H. Hung, Y. R. Lin, H. L. Huang, C. F. Liu, S. W. Mao and S. W. Kuo, *Optical Materials*, 2015, **39**, 118.
152. S. Shih, C. Chen and C. Chung, 2018.
153. A. Khalf and S. V. Madihally, *European Journal of Pharmaceutics and Biopharmaceutics*, 2017, **112**, 1.

154. Y. Lu, J. Huang, G. Yu, R. Cardenas, S. Wei, E. K. Wujcik and Z. Guo, *Wiley Interdiscip Rev Nanomed Nanobiotechnol*, 2016, **8**, 654.
155. D.-G. Yu, X.-Y. Li, X. Wang, J.-H. Yang, S. W. A. Bligh and G. R. Williams, *ACS Applied Materials & Interfaces*, 2015, **7**, 18891.
156. S. Khorshidi, A. Solouk, H. Mirzadeh, S. Mazinani, J. M. Lagaron, S. Sharifi and S. Ramakrishna, *Journal of Tissue Engineering and Regenerative Medicine*, 2016, **10**, 715.
157. J. Hu, D. Kai, H. Ye, L. Tian, X. Ding, S. Ramakrishna and X. J. Loh, *Materials Science and Engineering: C*, 2017, **70**, 1089.
158. L. C. Lins, F. Wianny, S. Livi, I. A. Hidalgo, C. Dehay, J. Duchet-Rumeau and J.-F. Gérard, *Biomacromolecules*, 2016, **17**, 3172.
159. H. Han, S. Kment, A. Goswami, O. Haderka and R. Zboril, *MRS Advances*, 2016, **1**, 3145.
160. M. G. Mali, S. An, M. Liou, S. S. Al-Deyab and S. S. Yoon, *Applied Surface Science*, 2015, **328**, 109.
161. A. Lepcha, C. Maccato, A. Mettenböcker, T. Andreu, L. Mayrhofer, M. Walter, S. Olthof, T. P. Ruoko, A. Klein, M. Moseler, K. Meerholz, J. R. Morante, D. Barreca and S. Mathur, *The Journal of Physical Chemistry C*, 2015, **119**, 18835.
162. S. S. Mali, C. Su Shim and C. Kook Hong, *Scientific Reports*, 2015, **5**, 11424.
163. F. Pierini, M. Lanzi, P. Nakielski, S. Pawłowska, O. Urbanek, K. Zembrzycki and T. A. Kowalewski, *Macromolecules*, 2017, **50**, 4972.
164. N. Singh, Z. Salam, A. Subasri, N. Sivasankar and A. Subramania, *Solar Energy Materials and Solar Cells*, 2018, **179**, 417.
165. C. Drew, X. Liu, D. Ziegler, X. Wang, F. F. Bruno, J. Whitten, L. A. Samuelson and J. Kumar, *Nano Letters*, 2003, **3**, 143.
166. D. Regonini, A. C. Teloecken, A. K. Alves, F. A. Berutti, K. Gajda-Schrantz, C. P. Bergmann, T. Graule and F. Clemens, *ACS Applied Materials & Interfaces*, 2013, **5**, 11747.
167. L. Zhang, L. Wang, Y. Wei, M. Zhang, H. Jiang, J. Li, S. Li and J. Li, *European Journal of Inorganic Chemistry*, 2015, **2015**, 5039.
168. D. Jing and L. Guo, *The Journal of Physical Chemistry B*, 2006, **110**, 11139.
169. D. J. Fermín, E. A. Ponomarev and L. M. Peter, *Journal of Electroanalytical Chemistry*, 1999, **473**, 192.
170. D. R. Baker and P. V. Kamat, *Advanced Functional Materials*, 2009, **19**, 805.
171. J. S. Jang, S. H. Choi, H. G. Kim and J. S. Lee, *The Journal of Physical Chemistry C*, 2008, **112**, 17200.
172. R. Raja, P. Sudhagar, A. Devadoss, C. Terashima, L. K. Shrestha, K. Nakata, R. Jayavel, K. Ariga and A. Fujishima, *Chemical Communications*, 2015, **51**, 522.
173. X. Wang, L. Yin and G. Liu, *Chemical Communications*, 2014, **50**, 3460.
174. H. Zhao, Y. Dong, P. Jiang, G. Wang, H. Miao, R. Wu, L. Kong, J. Zhang and C. Zhang, *ACS Sustainable Chemistry & Engineering*, 2015, **3**, 969.

175. Y. P. Xie, Y. Yang, G. Wang and G. Liu, *Journal of Colloid and Interface Science*, 2017, **503**, 198.
176. D. Ma, J.-W. Shi, Y. Zou, Z. Fan, X. Ji, C. Niu and L. Wang, *Nano Energy*, 2017, **39**, 183.
177. C. Han, Z. Chen, N. Zhang, J. C. Colmenares and Y.-J. Xu, *Advanced Functional Materials*, 2015, **25**, 221.
178. X. Zong, H. Yan, G. Wu, G. Ma, F. Wen, L. Wang and C. Li, *Journal of the American Chemical Society*, 2008, **130**, 7176.
179. X. Zong, G. Wu, H. Yan, G. Ma, J. Shi, F. Wen, L. Wang and C. Li, *The Journal of Physical Chemistry C*, 2010, **114**, 1963.
180. L. Shen, M. Luo, Y. Liu, R. Liang, F. Jing and L. Wu, *Applied Catalysis B: Environmental*, 2015, **166-167**, 445.
181. W. Zhong, W. Tu, S. Feng and A. Xu, *Journal of Alloys and Compounds*, 2019, **772**, 669.
182. Q. Xiang, F. Cheng and D. Lang, *ChemSusChem*, 2016, **9**, 996.
183. K. Kalyanasundaram, E. Borgarello and M. Grätzel, *Helvetica Chimica Acta*, 1981, **64**, 362.
184. V. M. Daskalaki, M. Antoniadou, G. Li Puma, D. I. Kondarides and P. Lianos, *Environmental Science & Technology*, 2010, **44**, 7200.
185. J. Fang, W. Wang, C. Zhu, L. Fang, J. Jin, Y. Ni, C. Lu and Z. Xu, *Applied Catalysis B: Environmental*, 2017, **217**, 100.
186. M. Luo, W. Yao, C. Huang, Q. Wu and Q. Xu, *Journal of Materials Chemistry A*, 2015, **3**, 13884.
187. T. Simon, M. T. Carlson, J. K. Stolarczyk and J. Feldmann, *ACS Energy Letters*, 2016, **1**, 1137.
188. N. Li, X. Zhang, S. Chen, X. Hou, Y. Liu and X. Zhai, *Materials Science and Engineering: B*, 2011, **176**, 688.
189. L. Zhang, X. Fu, S. Meng, X. Jiang, J. Wang and S. Chen, *Journal of Materials Chemistry A*, 2015, **3**, 23732.
190. J. Chen, X.-J. Wu, L. Yin, B. Li, X. Hong, Z. Fan, B. Chen, C. Xue and H. Zhang, *Angewandte Chemie, International Edition in English*, 2015, **127**, 1226.
191. S. Zhang, H. Yang, H. Gao, R. Cao, J. Huang and X. Xu, *ACS Applied Materials & Interfaces*, 2017, **9**, 23635.
192. J. Zhu, O. Palchik, S. Chen and A. Gedanken, *The Journal of Physical Chemistry B*, 2000, **104**, 7344.
193. L. Jiang, L. Wang, G. Xu, L. Gu and Y. Yuan, *Sustainable Energy & Fuels*, 2018, **2**, 430.
194. F. Kishimoto, T. Imai, S. Fujii, D. Mochizuki, M. M. Maitani, E. Suzuki and Y. Wada, *Scientific Reports*, 2015, **5**, 11308.
195. L. Manna, E. C. Scher and A. P. Alivisatos, *Journal of the American Chemical Society*, 2000, **122**, 12700.

196. P. Rukenstein, A. Teitelboim, M. Volokh, M. Diab, D. Oron and T. Mokari, *The Journal of Physical Chemistry C*, 2016, **120**, 15453.
197. H. Yan, J. Yang, G. Ma, G. Wu, X. Zong, Z. Lei, J. Shi and C. Li, *Journal of Catalysis*, 2009, **266**, 165.
198. J. S. Jang, S. M. Ji, S. W. Bae, H. C. Son and J. S. Lee, *Journal of Photochemistry and Photobiology A: Chemistry*, 2007, **188**, 112.
199. C. Cheng, S. K. Karuturi, L. Liu, J. Liu, H. Li, L. T. Su, A. I. Y. Tok and H. J. Fan, *Small*, 2012, **8**, 37.
200. M. Radecka, A. Trenczek-Zajac, K. Zakrzewska and M. Rekas, *Journal of Power Sources*, 2007, **173**, 816.
201. D. K. Zhong, M. Cornuz, K. Sivula, M. Grätzel and D. R. Gamelin, *Energy & Environmental Science*, 2011, **4**, 1759.